Evaporation of moderately volatile elements from silicate melts: experiments and theory

Paolo Sossi, Stephan Klemme, Hugh St.C. O'Neill, Jasper Berndt, Frédéric Moynier

Evaporation of moderately volatile elements from silicate melts: experiments and theory

Paolo A. Sossi[1*], Stephan Klemme[2], Hugh St.C. O'Neill[3], Jasper Berndt[2], Frédéric Moynier[1, 4]

[1]Institut de Physique du Globe de Paris, 1 rue Jussieu, F-75005, Paris, France

[2]Institut für Mineralogie, Westfälische Wilhelms-Universität Münster, Correnst. 24, D48149 Münster, Germany

[3]Research School of Earth Sciences, Australian National University, 2601 Canberra, Australia

[4]Institut Universitaire de France, 75005, Paris, France

* Corresponding author. Present address: Institute of Geochemistry and Petrology, ETH Zürich, Sonneggstrasse 5, CH-8092, Zürich, Switzerland. E-mail: paolo.sossi@erdw.ethz.ch

Abstract

Moderately volatile elements (MVEs) are sensitive tracers of vaporisation in geological and cosmochemical processes owing to their balanced partitioning between vapour and condensed phases. Differences in their volatilities allows the thermodynamic conditions, particularly temperature and oxygen fugacity (fO_2), at which vaporisation occurred to be quantified. However, this exercise is hindered by a lack of experimental data relevant to the evaporation of MVEs from silicate melts. We report a series of experiments in which silicate liquids are evaporated in one-atmosphere (1-atm) gas-mixing furnaces under controlled fO_2s, from the Fe-"FeO" buffer (iron-wüstite, IW) to air ($10^{-0.68}$ bars), bracketing the range of most magmatic rocks. Time- (t) and temperature (T) series were conducted from 15 to 930 minutes and 1300-1550°C, at or above the liquidus for a synthetic ferrobasalt, to which 20 elements, each at 1000 ppm, were added. Refractory elements (*e.g.*, Ca, Sc, V, Zr, REE) are quantitatively retained in the melt under all conditions. The MVEs show highly redox-dependent volatilities, where the extent of element loss as a function of fO_2 depends on the stoichiometry of the evaporation reaction(s), each of which has the general form $M^{x+n}O_{(x+n)/2} = M^{x}O_{x/2} + n/4O_2$. Where n is positive (as in most cases), the oxidation state of the element in the gas is more reduced than in the liquid, meaning lower oxygen fugacity promotes evaporation. We develop a general framework, by integrating element vaporisation stoichiometries with Hertz-Knudsen-Langmuir (HKL) theory, to quantify evaporative loss as a function of t, T and fO_2. Element volatilities from silicate melts differ from those during solar nebular condensation, and can thus constrain the conditions of volatile loss in post-nebular processes. Evaporation in a single event strongly discriminates between MVEs, producing a step-like abundance pattern in the residuum, similar to that observed in the Moon or Vesta. Contrastingly, the gradual depletion of MVEs according to their volatility in the Earth is inconsistent with their loss in a single evaporation event, and instead likely reflects accretion from many smaller bodies that had each experienced different degrees of volatilisation.

Keywords: Moderately Volatile Element, Evaporation, Volatile Depletion, Experiment, Silicate Melts

1.0. Introduction

Phase transformation from condensed (liquid, l, or solid, s) to gaseous (g) form, termed evaporation, is a ubiquitous geological process occurring during outgassing of ascending magmas (Symonds and Reed, 1993; Mather et al., 2012), upon heating attending meteorite impacts in the crust (Humayun and Koeberl, 2004; Moynier et al., 2009) and, on a larger scale, in planetary accretion processes (O'Neill, 1991; Alexander, 2001; Visscher and Fegley, 2013). The *volatility* of an element refers to its tendency to partition into the gas phase relative to condensed phases, and at equilibrium, depends on the thermodynamic conditions, especially the temperature and fO_2 at which these processes occur.

Under solar nebula conditions, the volatility of an element is quantified by its '50% condensation temperature', T_c^{50}, the temperature at which half its mass is calculated to condense from a gas of solar composition at equilibrium (Larimer, 1967). As T_c^{50} of the elements vary among one another, their abundances in chondrites may be used to constrain temperatures at which they accreted (*e.g.,* Keays et al. 1971; Laul et al. 1973), a concept known as 'cosmothermometry' (Urey, 1954). Although elemental abundances in chondrites correlate positively with T_c^{50}, these temperatures refer to specific conditions; that of a rarified (tenuous) nebular gas, with assumed pressures, P_{total} of 10^{-3}-10^{-5} bar (Larimer, 1967; Grossman, 1972; Grossman and Larimer, 1974; Lodders, 2003), in which H_2 is the most abundant species, such that $pH_2 \sim P_{total}$. The correspondingly low H_2O/H_2 (5×10^{-4}; Rubin et al. 1988) of the solar nebula promotes very reducing conditions, ~7 log units below the iron-wüstite (IW) oxygen buffer at 1400 K. Low total pressures result in condensation temperatures that are below the silicate, metal and sulfide solidi, such that condensation occurs into solid phases (Ebel, 2004).

In the absence of any other scale, T_c^{50} has been widely used to quantify element volatility in various other contexts, such as degassing from planetary bodies. Although refractory elements and the main components (Fe, Mg, Si) in the Earth and other planetary bodies (the Moon, Mars, Vesta) have abundances similar to those in chondritic meteorites, the moderately volatile elements (MVEs), with $650 < T_c^{50}$ (K) < 1300 at 10^{-4} bar (Palme et al., 1988), are variably depleted (Urey, 1954; Ringwood, 1966; Wanke and Dreibus, 1988; O'Neill and Palme, 1998; Albarède et al., 2015). The sub-equal distribution of MVEs between the gas and condensed phases holds promise for quantifying the conditions of volatile loss processes, which neither refractory elements (hardly lost) nor highly volatile elements (almost entirely lost) address.

Chondrite-normalised abundances of lithophile MVEs in the mantles of differentiated rocky bodies plotted against T_c^{50} define 'volatility trends'. Depletions of siderophile MVEs relative to these trends point to their additional loss to planetary cores (*e.g.,* Wood et al. 2006; Siebert and Shahar 2015). However, the proportions of siderophile MVEs (*e.g.,* Ga, Pb, In) inferred to reside in Earth's core using this approach are irreconcilable with their experimentally-determined metal-silicate partition coefficients

(Wang et al. 2016; Blanchard et al. 2017; Ballhaus et al. 2017; Norris and Wood, 2017), suggesting T_c^{50} may not be an apt descriptor of volatility at the conditions relevant to the formation of Earth.

The assumption implicit in the use of T_c^{50} states that volatile loss occurred under the same solar nebular conditions experienced by chondritic meteorites, and therefore neglects variations in nebular chemistry (*cf.* Ebel and Grossman 2000; Schaefer and Fegley 2010), in addition to the likelihood that planetary bodies continued to accrete following dissipation of the nebular gas. Indeed, numerical simulations of planetary formation highlight the potential for chemical fractionation to occur throughout their growth (*e.g.,* Morbidelli et al. 2012; Carter et al. 2015). These *post-nebular* processes include collisional erosion of differentiated material (O'Neill and Palme, 2008; Bonsor et al., 2015) and melting and evaporation of planetesimals or planets *via* ^{26}Al and ^{60}Fe decay (Sahijpal et al., 2007) or impact heating (Pahlevan et al., 2011). Models for the Moon-forming impact invoke temperatures ≥4000 K (*e.g.,* Melosh 1990; Nakajima and Stevenson 2014) and pressures between 10^{-3} and 100 bar (Canup et al., 2015). The fO_2 of the gas evolved by evaporation of silicates is close to the Fayalite-Magnetite-Quartz (FMQ) buffer (De Maria et al., 1971; Visscher and Fegley, 2013; Costa et al., 2017), orders of magnitude higher than in the solar nebula. Moreover, elemental depletions in planetary environments reflect not only volatility, but also the ability for the gas species to be carried away from the locus of vaporisation, which varies with physical factors such as planetary size, molar mass and atmospheric structure (Chamberlain and Hunten, 1989). As such, equilibrium is not mandated during evaporation (Young et al. 2019) and the physical mechanism cannot, *a priori*, be treated as the inverse of equilibrium condensation. Indeed, MVE depletion patterns in many planetary bodies are quite unlike those in chondritic meteorites (*e.g.,* O'Neill and Palme, 2008), attesting to their accretion under conditions and/or *via* mechanisms distinct from those of the solar nebula. Volatility trends established under these post-nebular conditions should thus diverge from expectations based on T_c^{50}. Together, these considerations call for more quantitative descriptions of element volatility relevant to the evaporation of silicate melts.

Existing experimental constraints (Chapman and Scheiber, 1969; Notsu et al., 1978; Bart et al., 1980; Tsuchiyama et al., 1981; Kreutzberger et al., 1986; Shimaoka et al., 1994; Wulf et al., 1995; Norris and Wood, 2017; Braukmüller et al., 2018) highlight a dependence of element volatility on fO_2; some elements (*e.g.,* Zn, Cd, Na) become more volatile at low fO_2, whereas others (*e.g.,* Ir, Au, As) become less so. Differences were found between volatilities inferred from evaporation of silicate melts and those calculated for solar nebula condensation. While abundances of elements that are refractory in the solar nebula (*e.g.,* Al, Ti, Sc, REEs) increased in evaporation residues (Chapman and Scheiber, 1969; Notsu et al., 1978), K (T_c^{50} = 1006 K) was observed to vaporise more readily than Na (T_c^{50} = 958 K) (Kreutzberger et al., 1986) while In (T_c^{50} = 536 K) was found to be less volatile than Zn (T_c^{50} = 726 K) (Norris and Wood, 2017). Norris and Wood (2017) argued that, because this order of volatility better matched the MVE depletions observed in Earth's mantle, they were lost *via* evaporation from silicate

melts rather than during nebular condensation. Nevertheless, a theoretical understanding of the process studied in these experiments has hitherto not been addressed.

Here, we present experimental results of trace element loss during Langmuir (free) evaporation of a ferrobasaltic melt composition as a function of run time, temperature and fO_2. We develop a theoretical approach based on Hertz-Knudsen-Langmuir (HKL) theory (*e.g*, Knudsen 1909) that quantifies the effect of *t*, *T* and fO_2 on element loss and determines stoichiometries of element vaporisation reactions. This model enables extrapolation and prediction of evaporative element loss from silicate melts and is used to better understand the conditions and mechanisms that lead to volatile depletion among rocky planetary bodies.

2.0. Methods

2.1. Experimental Methods

Reagent-grade, major-element oxide powders (Fe_2O_3-MgO-Al_2O_3-SiO_2) were weighed out and ground in an agate mortar. Calcium was added as carbonate ($CaCO_3$). The major element composition (Table 1) represents a compromise between achieving a low liquidus temperature whilst still resembling a realistic planetary mantle composition. To this end, an Anorthite-Diopside eutectic composition was used, to which roughly 15 *wt.* % each of forsterite and Fe_2O_3 were added. Trace elements were added to a separate mixture; the alkalis (Li, Na, K, Rb) were added as carbonates. The remaining elements were added as oxides, so as to mimic their speciation in silicate melts (addition of elements as solutions, *e.g.*, nitrates was avoided as this may cause elements to behave abnormally during heating). Oxides added were: Cu_2O, Ga_2O_3, GeO_2, PbO, MnO, MoO_2, V_2O_5, ZrO_2, Sc_2O_3, ZnO, TiO_2, La_2O_3, Gd_2O_3, Yb_2O_3, Ag_2O and CdO, totalling 20 elements, six of which (Zr, Sc, Ti, and the REEs) are nominally refractory. All oxides were added in proportions equivalent to one-another, to give ≈ 28,000 ppm of the element in the final trace element mix, of which 3.6 wt. % was added to the FCMAS composition to give ≈ 1000 ppm of each element in the final mixture (Table 1). The ensemble was then decarbonated at 1000 °C for 24 h in air and re-ground. Experiments were also performed with the FCMAS mix prior to the addition of the trace element mixture to assess the degree of contamination during the experiments.

For each experiment, around 25 mg of powder was mixed into a viscous slurry with 100,000 molecular weight polyethylene oxide and loaded onto a metal wire loop. In order to minimise Fe, and other metal loss to the loop, Re was used where possible at reducing conditions (below FMQ), whereas Pt loops (and one Ir loop) were used above FMQ. Oxygen fugacity was externally buffered by CO–CO_2 gas mixtures metered from Tylan mass flow controllers (range 0–200 and 0–20 standard cubic centimetres per minute, sccm), whose performance was checked *in-situ* using a yttria-stabilised zirconia $SIRO_2$ oxygen sensor at 1000 °C (see O'Neill and Eggins, 2002). The sensor was not used in

the actual experiments because of the high temperatures. Oxygen fugacities varied between 10^{-10} bar (≈IW) to $10^{-0.68}$ bar (air) at a given temperature, at an estimated accuracy of ±0.05 log units. Excepting experiments in air and at ANU, the total gas flow rate was kept constant at each oxygen fugacity, ≈ 200 sccm. Gas flow rates are listed in Table 2, along with run duration and temperature. Experiments performed at Westfälische Wilhelms-Universität, Münster, are denoted by the code 'M', those at the Research School of Earth Sciences, ANU, by 'C' and at the Institut de Physique du Globe de Paris, by 'P'.

Samples were introduced into the 3-cm-long hotspot of a 42-mm internal-diameter, 70-cm-long GERO vertical alumina tube furnace directly at the set-temperature, between 1300 < T (°C) < 1550, with run times between 15 min and 930 min. Gases were allowed to run and equilibrate in the sealed furnace tube for ≈ 10 min prior to sample introduction. The gas continually flowed through the tube, and was evacuated by a line at the top of the furnace. The volume of the furnace tube relative to that of the sample is sufficiently large that vapour produced upon sample evaporation was efficiently removed from the hotspot and condensed in the cold zones of the tube, thereby approximating an open system. Temperature was controlled with a thermocouple external to the alumina muffle tube by a Eurotherm® controller, limiting fluctuations to within ±1 °C. Temperatures were independently measured, and adjusted as necessary, with a Type B thermocouple bead (Klemme and O'Neill, 2000) located <5 mm above the sample. Run duration is reported from the time of sample insertion and therefore includes a thermal equilibration time. This time (defined as the time needed to reach 99% of the set temperature) was determined to be between 4 – 7 minutes, conforming to the relationship $dT/dt = k(T_{final}-T)$, where k is the response time constant. When integrated with respect to time and temperature, this gives $t = (-\ln(T_{final}-T)+\ln(T_{final}))/k$. The value of k was experimentally determined to be 0.018 at 1350°C from the observed increase in temperature for a Type B thermocouple bead of 10^{-4} m radius. The response time constant is related to specific heat capacity (C_p), mass (m) and area (A) of the material by the expression $k = hA/mC_p$, where h is the external heat transfer coefficient and depends on the properties of the gas phase. Since silicate melt spheres in our experiments have higher heat capacities (≈ 1500 J/kgK) and surface areas (≈ 2×10^{-5} m) than the thermocouple bead, equilibration times are expected to be similar. Charges were quenched by dropping them into a beaker of distilled water.

2.2. Analytical Methods

Trace element abundances in the quenched glasses were measured by Laser-Ablation Inductively-Coupled Plasma Mass Spectrometry (LA-ICP-MS) at the Institut für Mineralogie, Westfälische Wilhelms-Universität Münster. Glasses were mounted in epoxy and polished before being placed in a dual-volume Helex cell filled with He gas (≈ 1 L/min; large cell and 0.33 L/min, small cell). Ablation was performed by a Photon Machines Analyte G2 193 nm ArF excimer laser with a repetition rate of

10 Hz, a total fluence of 4 J/cm^2 and a spot size of 130 µm (25 µm for zoning profiles). The ablation sequence consisted of 20 s background and 40 s of counting time, in which the ablated material was carried to the *ThermoFisher* Element II running in low resolution mode. Each mass peak is measured four times (100 samples per peak with a mass window of 4%) for a total of 0.02 s each. The isotopes measured for this purpose were: ^{7}Li, ^{23}Na, ^{29}Si, ^{39}K, ^{43}Ca, ^{45}Sc, ^{47}Ti, ^{49}Ti, ^{51}V, ^{53}Cr, ^{55}Mn, ^{60}Ni, ^{63}Cu, ^{66}Zn, ^{69}Ga, ^{72}Ge, ^{73}Ge, ^{85}Rb, ^{90}Zr, ^{93}Nb, ^{95}Mo, ^{107}Ag, ^{111}Cd, ^{115}In, ^{133}Cs, ^{139}La, ^{157}Gd, ^{172}Yb, ^{182}W, ^{185}Re, ^{193}Ir, ^{195}Pt, ^{208}Pb, totalling an analytical pass time of roughly 0.6 s. Oxide production rates, as monitored by the ^{232}Th^{16}O/^{232}Th ratio, were < 0.1 %.

Samples were ablated between 6 – 12 times, with care taken to analyse both the core and rim of the glass bead, permitting detection of any zoning. Standards bracketed sample ablation every 12 – 24 points (*i.e.*, every two samples), and consisted of a set of three NIST-612 and two basaltic standards (either BCR-2G, GSD-1G, GSE-1G or BIR-1G, depending on the session). Standardisation was performed in two stages. Firstly, the NIST-612 standard glass, in which trace elements are present at ≈ 40 ppm levels, was used to produce calibration curves relating counts per second to concentration for a given isotope. Following this initial normalisation, ^{29}Si was used as an internal standard (41 wt. % SiO_2 in samples) to correct for matrix effects between the samples and NIST-612 by comparison with BCR-2G, GSD-1G, GSE-1G or BIR-1G, whose matrix is a good analogue for the experimental glasses.

Relative standard deviation (RSD) across all elements in a given sample was 5.1±0.4% (SD), excluding cases where the element concentration was near the detection limit (frequently Cd and Ag, but also in some experiments where elements have been quantitatively lost). In these instances, the RSD increases to 15 – 20%, while Li also has a high RSD (≈10%), presumably owing to the analyses of Li tetra- and metaborate-fluxed fused discs on the LA-ICP-MS system. For major elements and those with interference-free masses (*e.g.*, Na, Sc, V, Cr, Mn, Rb and the REE), RSD is typically 2-3 %. Analytical accuracy was assessed by analyses of basaltic reference materials; concentrations of all elements were found to be within 10% (and often 5%) of the most recent published analyses using femtosecond LA-ICP-MS (Jochum et al. 2014; Li et al. 2015; Electronic Annex A). The sole exception is Ge; its measured abundance is systematically higher in BCR-2G (^{72}Ge, 2.16±0.10 and ^{73}Ge, 2.23±0.16 ppm) and BIR-1G (^{72}Ge, 4.25±0.60 and ^{73}Ge, 2.18±0.44 ppm) compared to published values (1.51±0.10 and 1.2±0.1 ppm, respectively). This discrepancy disappears for synthetic basaltic glasses with higher Ge contents; GSD-1G (39.07±0.99 *vs.* 40±1 ppm) and GSE-1G (391.6±13.6 *vs.* 402±16 ppm), pointing to the production of ^{56}Fe^{16}O^{+} and lesser amounts of ^{57}Fe^{16}O^{+} and ^{56}Fe^{16}O^{1}H^{+} on ^{72}Ge and ^{73}Ge, respectively. While these interferences degrade the accuracy of Ge measurements at low abundances (≈ 1 ppm), they are negligible at the concentrations relevant to the experiments (10 – 1000 ppm).

3.0. Theoretical Framework

The kinetic theory of gases states that particles in an isothermal ideal gas have a Maxwell-Boltzmann distribution of kinetic energies (Maxwell, 1860; Boltzmann, 1872). Such molecular chaos (*stosszahlansatz*) occurs when the mean free path, the average distance travelled by a gaseous molecule prior to collision, is greater than the diameter of the particles. At 1673 K and 1 bar, the mean free path is ≈5×10^{-6} metres, 10^4 times larger than typical molecular diameters (Chapman and Cowling, 1970). In this framework, the number of particles striking a surface over a given time interval is given by the Hertz-Knudsen-Langmuir (HKL) equation (Hertz, 1882; Knudsen, 1909; Langmuir, 1916; Hirth and Pound, 1963; Richter et al., 2002):

$$\frac{dn_i}{dt} = -A\frac{\alpha_e p_{i,sat} - \alpha_c p_i}{\sqrt{2\pi RMT}}, \quad (1)$$

Here, $\frac{dn_i}{dt}$ is the flux (mol/s), A the surface area (m^2), $p_{i,sat}$ is the equilibrium partial pressure of the gas species of element i (Pa) and M its molar mass (kg/mol), p_i its partial pressure at the surface, α_e and α_c the dimensionless Langmuir coefficients for evaporation and condensation respectively, R the gas constant (J/mol.K) and T absolute temperature.

Langmuir evaporation ($p_{i,sat} \gg p_i$) involves liquid-gas equilibrium only at infinitesimally small intervals, after which each parcel of gas is removed from the system, rendering it thermodynamically irreversible. Theoretically, the HKL equation implicitly assumes thermal equilibrium between liquid and gas. The high thermal mass of the surrounding gas with respect to sample in the furnace hotspot satisfies this condition, under which the HKL equation accurately describes the Langmuir evaporation flux (Littlewood and Rideal, 1956; Persad and Ward, 2016).

The evaporation rate is maximal when p_i = 0 (eq. 1). Though not measurable in these experiments, p_i relates to the accumulation of molecules of i at the evaporating surface and hence depends on the evaporation rate relative to the transport rate of i away from the surface. At our experimental conditions, element evaporation rates are relatively slow (≈ 10^{-4} cm^2/s) relative to transport rates, which are due to both diffusion and advection, and are of the order of several cm^2/s (Electronic Annex B). In this limit the gas is instantaneously removed from the locus of evaporation, maintaining $p_i \approx 0$ and, for a sphere, eq. 1 reduces to:

$$dn_i = -4\pi r^2 \frac{\alpha_e p_{i,sat}}{\sqrt{2\pi RMT}} dt. \quad (2)$$

Dividing eq. 2 by the total number of moles n_T^0, since $\left(\frac{n_i}{n_T^0}\right) = X_i$ and $n_T^0 = \frac{4\pi r^3 \rho}{3M}$, gives:

$$dX_i = -\alpha_e p_{i,sat} \frac{3}{r\rho} \sqrt{\frac{M}{2\pi RT}}\, dt. \quad (3)$$

Element loss rate is also affected by the radius (r) and density (ρ) of the sample (eq. 3). A factor of 2 variation in r results in differences in concentration of ≤ 7%, and, because the major elements (Si, Mg, Fe, Al and Ca) are non-volatile in the experiments, ρ is near-constant (Electronic Annex B). Thus, r = 0.001 m was used for all experiments and ρ was calculated for each run using the model of Bottinga and Weill (1970) and varied between 2761 and 2905 kg/m^3.

Though the equilibrium partial vapour pressure, $p_{i,sat}$, is not directly measurable in these kinetic experiments, it may be calculated from equilibrium thermodynamics if the chemical reaction(s) describing the vaporisation are known. In the general case of the evaporation of a metal oxide species dissolved in the melt, $\left(M^{x+n}\frac{x+n}{2}O\right)(l)$, to a gaseous species that may have a different valence state, $\left(M^xO_{\frac{x}{2}}\right)(g)$, the reaction is:

$$\left(M^{x+n}\frac{x+n}{2}O\right)(l) = \left(M^xO_{\frac{x}{2}}\right)(g) + \frac{n}{4}O_2 \quad (4)$$

Here, M is the metal, x its formal charge (an integer value) and n the number of electrons in the reaction. Because the evaporating gas is tenuous, we assume ideal gas behaviour, such that $f = p$. The equilibrium constant of eq. 4, $K_{(4)}$, re-arranged to solve for p, the partial pressure of $M^xO_{\frac{x}{2}}$ in the gas, is:

$$p\left(M^xO_{\frac{x}{2}}\right) = \frac{K_{(4)}X\left(M^{x+n}O_{\frac{x+n}{2}}\right)\gamma\left(M^{x+n}O_{\frac{x+n}{2}}\right)}{f(O_2)^{n/4}}. \quad (5)$$

In eq. 5, X and γ refer to the mole fraction and activity coefficient, respectively, of $M^{x+n}O_{\frac{x+n}{2}}$ in the liquid. For clarity, we make the substitution $i = M^{x+n}O_{\frac{x+n}{2}}$. We take the standard state as that of the pure liquid oxide at the temperature and pressure of interest. We assume that the concentration of an evaporating element is in the Henry's law region, such that its activity coefficient, γ_i, is equivalent to that at infinite dilution, γ_i^∞. Where γ_i^∞ = 1, the solution of component i in the liquid is ideal. Likewise, when the Langmuir evaporation coefficient α_e is unity, Langmuir evaporation is considered ideal. As the values of α_e and γ_i^∞ are not known *a priori*, it is convenient to define a modified equilibrium constant, K^*:

$$K^* = \alpha_e \gamma_i^\infty K. \quad (6)$$

It is the composite parameter K^* that will be determined from the experiments. For some elements, K and γ_i^∞ are known from independent equilibrium thermochemical measurements, allowing α_e to be calculated using eq. 6. Alternatively, if α_e is defined then γ_i^∞ may be computed by the quotient K^*/K. With this simplification, eqs. 5 and 6 may be substituted into eq. 3, giving:

$$dX_i = -\frac{K^*_{(4)}}{f(O_2)^{n/4}} \frac{3}{r\rho} \sqrt{\frac{M}{2\pi RT}}\, dt \tag{7}$$

Integrating eq. 7 with respect to dX_i and dt yields:

$$\frac{X_i^t}{X_i^0} = \exp\left(-\frac{K^*_{(4)}}{f(O_2)^{n/4}} \frac{3}{r\rho} \sqrt{\frac{M}{2\pi RT}} (t - t_0) \right) \tag{8}$$

Equation 8 returns the mole fraction of element i remaining in the melt after a given time, t, (X_i^t) relative to its initial mole fraction X_i^0, a ratio that is experimentally-measured. It has three refinable parameters: the physically significant quantities K^* and n, and t_0, a lag time that depends on the experimental arrangement (*e.g.*, heating time). They are found by minimising the misfit of $\frac{X_i^t}{X_i^0}$ calculated by eq. 8 to the measured value, summed over a set of N experiments at a single temperature and run time but variable $f\mathrm{O_2}$ by non-linear least squares:

$$\chi^2(K^*, n, t_0) = \sum_N \left(\frac{\frac{X_i^t}{X_i^0}_{meas} - \frac{X_i^t}{X_i^0}_{calc}}{s\left(\frac{X_i^t}{X_i^0}_{meas}\right)} \right)^2, \tag{9}$$

where s denotes the standard deviation. The values of K^* and n are derived solely from fits to the experimental data using eq. 9 and do not depend on any *a priori* knowledge of thermodynamic quantities. By default, t_0 is set to 0 but is refinable within the limits $0 \leq t_0 \leq t$.

Plotted against $\log f\mathrm{O_2}$, $\frac{X_i^t}{X_i^0}$ varies as a sigmoid, where n determines the slope. If the oxidation state of an element in the melt is known, then that in the gas may be inferred from the slope of the curve defined by the experimental data. If $n > 0$, the oxidation state of the element in the gas is lower than that in the liquid, and vice-versa. The change in element volatility with $f\mathrm{O_2}$ becomes sharper (steeper slopes) as n diverges from 0. The K^* controls the displacement of the curve along the $\log f\mathrm{O_2}$ axis, where higher values of K^* result in lower $\frac{X_i^t}{X_i^0}$ (*i.e.*, more evaporative loss), all else being equal. At constant temperature, a systematic increase of K^* with run time signals a non-zero t_0 (evaporation begins only after some time, t_0).

Values of $p_{i,sat}$ reflect the sum of each of the possible vaporisation reactions that may be written between all relevant components containing *i* in the melt, and all gas species containing *i* in the vapour. If the element of interest has a given number, N_{liq} of valence states in the melt and N_{gas} species in the gas, there will be (N_{liq}+N_{gas}-1) independent reactions (*e.g.*, one reaction if N_{liq} =1 and N_{gas}=1). We identify five possible scenarios in order of increasing complexity:

1) Congruent associative evaporation with one species in both liquid and gas, the species having the same oxidation states ($n = 0$).

$$\frac{X_i^t}{X_i^0} = \exp\left(-K^* \frac{3}{r\rho}\sqrt{\frac{M}{2\pi RT}}(t - t_0)\right) \quad (10)$$

2) Congruent dissociative evaporation with one metal-bearing species in both liquid and gas, the species having different oxidation states ($n \neq 0$). Elemental loss is given by eq. 8.

3) Congruent dissociative evaporation with a single oxidation state in the liquid and multiple in the gas.

   This equation is a sum of the partial pressures of the gas species involved in the vaporisation of a given element:

$$\frac{X_i^t}{X_i^0} = \exp\left(-\left(\frac{K^*_{(4_a)}}{f(O_2)^{n_a/4}} + \frac{K^*_{(4_b)}}{f(O_2)^{n_b/4}}\right)\frac{3}{r\rho}\sqrt{\frac{M}{2\pi RT}}(t - t_0)\right) \quad (11)$$

   Where *a* and *b* refer to the different stoichiometries of eq. 4.

4) Congruent dissociative evaporation with multiple oxidation states in the liquid and a single gas species.

   The homogeneous equilibrium between two melt oxide components with different oxidation states may be written:

$$\left(M^{x+n}O_{\frac{x+n}{2}}\right)(l) = \left(M^xO_{\frac{x}{2}}\right)(l) + \frac{n}{4}O_2 \quad (12)$$

   The log$K^*_{(12)}$ is related to the equilibrium constant in the pure M-O system by the equation:

$$\log K^*_{(12)} = \log K_{(12)} - \log\left(\frac{\gamma\left(M^{x+n}O_{\frac{x+n}{2}}\right)}{\gamma\left(M^xO_{\frac{x}{2}}\right)}\right). \quad (13)$$

   The melt oxide components $\left(M^{x+n}O_{\frac{x+n}{2}}\right)$ and $\left(M^xO_{\frac{x}{2}}\right)$ are denoted *i* and *j* respectively.

   Expressions for the partial pressure of a given gas species can be substituted into eq. 3 (see Appendix A for derivation) and integrated in a manner identical to that for eq. 8 to give:

$$\frac{X_i^t}{X_i^0} = \exp\left(-\frac{\alpha_e \gamma_j K_{(4)} f(O_2)^{-n_{(4)}/4}}{\left(K_{(12)} f(O_2)^{n_{(12)}/4} \frac{\gamma_j}{\gamma_i} + 1\right)} \frac{3}{r\rho} \sqrt{\frac{M}{2\pi RT}} (t - t_0)\right) \quad (14)$$

Although $K_{(12)}$is given by thermodynamic data in the pure metal oxide system, eq. 14 has an additional degree of freedom, the ratio of the melt oxide activity coefficients, $\frac{\gamma_j}{\gamma_i}$. Therefore eq. 14 requires independent knowledge of $\frac{\gamma_j}{\gamma_i}$ to be able to solve uniquely for K^*.

5) Congruent dissociative evaporation with multiple oxidation states in the liquid and in the gas.

This equation is the sum of the partial pressures of two gas species as derived in eq. 14

$$\frac{X_i^t}{X_i^0} = \exp\left(-\left(\left(\frac{\alpha_e \gamma_j K_{(4a)} f(O_2)^{-n_{(4a)}/4}}{\left(K_{(12)} f(O_2)^{n_{(12)}/4} \frac{\gamma_j}{\gamma_i} + 1\right)}\right) + \left(\frac{\alpha_e \gamma_j K_{(4b)} f(O_2)^{-n_{(4b)}/4}}{\left(K_{(12)} f(O_2)^{n_{(12)}/4} \frac{\gamma_j}{\gamma_i} + 1\right)}\right)\right) \frac{3}{r\rho} \sqrt{\frac{M}{2\pi RT}} (t - t_0)\right) \quad (15)$$

These equations may be applied to any element. New evaporation experiments in the future would provide additional tests on the theory developed herein.

4.0. Results

A total of 48 experiments were performed at temperatures of 1300, 1400, 1500 and 1550 °C with run durations of 15, 60, 120, 720 and 930 minutes and log$f$O$_2$s between air (-0.68) and -10 (Table 2). All experiments quenched to homogeneous glasses (Fig. 1), with the exception of some of the 1300 °C experiments at low fO$_2$, which contain ≈5% microphenocrysts of olivine and spinel (Electronic Annex C), suggesting the liquidus temperature is close to 1300 °C. Samples run on Pt loops at low fO$_2$ experienced minor (≈ 5 %) Fe loss to the wire (Electronic Annex C).

4.1. Contamination and blank runs

Four experiments performed at log$f$O$_2$ = -8 (N = 3) and -0.68 (N = 1) at 1400°C and 1500°C on the FCMAS mixture without trace elements (‘blank’ runs) were analysed to quantify any contamination within the furnace. At log$f$O$_2$ = -8, the concentrations of all 20 trace elements were < 1% of 1000 ppm, with an average of 1.8 ppm (Table 2). These values indicate negligible vapour pressures of volatile elements in the furnace hotspot, ruling out re-condensation and verifying the condition $p_i \approx 0$. In the air experiment (P28/05/18), all elements are present below 3 ppm, excepting Na and K at 92.1 ppm and 77.7 ppm. That Na and K should not have appreciably evaporated after 15 minutes at 1400°C in air suggests they occur as impurities in the major oxides.

In the trace element-bearing experiments, abundances of K and particularly Na, increased through contamination up to 2075 and 20028 ppm from their initial concentrations of 944±128 ppm and 3252±281 ppm in the starting mixture, respectively. Contamination affected only the samples run at

WWU Münster, likely reflecting the experimental history of the furnace and/or its alumina muffle tube. As such, only the experiments performed at RSES ANU (C-17,18/12/15) and IPGP, Paris (P-xx/xx/17,18), which have low background Na contents (Table 2; Tuff and O'Neill 2010) are considered for Li, Na and K.

4.2. Experimental reproducibility

We duplicated four experiments at 1400°C (Table 2). Experiments for pair P09-06-18b and P09-06-18a, were run on Pt- and Re loops, respectively. The concentrations of volatile elements (K, Cr, Cu, Zn, Ga, Ge, Rb, Mo, Ag, Cd, Pb; N = 38) are compared in Fig. 2 and adhere closely to the 1:1 line. The median misfit between the four pairs for elements with non-zero (> 5 ppm) concentrations is 6.0 % relative. This is two- to three-times larger than the analytical RSD (see section 2.2.), reflecting the experimental error. These random errors include the mass and shape of the experimental charge (section 3.0.; Electronic Annex B) as well as measurement of the temperature, run duration and fO_2 (section 2.2.).

4.3. Metal Loops

Because the solubility of an element into metal increases as fO_2 decreases, depletion of some elements in the glasses at low fO_2 may be partially attributable to alloying with noble metal wires. In order to test this hypothesis, the trace element content of wires in 10 experiments (Table 2) were analysed (Electronic Annex C).

No elements other than the metal were detected in the Ir loop experiment (C18/12/15) and three Re loop experiments measured (1M-1/3/16, 1M-1/3/16b and C17/12/15c). For Pt loop experiments, Ga and Cu dissolved into Pt metal, along with very minor Ag (Ag/Pt < 2×10^{-4}) and Pb (Pb/Pt < 7×10^{-4}) in experiments 1M-PS4, 1M-PS5 and 2M-15-07-16f. This latter pair is so volatile that their abundances were already negligible in silicate liquid.

Although Ga/Pt ratios are typically <7×10^{-4}, in one sample, 2M-17-07-16c ($\log fO_2$ = -8, T = 1500°C, t = 60 mins), Ga/Pt reaches $2.4(\pm0.1)\times10^{-3}$. The melt is also strongly depleted in Ga (67.4 ppm) with respect to the run at $\log fO_2$ = -5.5 (775.1 ppm). Gallium abundances in Pt loops (P09-06-18b) and Re loops (P09-06-18a) at 1400°C and $\log fO_2$ -9.23 are similar (439.9 ppm and 409.4 ppm), suggesting that partitioning of Ga into Pt wire has no resolvable influence on the quantity measured in the melt.

The Cu/Pt ratios of the Pt wire reach $4.7\pm2.9\times10^{-3}$, but are highly heterogeneous, reflecting the low diffusion coefficient of Cu in Pt, 10^{-13} m^2/s at 1673 K (Liu et al., 2009). For a 15-minute experiment, Cu would have diffused only 9 μm into the 0.1 mm diameter Pt wire. For a 0.5 cm length with mass of 0.84 mg (≈7% of sample mass), the Cu budget in the wire, assuming 4000 ppm in the affected zone, is 9%. Experiments P09-06-18b (Pt) and P09-06-18a (Re) have similar Cu contents of 40.5 and

11.2 ppm, respectively. It is concluded that the partitioning of any given element into the metal wire has no resolvable effect within experimental error (± 6% relative) on its observed depletion in the silicate melt.

4.4. Elemental Zoning

Implicit in the theoretical framework in *section 3.0.* is the homogeneous distribution of evaporating elements in the liquid. To test homogeneity, element concentrations were measured in each sample with at least three 130 μm laser spots in both the core and rim, often with a few points in between (N = 6-12; Fig. 1). In addition, a representative subset of seven samples (two each at 1300°C, 1400°C, 1500°C and one at 1550°C; Table 2; Electronic Annex C) were analysed in detail by taking linear profiles from rim to core, consisting of ten to fifteen 25 μm spots spaced at 50 μm intervals (Fig. 3a).

Excepting one sample, 2M-15-07-16f, which represents the extremes of lowest temperature (1300 °C), fO_2 (10^{-10} bar) and shortest run time (15 mins) of the experiments, all elements in all other samples measured show no analytically-resolvable compositional zoning from core to rim (Fig. 3b and Electronic Annex C). Homogeneous zoning profiles indicate that the characteristic timescale of evaporation, t_{HKL}, found by solving for t in eq. (8), is greater than the diffusive timescale, approximated by $t_D = r^2/2D$, where D is the diffusion coefficient (see Electronic Annex D). The lack of zoning can therefore set lower limits on the value of D. In sample 2M-15-07-16f, the extent of element zoning is inversely proportional to the fraction remaining after volatile loss. This suggests zoning is more pronounced for elements with higher evaporation rates relative to their diffusion rates. This ratio increases (and hence zoning is more likely) for most elements to lower fO_2, because vaporisation rates increase whereas diffusion rates are constant as long as the melt oxide species is unchanged. Accordingly, only sample 2M-15-07-16f was rejected from the dataset. For the remaining experiments, diffusion in the liquid was not the rate-limiting step controlling measured element abundances, thereby leaving evaporation from the surface.

4.5. Data fitting

Three groups of elements can be classified *i)* 'non-volatile' elements (Mn, Sc, Ti, V, Zr and the REEs) for which no statistically discernible change from their initial concentrations is observed, *ii*) volatile elements that become relatively more volatile with decreasing fO_2 ($n > 0$; Na, K, Cu, Zn, Ga, Ge, Rb, Pb, Ag, Cd) and *iii)* volatile elements that become relatively more volatile with increasing fO_2 ($n < 0$; Cr, Mo). Lithium is similarly volatile over the range of fO_2 investigated. At a given fO_2, loss of elements belonging to groups *ii)* and *iii)* also increases with a) temperature and b) run time. Values of t_0, n and log$K$* fitted to the data for all volatile elements are shown in Table 3.

4.5.1. Congruent Dissociative Evaporation with one metal-bearing species in both liquid and gas, the species having different oxidation states

One electron (n = 1) reactions (Na, K, Rb, Cu, Ag)

The order of alkali volatility observed in the experiments increases down the group; Li < Na < K < Rb (Fig. 4a-c), in line with the equilibrium vapour pressures above their pure oxides (Lamoreaux and Hildenbrand, 1984). All alkali metals exist in silicate melts as $M^{+}O_{0.5}$ species (*e.g.*, Charles 1967). Lithium is deal with separately owing to its distinct vaporisation behaviour.

At 1400 °C, sodium and potassium become increasingly volatile at low fO_2 (Fig. 4a, b). This behaviour results from a lower mean valence state of these elements in the gas compared to the liquid. Using eq. 8 to fit the data, both Na and K conform to an n = 1 reaction (Fig. 4a, b), implying the reaction $M^{+}O_{0.5}(l) = M^{0}(g) + ¼O_2$ (Fig. 4a, b). This stoichiometry is supported by thermodynamic data that show the overwhelming stability of the monatomic gas above $Na_2O(s)$ and $K_2O(s)$ (Lamoreaux and Hildenbrand, 1984), and above natural silicate melts from Naughton et al. (1971), De Maria et al. (1971) *via* Knudsen Effusion Mass Spectrometry (KEMS) and Tsuchiyama et al. (1981) *via* Langmuir evaporation. The higher log$K$* of the evaporation reaction for K (-3.95±0.06) relative to Na (-4.25±0.10) at 1400°C attests to its higher volatility (Fig. 4a, b, Table 3).

Rubidium is more volatile than either Na or K (Fig. 4c). Like Na and K, its dependence on fO_2 is consistent with an n = 1 reaction, meaning Rb^0 is the stable gas species (Lamoreaux and Hildenbrand 1984). In fitting the equilibrium constant of the Rb vaporisation reaction, a positive dependence of log$K$* with the time series (15, 60, 120 minutes) was observed. In order to account for this, an experimental 'lag time' is introduced, which describes the time at which Rb starts evaporating after sample insertion. A best fit is found at t_0 = 14.4 min (863 s), a constant for all time- and temperature series.

Copper is observed to become more volatile at lower fO_2 (Fig. 4d), signalling a lower oxidation state of Cu in the gas relative to the melt. Although copper is expected to be dominantly cuprous (Cu^{+}) in silicate melts at very high fO_2 (*e.g.*, in air), it may also be present as $Cu^{2+}O(l)$ (*e.g.* Schreiber 1987). Only Cu^{+} is detected in alkali-free, CMAS and CMAS+Fe liquids at 1300°C up to ΔFMQ-1.5, (Holzheid and Lodders 2001, and references therein). Nevertheless, to check for the presence of Cu^{2+}, fits to the experimental data were performed for n in eq. 8. At 1300°C, a formal valence of 1.14 is calculated, at 1400°C it is 1.17, 0.84 at 1500°C, and 0.98 at 1550°C, yielding a weighted average of 1.06±0.15. Therefore, $CuO_{0.5}$ is the only stable liquid oxide species considered, meaning n is set equal to 1, implying the stability of $Cu^0(g)$.

Silver is in its 1+ oxidation state in silicate melts, occurring as $AgO_{0.5}(l)$, however, due to its high volatility, its vaporisation stoichiometry is not well constrained by the present set of experiments. The few data points at 1300°C allow the expected one-electron (n = 1) reaction to be fit (Table 3).

Two electron (n = 2) reactions (Zn, Ge, Cd)

The volatility of zinc is very sensitive to fO_2. Although it is less volatile than Cu or K in air, under reducing conditions ($\leq \log fO_2 = -8$), its abundance in the melt is negligible at all temperatures (Fig 5a). The experimental data are best fit with an $n = 2$ reaction, reflecting the evaporation of ZnO(l), its only stable melt component, to Zn^0(g). Thermodynamic data for gases above ZnO(s) also show that Zn exists as Zn^0(g), be it below the IW buffer or in air, though ZnO(g) becomes important <1000 K in air (Lamoreaux et al., 1987). As for Rb, if $t_0 = 0$ in eq. 8, then a positive dependence of log$K$* with time is observed. For Zn, this time dependence is removed for a time lag of 9 minutes ($t_0 = 540$ s), applied to all run durations and temperatures. Log$K$*s increase systematically with temperature (Fig. 5a; Table 3).

The vaporisation behaviour of Ge closely mirrors that of Zn (Fig. 5b). Although in silicate liquids Ge transitions to 2+ at low fO_2, where $Ge^{2+}/\sum Ge = 0.5$ at IW and 1 atm for a CMAS composition (Mare et al., 2016), it exists exclusively as Ge^{4+} over the fO_2 range covered in our experiments. The data are best fit with an $n = 2$ reaction, implying GeO(g) is stable. This is also corroborated by thermodynamic data for vaporisation of GeO_2(s) (Lamoreaux et al., 1987). Like Zn, a constant 'time lag' of $t_0 = 624$ s (10.4 min) accounts for the observed dependence of log$K$* on time. The proportion of Ge lost from the melt is indistinguishable from that of Zn at 1300°C, attested to by their overlapping log$K$*s (Table 3), but at higher temperatures Ge becomes relatively more volatile than Zn (Fig. 5).

Cadmium, like silver, was too volatile to permit assessment of its evaporation stoichiometry; only two experiments contain measurable quantities of Cd, 2M-15-07-16c and 2M-15-07-15d, $\log fO_2 = -0.67$ and -3.44, for 15 min at 1300°C, respectively. Cadmium, which occurs as Cd^{2+} in silicate melts, evaporates as Cd^0(g) over all fO_2 above CdO(s) (Lamoreaux et al., 1987) suggesting $n = 2$, the value adopted for the fitting.

4.5.2. Congruent dissociative evaporation with a single oxidation state in the liquid and multiple in the gas (Li, Ga, Pb)

For an element with a single melt oxidation state, and more than a single species in the gas, the total partial pressure of the element in the gas phase is the sum of two or more partial pressures (eq. 11). This applies to the vaporisation of Li, Ga and Pb over the T-fO_2 conditions investigated.

The vaporisation behaviour of Li is distinct from that of other alkali metals; it is equally volatile at high fO_2 as it is at low fO_2 (Fig. 6a). The high-temperature gas species of Li above Li_2O(s) are Li(g), Li_2O(g), and LiO(g) (*e.g.*, Kimura et al. 1980), of which Li_2O(g) is the most stable (Lamoreaux and Hildenbrand, 1984). However, since $p(Li_2O)$ is proportional to $a(LiO_{0.5})^2$, for $a(LiO_{0.5}) \approx 10^{-3}$ as in our experiments, Li_2O is no longer the predominant gas species, leaving Li(g) and LiO(g) (see Electronic Annex E). Lithium depletion is generally observed in long (≥120 minute) duration experiments at 1400°C, and only these runs are fit. The time series in air gives a log$K$* for the reaction $LiO_{0.5}$(l) +

¼O_2 = LiO(g) of -3.39, whereas at logfO_2 = -8 the log$K$* for $LiO_{0.5}$(l) = Li(g) + ¼O_2 is -5.36 (Table 3, Fig. 6a).

No Ga evaporation is observed at 1300°C, but at higher temperatures Ga becomes more volatile at lower fO_2 with close to an n = 2 stoichiometry (Fig. 6b). Since Ga occurs as $GaO_{1.5}$ in silicate melts, there is no suitable Ga-bearing gas species that would result in an n = 2 reaction. Above Ga_2O_3(s), the stable gas species is Ga_2O(g) (Burns, 1966; Lamoreaux et al., 1987), whose partial pressure is proportional to fO_2 (an n = 4 reaction). However, as for Li, $p(Ga_2O)$ is proportional to $a(GaO_{1.5})^2$, meaning its stability decreases sharply as the activity of $GaO_{1.5}$ in the melt falls (Electronic Annex E), such that it is stable only below IW-1 at 1700 K for $a(GaO_{1.5}) = 10^{-3}$ (1000 ppm). Instead, the data is fit by a combination of the n = 1 reaction involving GaO(g) and the n = 3 reaction with Ga(g) (Table 3).

Lead is lost rapidly from the melt, and measurable amounts remain only in runs performed at 1300°C and at high fO_2 at 1400°C. In all cases, Pb becomes more volatile with decreasing fO_2 with an observed value of n that is close to 1 (Fig. 6c). In silicate melts, Pb is present as $Pb^{2+}O$, be it at oxidised (≈NNO) or reduced (≈IW) conditions (Watson et al., 1997; Wood and Halliday, 2010). Evaporation of pure PbO(s, l) shows that Pb(g) is dominant below IW, both Pb(g) and PbO(g) are found between IW and air, above which the oxidised species predominates (Lamoreaux et al., 1987; Kobertz et al., 2014; Kobertz, 2019a). As such, both the n = 0 and n = 2 reactions are fit to the experimental data. The partial pressures of Pb(g) and PbO(g) are found to be similar (Table 3) to reproduce the $n \approx 1$ slope of the data.

4.5.3. Congruent dissociative evaporation with multiple oxidation states in the liquid and a single gas species (Mo)

Oxygen fugacity may also influence the oxidation state of a metal oxide dissolved in a silicate melt. This is the case for molybdenum, whose two silicate melt components, $Mo^{4+}O_2$(l) and $Mo^{6+}O_3$(l) (Holzheid et al., 1994; O'Neill and Eggins, 2002) are related by $(fO_2)^{1/2}$ (see Appendix A).

Unlike the aforementioned elements, Mo becomes increasingly volatile at increasing fO_2 (Fig. 7a), reflecting the higher mean oxidation state of Mo in the gas phase compared to the silicate melt. Because the melt has $Mo^{4+}/\sum Mo < 1$, this behaviour implies the presence of $Mo^{6+}O_3$(g). Indeed, calculation of Mo gas species from thermodynamic data (Chase, 1998) shows the clear predominance of MoO_3(g) at all fO_2 > IW-2.5 (Electronic Annex E), and hence only this species is considered in fitting the experimental data.

Because Mo^{4+}/Mo^{6+} of the melt decreases with $(fO_2)^{1/2}$, the effective value of n must also decrease as fO_2 increases. This behaviour necessitates the use of eq. (14) to fit the data. Unique solutions for $p(MoO_3)$ require that $\gamma(MoO_3)$ and $\gamma(MoO_2)$ are known. Here, a value of $\gamma(MoO_3) = 0.3$ is chosen

from CMAS liquids (O'Neill and Eggins, 2002). The slope of the data (n) with fO_2 depends on $\gamma(MoO_3)/\gamma(MoO_2)$, with a best fit across the experimental range found at a ratio of 20.7. These assumptions render the values for the log$K$*s listed in Table 3 approximate.

4.5.4. Congruent dissociative evaporation with multiple oxidation states in the liquid and in the gas (Cr)

Chromium, like Mo, becomes more volatile from silicate melts at increasing fO_2 (Fig. 7b) because Cr in the gas has a higher mean valence than in the liquid. In the liquid, both Cr^{2+} and Cr^{3+} occur (*cf.* Berry and O'Neill 2004), while four Cr-bearing gas species are stable at high temperatures; Cr(g), CrO(g), CrO_2(g) and CrO_3(g). However, only CrO_2(g) is important for IW < fO_2 < FMQ+3, with CrO_3(g) only becoming dominant in air, though its stability increases to lower temperatures (see Electronic Annex E). Tungsten also has oxidised gas species; WO_2 and WO_3 (see also Fegley and Palme 1985; O'Neill 1991), indicating that this is a general feature of Group VI metals.

Two conditions are imposed in the fitting *i)* $\gamma(CrO) = 3$ (Pretorius and Muan, 1992) and *ii)* the $\gamma(CrO_{1.5})/\gamma(CrO)$ ratio at 1400 °C is fixed at 6.13 to give a log$K$* of 2.26 for the equilibrium CrO(l) + ¼O_2 = $CrO_{1.5}$(l) (at an optical basicity of 0.645 for the ferrobasalt; Berry et al. 2006) and is taken to remain constant at all temperatures. Fitting with CrO_3(g) did not improve the misfit and was therefore neglected, hence the data was fit using eq. (14) with CrO_2(g) as the stable species. The 1300°C experiments are anomalously more depleted than at higher temperatures and were not fit. For these reasons, the log$K$*s derived from fitting Cr data shown in Table 3 are semi-empirical.

4.6. Evaporation coefficients and activity coefficients of metal oxide species in silicate melts

In these experiments, gas speciation and thus reaction stoichiometries were not measured, but inferred from fits to concentration-T-fO_2 relations (Figs. 4 – 7), the potential complexity of which limits the extraction of reliable thermodynamic quantities (K*, n) to elements with simple vaporisation stoichiometries (eq. 8, 10). The sum of the experimental uncertainties that may affect precise determination of K* and n, including sample properties (size, shape, density) and other kinetic factors that may influence vaporisation rate (diffusion-limited evaporation, gas flow rate), is relatively small (±6%; section 4.2.). As the determination of n relies on how $\left(\frac{X_i^t}{X_i^0}\right)$ changes relative to other experiments in a given fO_2 series, it depends only on these random experimental variables and is derived with good precision and accuracy.

An additional experimental uncertainty arises for Rb, Zn and Ge because of the time lag from sample insertion to vaporisation (t_0 = 9 – 14 minutes; Table 3), which almost coincides with measured heating times (4 – 7 minutes, section 2.1.). In equilibrium techniques such as KEMS, it is routine to run a

standard material with known partial pressures under identical conditions (Margrave, 1967; Drowart et al. 2005) to identify any systematic errors (*e.g.*, choice of *r*, effect of t_0, deviations from Langmuir conditions), thereby calibrating K^* values. This was not done for these experiments. Therefore, although K^* values are relatively precise (≈±5% to ±30%; Table 3), their accuracy is harder to quantify.

Here, accuracy is assessed by comparing the experimentally-determined equilibrium constant of the vaporisation reaction of the oxide component from silicate melts (K^*), with the known equilibrium constant for the equivalent vaporisation reaction of the pure oxide (K) calculated from thermodynamic data (*e.g.*, Lamoreaux et al. 1987; Chase 1998; Glushko et al. 1999). The values K^* and K are related by eq. 6, and are not equivalent if γ_i^∞ or α_e deviate from unity. For $\frac{K^*}{K} > 1$ the vapour species is favoured over the liquid component of the silicate melt relative to the same reaction between the pure liquid oxide and gas, and vice-versa.

Activity coefficients of metal oxide species in silicate melts vary by orders of magnitude with composition (*e.g.*, Rammensee and Fraser 1982; Wood and Wade 2013), temperature (*e.g.*, Reyes and Gaskell 1983) and metal oxidation state (O'Neill and Eggins, 2002), with theoretical limits between $1/\infty < \gamma_i < \infty$. However, for many trace elements, activity coefficients remain poorly known. Constraints on Langmuir evaporation coefficients are similarly sparse. Because the HKL equation describes only the flux of particles striking a surface, α_e was introduced *a posteriori* as an *ad-hoc* adjustment to account for the energy required in the transformation of element i from the condensed to gaseous state (see Ackermann et al. 1962) and thus has theoretical limits $1/\infty < \alpha_e \leq 1$. Unlike γ_i, α_e may depend not only on liquid composition, temperature and redox state, but also on the activation energy of evaporation, surface properties, vaporisation rate and nature of the gas phase (*e.g.*, Knacke and Stranski 1956; Persad and Ward 2016) and hence cannot be determined *ab-initio*. Although evaporation coefficients from simple solid metal or binary metal oxides are <1, the equivalent liquids have α_e of unity (Burns, 1966; Safarian and Engh, 2013; Shornikov, 2015). For vaporisation of major components from silicate melts Alexander (2002) and Fedkin et al. (2006) employed MELTS to calculate γ_i and found $0.01 < \alpha_e < 0.5$ from fits to experimental data. Given the potential variation of α_e and γ_i^∞ in our system, values of α_e are calculated using independent estimates of γ_i, providing a test of the accuracy of our theoretical framework (section 3.0.).

Evaporation coefficients calculated from eq. 6 are shown in Table 4. The activity coefficients of Na and K are well-characterised (O'Neill, 2005; Grant and Wood, 2008; Borisov, 2009; Mathieu et al., 2011) due to their importance in the vaporisation of chondrules (*e.g.*, Tsuchiyama et al. 1981; Shimaoka and Nakamura 1991; Georges et al. 2000) and lunar basalts (De Maria et al., 1971; Gibson and Hubbard, 1972; Gooding and Muenow, 1976; Donaldson, 1979). From the Na vapour pressures measured over natural basalts by DeMaria et al. (1971) and Gooding and Muenow (1976), activity

coefficients ≈ 10^{-3} were calculated. Mathieu et al. (2008) also report $\gamma_{NaO_{0.5}}$ = 10^{-3} in the CMAS system and 8.4×10^{-4} – 2.2×10^{-3} in the simpler CMS system (Mathieu et al., 2011). This gives $\alpha_{e,NaO_{0.5}}$ between 0.3 – 1.7 for our experiments at 1400 °C. Values of $\gamma_{KO_{0.5}}$≈ 5×10^{-5} to 7×10^{-4} were calculated from De Maria et al. (1971), Gooding and Muenow (1976) in natural basalts and Hastie and Bonnell (1985) for the KFCAS system, resulting in $\alpha_{e,KO_{0.5}}$ from 0.3 to 3.4 at 1400 °C.

Reyes and Gaskell (1983) found γ_{ZnO} = 0.25, 0.43, and 0.58 at 1400, 1500 and 1550 °C, respectively in CAS melts by transpiration, yielding $\alpha_{e,ZnO}$ ≈ 2. Holzheid and Lodders (2001) determined $\gamma_{CuO_{0.5}}$ = 10±1 at 1300°C for Fe-poor basaltic compositions, returning $\alpha_{e,CuO_{0.5}}$ = 2.4±0.8. If the trends of K^* are extrapolated with temperature to 1650°C, then the $\gamma_{CuO_{0.5}}$ = 3.5 determined by Wood and Wade (2013) at this temperature gives $\alpha_{e,CuO_{0.5}}$ = 1.2. The two stable gases species evaporating over PbO(l) allows $\alpha_{e,PbO}$ to be calculated from both reactions (Table 4). Although the two points for Pb evaporation do not permit extrapolation to higher temperatures, $\alpha_{e,PbO}$ ranges between 0.3 and 1.7 when calculated from γ_{PbO} of Wood and Wade (2013), 0.22, at 1650°C for an SiO_2-rich melt.

Therefore, evaporation coefficients are close to unity (within a factor of 2 - 3) for all elements for which *i)* the experimentally determined *K** is robust, *ii)* melt compositions and temperatures are similar to literature data, and *iii)* the activity coefficient is well-determined (particularly Na, Cu and Zn). Based on these observations α_e is set to 1 and γ_i^∞ is calculated from *K*/K* (eq. 6; Table 4, Fig. 8). The uncertainties on the reported activity coefficients represent only the precision on the fit, and do not include the uncertainties in α_e just discussed.

Aside from Li, alkali dissolution in silicate melts is strongly non-ideal (γ_i^∞ << 1), meaning their volatilities are much reduced from those of pure alkali oxides. Furthermore, alkali metal oxide activity coefficients decrease in the order Li>>Na>K>Rb>(Cs) (*cf.* Charles, 1967; Borisov, 2009), a hierarchy that is inversely proportional to their volatilities.

Zinc oxide activity coefficients, like other divalent, first-row transition metals (O'Neill and Eggins, 2002), are close to unity but show a weak positive dependence on temperature. This behaviour is mimicked by $\gamma_{GeO_2}^\infty$, albeit at lower absolute values. By contrast, $\gamma_{CuO_{0.5}}^\infty$ is >1, (see also Holzheid et al., 2001; Wood and Wade, 2013), and decreases to higher temperatures. In these three cases, γ_i^∞ tends towards unity at high temperatures, a phenomenon described by the van't Hoff equation:

$$\frac{d\ln\gamma_i^\infty}{d(1/T)} = -\frac{\Delta H}{R}, \qquad (16)$$

where ΔH refers to the partial molar enthalpy of solution of i in the silicate melt. For $CuO_{0.5}$, this is calculated at 121±12 kJ/mol, -143±15 kJ/mol for ZnO (compared with -135 kJ/mol from Reyes and Gaskell, 1983) and -147±25 kJ/mol for GeO_2 over the temperature range 1573 to 1823 K.

4.7. Gibbs Free Energy of vaporisation using the '2nd law method'

The modified equilibrium constants of vaporisation reactions (K*) may be converted into Gibbs Free Energies (ΔG^*):

$$\Delta G^* = -RT \ln K^*. \quad (17)$$

The asterisk denotes that the Gibbs Free Energy of reaction includes *i)* the non-ideality of trace element dissolution in silicate melts and *ii)* any deviation of the evaporation coefficient from unity and/or variation with temperature. Hence, ΔG*s calculated are relevant only to the investigated melt composition at 1 bar pressure and temperatures between 1573 and 1823 K.

Variation of ΔG^* of a volatilisation reaction against the absolute temperature, T, in an Ellingham diagram, results in a straight line (Fig. 9), independent of run time. This confirms that a reproducible, thermally-activated process is controlling elemental loss, namely, the equilibrium partial pressure.

At constant total pressure, the Gibbs-Helmoltz equation is:

$$\Delta G^* = \Delta H^* - T\Delta S^* \quad (18)$$

Hence, the slope of the line is equivalent to $-\Delta S^*$ (entropy) and its intercept ΔH^* (enthalpy), which are average values determined for the mid-point temperature over the temperature range. This is a 2nd law treatment of the vaporisation data, requiring two or more measurements of the equilibrium constant, and is analogous to the integration of the Clausius–Clapeyron equation generally used for interpretation of vapour pressure data (Drowart and Goldfinger, 1967; Drowart et al., 2005; L'vov, 2007). It implicitly assumes that ΔH^* is much greater than the product of ΔC^o_P (molar heat capacity at constant pressure) and temperature over the interval of interest, such that slopes can be approximated as linear within experimental uncertainty.

Values for the entropy and enthalpy of reaction, along with those for the pure system, are listed in Table 5. Typical relative standard deviations for ΔH^* and ΔS^* range from 5 – 15 %, as compared with 1 – 2 % for KEMS measurements for vaporisation of multicomponent systems (silicate melt, Markova et al., 1986, Fraser and Rammensee, 1987; olivine, Costa et al. 2017) or pure metal oxides (Kobertz 2019a, b). It is observed that ΔH^* and ΔS^* are positively correlated (Fig. 10a), indicative of enthalpy-entropy compensation, where ΔG tends to a common value at infinite temperature (see Exner 1973; Kemeny and Rosenberg 1973). The same is true of thermodynamic data in the pure M-O system, though less marked (compare Fig. 10a and b). The gross effect of γ_i^∞ is to smooth out variability in ΔH^* *vs.* ΔS^* compared with ΔH^o and ΔS^o. Activity coefficients of divalent first-row transition metal cations are ≈1 in geologically-relevant silicate melts (Pretorius and Muan, 1992; Ohta and Suito, 1995; Holzheid et al., 1997; O'Neill and Eggins, 2002) and furthermore depend on melt composition

in a similar manner (O'Neill and Eggins, 2002). With these caveats in mind, their ΔH^o and ΔS^o from pure system thermodynamic data (Chase, 1998) are also shown in Table 5.

4.8. Comparison with previous work

Tsuchiyama et al. (1981) studied Na evaporation from chondrule-like melts at varying log$f$O$_2$ (-5 to -10) between 1450 and 1600 °C (Fig. 11a). Their data are well-modelled by eq. (8), conforming to an n = 1 reaction with log$K$*s that define $\Delta G^* = 444.4(\pm 0.2) - 0.166(\pm 0.003)T$ (kJ/mol) for their 'composition 1'. Na evaporation from 'composition 2', with SiO$_2$ (43.55 wt. %) and FeO^T (18.52 wt. %) contents similar to the ferrobasalt, has log$K$* 0.5 log units higher (log$K$* = -3.30 at 1586 °C), suggesting a compositional control on $\gamma_{NaO_{0.5}}$ (*cf.* O'Neill 2005; Borisov 2009; Mathieu et al. 2011).

The experiments of Kreutzberger et al. (1986) were performed on a $Di_{75}An_{25}$ melt. The volatility behaviour of Na, K and Rb is fit as a function of time (Fig. 11b) using an n = 1 reaction. A uniform sample radius of 0.0015 m and density of 2750 kg/m^3 was assumed. The order of volatility observed (Na < K < Rb) is in good agreement with this work, and the fitted log$K$*s for Na (-4.15) and Rb (-3.04) overlap with our determination (-4.25±0.10 and -3.12±0.10, respectively, Table 3), while that of K is much higher (-3.26 compared to -3.95±0.06, Table 3).

Norris and Wood (2017) performed vaporisation experiments on a trace element-doped MORB melt, stirred in an Ni crucible. The agreement in the order of volatility for elements common in both studies is reasonable. At log$f$O$_2$ = -10 and 1300 °C, Norris and Wood (2017) show Cr < Ga < Zn < Pb ≈ Cu < Ag < Ge < Cd (Fig. 11c), compared with Cr < Ga < Cu < Zn ≈ Ge < Pb < Ag ≈ Cd in this work. Given that not all variables (*e.g.*, stirring rate, eccentricity) were kept constant between their experiments, element depletion factors in Norris and Wood (2017) were normalised to a second element, *j*, such that physical factors affecting element loss cancel, leaving:

$$\frac{\ln\left(\frac{X_i^t}{X_i^0}\right)}{\ln\left(\frac{X_j^t}{X_j^0}\right)} = \frac{K_i^*}{K_j^*}(fO_2)^{\frac{\Delta n_{j-i}}{4}}\sqrt{\frac{M_i}{M_j}}. \quad (19)$$

Here, j = Zn, and hence depletion of an element ($\frac{X_i^t}{X_i^0}$) by a single vaporisation reaction will be proportional to a constant multiplied by $(fO_2)^{\frac{\Delta n_{j-i}}{4}}$ (eq. 19). Relative to the Zn vaporisation reaction (n =2), Δn_{Zn-Cu} = 1 and best fits are found with $\frac{K_{Cu}^*}{K_{Zn}^*}$ = 10^3; this compares with 10^1 from our work (Table 3). For Pb, due to the reducing conditions only Pb(g) is considered, hence Δn_{Zn-Pb} = 0 and $\frac{K_{Pb}^*}{K_{Zn}^*}$ ≈ 1.2, in reasonable agreement with $\frac{K_{Pb}^*}{K_{Zn}^*}$ = 4 determined herein (Table 3). Similarly, only Ga(g) should be stable below < FMQ (Electronic Annex E), thus Δn_{Zn-Ga} = -1. Satisfactory agreement is

found when $\frac{K^*_{Ga}}{K^*_{Zn}}$ = 10^{-3}. For Δn_{Zn-Ge} = 0 as determined in this work, no constant value fits the gradual decline in $\frac{X^t_{Ge}}{X^0_{Ge}}$ with log$f$O$_2$ observed, suggesting that Δn_{Zn-Ge} increases with decreasing fO$_2$. Phenomenologically, this is consistent with increasing proportions of Ge^{2+} in the melt <IW, potentially explaining its more volatile behaviour in Norris and Wood (2017) than reported here.

5.0. Discussion

Our approach is to provide experimental constraints on element vaporisation from silicate melts under a set of known and controlled experimental conditions rather than to replicate any specific natural process. As such, use of the results to quantify vaporisation in natural samples is associated with numerous caveats. We assume the synthetic ferrobasalt is a good approximation of natural melts, however, activity coefficients can vary with composition (O'Neill and Eggins, 2002; Borisov, 2009; section 4.6.) meaning our results are only indicative for other basaltic melts. Moreover, the absence of major volatiles (H, C, N, S and the halogens) in our experiments prevents their complexation of metal-bearing gas species, which could otherwise modify element volatility (Schaefer et al., 2012; Fegley et al., 2016; Renggli et al., 2017). Nevertheless, even in volatile-laden volcanic gases, higher temperatures and lower pressures favour simple species (monatomic gases, oxides) with respect to associated molecules (*e.g.*, Churakov et al., 2000). At low pressures (≤1 bar), the major volatiles are either sparingly soluble in silicate melts (*e.g.*, Carroll and Webster 1995) and/or highly volatile, leaving O_2 as the major volatile species. Such conditions may be relevant to degassed planetesimals, with escape velocities too low to retain an atmosphere of light elements (*cf.* Hin et al. 2017), as well as volatile-poor chondrules (Fedkin and Grossman, 2013; Oulton et al., 2016), tektites (Chapman and Scheiber, 1969; Koeberl, 1986) and other 1 atm furnace experiments (Ertel et al., 1997). Experimental and thermodynamic studies show that, in a vacuum, silicate vaporisation sets the fO$_2$ of the vapour phase close to the FMQ buffer (De Maria et al., 1971; Visscher and Fegley, 2013; Costa et al., 2017), precisely the conditions covered by our experiments. We hereafter discuss our results in the context of evaporation of planetary bodies.

5.1. Equilibrium evaporation and evaporation temperatures

Experimentally-derived thermodynamic data (Table 5), permit calculation of evaporation temperatures. The partial pressure of an element i in the gas phase is related to its mole fraction (X_i^{vap}) and total pressure, P_T:

$$p_i = X_i^{vap} P_T. \quad (20)$$

Because the fraction of i in the gas (f_i^{vap}) and in the liquid, f_i^{liq} must sum to 1, and $f_i^{liq} = X_i^{liq}/X_0^{liq}$ where X_0^{liq} is the original mole fraction of element i, it follows that:

$$p_i = \left(X_0^{liq} - X_i^{liq}\right)P_T. \quad (21)$$

Substituting eq. (21) into eq. (5), combining it with eq. (17) and solving for the temperature (T_e) at which a fraction, f, of an element, i, has evaporated, gives, for congruent dissociative evaporation reactions (eq. 4):

$$T_{e,i}^{f} = \frac{-\Delta H_i^*}{\left(R\left(\frac{n}{4}\ln fO_2 + \ln P_T + \ln\frac{f_i^{vap}}{\left(1-f_i^{vap}\right)}\right) - \Delta S_i^*\right)}. \quad (22)$$

For more complicated evaporation stoichiometries $T_{e,i}^{f}$ is computed analytically. Although 50% condensation temperatures are calculated by convention, any fraction evaporated could be chosen. Here, because the temperatures of the experiments range between 1573 K and 1823 K, it is favourable to keep the eventual calculated T_e^f within this range to minimise extrapolation and therefore uncertainties. As such, 1% evaporation temperatures, T_e^1, are calculated, at log$f$O$_2$s; -10 ($T_e^{1,-10}$), -5 ($T_e^{1,-5}$) and in air, $T_e^{1,air}$ (Table 6).

Relative to nebular T_c^{50} (Lodders, 2003, Fig. 12a; Wood et al. 2019, Fig. 12b), the higher total pressures (1 bar) and oxygen fugacities at which $T_e^{1,-10}$ are calculated offsets them to higher temperatures (eq. 22; Fig. 12). These effects notwithstanding, the correlation between $T_e^{1,-10}$ and T_c^{50} for lithophile elements, (Cr), Mg, Li, Mn, (Ga), Na, K, Rb and Zn, is excellent (r^2 = 0.93 for Lodders, 2003; r^2 = 0.90 for Wood et al. 2019). Siderophile and chalcophile elements tend to have relatively lower $T_e^{1,-10}$ than their lithophile counterparts at a given T_c^{50} (Fig. 12). This likely reflects their early condensation, under nebular conditions, into an Fe-alloy or sulfide phase. An exception is Pb, for which Lodders (2003) calculated T_c^{50} as 727 K by assuming ideal condensation into Fe metal whereas Wood et al. (2019), considering its low solubility in Fe as Pb^0 and in FeS as PbS, calculated 495 K. As such, Pb sits below and above, respectively, the lithophile element trends in Fig. 12. This highlights not only the need for solubility data for trace elements in major nebula condensate phases to better constrain T_c^{50}, but also that element volatility is sensitive to the phases present (silicate melt in our experiments; solid FeS, silicates and metal in the solar nebula).

A volatility scale of elements evaporating from a ferrobasaltic liquid at 1 bar (Table 6) as a function of fO$_2$ is shown in Fig. 13. Lead has T_e^1 within liquidus temperatures of basaltic rocks (≈ 1573 K), even at oxidising conditions, suggesting Pb (and more volatile elements such as Tl and Cd) might be slightly volatile in subaerial eruptions (see also Norman et al. 2004; Johnson and Canil 2011; Vlastélic et al. 2013; Edmonds et al. 2018). Zinc and Ge show similar volatility over all fO$_2$ due to

their equivalent n = 2 vaporisation reactions, where deviations in Zn/Ge should signal metal segregation, as Ge is more siderophile than Zn (*e.g.*, Siebert et al. 2011; Wood et al. 2014). Alkali metal volatilities increase monotonically down Group I, with Na, K and Rb showing identical vaporisation stoichiometries. Lithium is the least volatile of the alkalis, except under oxidising conditions, and becomes more refractory than either Ni (<FMQ-2) or Co (<IW+1). Manganese also becomes more volatile than Li at ≈IW-6, a prediction verified by the observation of slightly decreasing Mn/Li with increasing volatile depletion in carbonaceous chondrites (Siebert et al., 2018) and lower T_c calculated by Wood et al. (2019). Thus, Mn (and Fe and Mg) vaporises sparingly in oxidising, post-nebular settings. The depletion of these elements by volatility is therefore a hallmark of nebular depletion where fO_2 is sufficiently low to render them volatile (O'Neill and Palme, 2008). Although Cr is relatively refractory at low fO_2, it becomes more volatile with fO_2, such that $T^1_{e,Cr}$ = 1785 K in air is lower than all elements studied except Pb. The same progression is observed for Mo (and W), and hence ratios of the abundances of these Group VI elements to volatile metals with opposite behaviour (n > 0) are able to constrain fO_2 during evaporation (see also Fegley and Palme 1985).

5.2. Origin of moderately volatile elements in the terrestrial planets

Element depletion factors relevant to planet-building processes after dispersal of the solar nebula are conveniently expressed by normalising to the main lithophile element in rocky planets, Mg. These depletion factors, defined as $\frac{X_i^t}{X_i^0} / \frac{X_{Mg}^t}{X_{Mg}^0}$, were calculated as a function of temperature (1373 K to 1973 K) and fO_2 (FMQ-4 to FMQ+4) at 1 bar, and plotted in Fig. 14.

Differences in molar mass play only a secondary role in controlling $\frac{X_i^t}{X_i^0}$ (eq. 19) because equilibrium partial pressures of stable gas species of moderately volatile elements vary by orders of magnitude among one another. This is manifest in the pronounced discrimination of MVE abundances in evaporation residues at a given fO_2 and T. That is, the most volatile MVEs (*e.g.*, Pb and Ge), will be quantitatively vaporised before evaporation of more refractory elements, including Fe and Mg, has begun (Fig. 14). Evaporation therefore results in a near-binary distribution of elements in the residue; those that are preserved and those that are vaporised, with the transition between them defining a sharp 'cut-off' temperature. While this cut-off temperature will vary with total pressure and fO_2 (eq. 22), the general step-function form of the MVE pattern in the residuum is insensitive to these variables, or indeed to the accuracy of the K* values. The binary element distribution results from *relative* differences in partial pressures among MVEs, making it a diagnostic feature of single-stage evaporation.

Urey (1952, 1954) first proposed that volatile element abundances could be used as 'cosmothermometers' to track accretion temperatures of planetary materials, an approach rendered quantitative by the calculation of condensation temperatures (Larimer, 1967). The fact that MVEs are easily decoupled during evaporation was recognised, and employed as an argument by Anders (1964) and further developed by Keays et al. (1971), Laul et al. (1973), Larimer (1973) and Grossman and Larimer (1974) to exclude vaporisation as a major contributor to the gradual depletion of MVE with volatility observed in chondrites as there is *"no one temperature at which they will all be condensed to the same fractional degree"*. As in chondrites, the abundances of lithophile MVEs in the BSE decline smoothly as a function of volatility (Fig. 14).

Volatile depletion in the Earth must reflect both *i)* the fraction of the element in the atmosphere (Fig. 14) and, unlike chondrites, *ii*) its proclivity to escape. Atmospheric escape from Earth is, however, ineffective in fractionating MVEs abundances. Thermally-based Jeans escape requires prohibitively high temperatures (>10000 K) due to the Earth's high escape velocity (11.2 km/s) and would produce a correlation with $M^{-0.5}$, which is not observed (Sossi and Fegley, 2018). Both hydrodynamic escape (Hunten et al., 1987; Genda and Abe, 2003; Young et al. 2019) and outflow of ionised particles (Yamauchi and Wahlund, 2007) are nearly mass-independent processes, meaning MVE losses should reflect their equilibrium partial pressures (*cf.* Fig. 14).

Many MVE ratios in the Earth are chondritic (*e.g.*, O'Neill and Palme, 2008; Mann et al., 2009; Siebert et al., 2018) suggesting minimal post-nebular perturbation by evaporative processes. Unlike elemental ratios, isotope ratios are readily mass-fractionated during Langmuir evaporation (Humayun and Clayton, 1995; Yu et al., 2003; Wombacher et al., 2004; Richter et al., 2007). Hence, the agreement in MVE stable isotope compositions between Earth and carbonaceous chondrites (*e.g.* Wombacher et al. 2008; Pringle et al., 2017; Sossi et al., 2018) also suggests terrestrial volatile depletion occurred in a similar manner to that in chondrites. Contrastingly, the higher abundance of In ($T_c^{50} \approx 530$ K) relative to Cd ($T_c^{50} \approx 500 – 650$ K) and Zn ($T_c^{50} \approx 700$ K) in the BSE despite its higher siderophilicity and volatility permits deviation from canonical nebular conditions during volatile loss (Wang et al., 2016; Norris and Wood, 2017), though other explanations, including collisional erosion, are feasible (Witt-Eickschen et al. 2009). Indeed, the condensation/vaporisation behaviour of these highly volatile elements ($T_c^{50} < 750$ K), whose abundances flatten out with T_c^{50} in carbonaceous chondrites (Wolf et al., 1980; Humayun and Cassen, 2000; Braukmüller et al., 2018), is poorly understood. Whether these elements also define a constant-abundance plateau in the BSE requires additional work to distinguish between the relative effects of core formation and volatility (*cf.* Wang et al., 2016; Ballhaus et al., 2017). For the MVEs, their gradual depletion with volatility in Earth's mantle, coupled with their chondritic elemental and isotope ratios, appear at-odds with partial evaporation and loss at a single temperature and fO_2 such as may be expected during a giant impact (Fig. 14).

A potential mechanism that could satisfy both isotopic and elemental constraints is the accretion of the Earth from a distribution of partially vaporised bodies. In each body, the elements below a given cut-off temperature are lost entirely while those above it are not lost at all (normalised abundances are '1' above and '0' below), where the cut-off point varies stochastically from body to body. Integration of material from many such bodies, each with its own binary pattern, would sum to a smooth pattern in which MVE depletion correlates with volatility, but whose MVE isotopic composition is dominated by the contributions from material that has seen negligible volatilisation.

By contrast, smaller bodies such as Vesta, the Ureilite and Angrite parent bodies and the Moon record significant depletions, $<10^{-3}\times$ CI, in highly volatile elements (Cd, Ag, Pb, Ge, Zn) coupled with modest losses ($\approx10^{-1}$ to $10^{-2}\times$CI) of the moderately volatile elements, such as Na, K and Ga (Janssens et al., 1987; O'Neill, 1991; Ruzicka et al., 2001) and a lack of depletion in elements more refractory than Li (see also Magna et al. 2006). Volatile element abundances in the Moon exemplify a highly fractionated, binary pattern consistent with single-stage evaporation, where Mg-normalised abundances of Ge, Zn, and the alkalis are very low (Wolf and Anders, 1980), whereas Li and Mn are undepleted relative to Earth's mantle (Fig. 14). Furthermore, these bodies do exhibit fractionated stable isotope signatures in elements such as Zn (*e.g.* Paniello et al. 2012), K (Wang and Jacobsen, 2016), Ga (Kato and Moynier, 2017) and Cl (Boyce et al., 2018); but not Li (Magna et al. 2006), consistent with its retention during volatility-related processes. These lines of evidence are more compatible with a partial evaporation origin, the conditions and mechanisms of which will require quantitative assessment of temperatures, gas compositions, accretion scenarios and vapour loss processes.

Conclusion

In order to determine the behaviour of moderately volatile elements during evaporation of silicate melts, experiments were conducted in 1-atm vertical tube gas-mixing furnaces in which samples of synthetic ferrobasalt in the FCMAS system, doped with 1000 ppm each of Li, Na, K, Cu, Rb, Ga, Ge, Pb, Mn, Mo, Zn, V, Zr, Sc, Ti, La, Gd, Yb, Ag and Cd, were suspended on noble metal wire loops and heated to 1300 °C, 1400 °C, 1500 °C and 1550 °C for between 15 and 930 minutes at logfO_2s between air (-0.68) and -10. Element loss from the melt, as determined from LA-ICP-MS measurements of the quenched glasses, varied strongly with fO_2. Alloying with the metal wire and incomplete diffusion of the element to the surface were unimportant, leaving vaporisation as the sole cause of the observed depletion relative to the starting composition.

The degree of elemental loss depends on the stoichiometries of the vaporisation reaction(s), which have the general form $M^{x+n}O_{(x+n)/2}(l) = M^xO_{x/2}(g) + n/4O_2$. These reactions are solved for the equilibrium partial pressure of the gas species and incorporated into the Hertz-Knudsen-Langmuir equation, enabling element evaporation from a sphere to be quantitatively modelled. Stoichiometries

of the reaction(s), n, and equilibrium constant(s), K^* are calculated from fits to the experimental data. Most MVEs evaporate with $n > 0$, where stoichiometries of 1 (Cu, Na, K, Rb, Ag) and 2 (Zn, Ge, Cd) are common. The Group VI metals, Cr and Mo, show the inverse behaviour ($n < 0$) by virtue of their stable oxide-bearing gas species with oxidation states higher than those in the silicate liquid. The K^* value is the product of the activity coefficient, γ_i, the evaporation coefficient, α_e and the equilibrium constant of reaction (K), the first two of which are not known *a priori*. Evaporation coefficients calculated using literature values for activity coefficients return values near unity, verifying the accuracy of the approach and suggesting evaporation is near-ideal. Given α_e of 1, γ_i of melt oxide components vary by ~10^5, shifting their volatilities compared with evaporation from pure oxides. For all volatile elements, logK^* increases with temperature, which, when converted to ΔG^*, allows a straight line to be fit to the data, where the slope is equal to $-\Delta S^*$ and the intercept ΔH^*.

These fundamental data are useful for understanding vapour loss during chondrule melting, degassing of anhydrous magmas, tektite formation and other 1 atm furnace experiments. Although lithophile elements show good agreement with nebular condensation temperatures at low fO_2, chalcophile and siderophile elements are generally more volatile during evaporation of silicate melts relative to solar nebular environments. Evaporation of a silicate melt at a single temperature and fO_2 results in a near-binary element distribution in the residuum, strongly discriminating the volatile elements from the non-volatile. This type of fractionation among MVEs is observed in small telluric bodies (Moon, Vesta) but not on Earth, where element depletion is a gradual function of volatility. This observation argues against volatile loss from Earth during a giant impact, suggesting that it accreted from already volatile-depleted components.

Acknowledgements

P.A.S. and F.M. were supported by the European Research Council under the H2020 scheme with the grant #637503 (PRISTINE). We are grateful to the Associate Editor Munir Humayun for his measured, thorough and insightful evaluation, advice for re-organisation of the manuscript and broad understanding of the cosmochemical literature and to Executive Editors Marc Norman and Jeff Catalano. We thank Bernie Wood for his input into the use of the HKL equation, experimental considerations, the importance of the evaporation coefficient, and for recommending us to be more circumspect about our thermodynamic treatment, Gokce Ustunisik on the experimental methodology and its relevance to natural processes and an anonymous reviewer for various aspects of the work and for encouraging application of the model to other studies. P.A.S. is thankful to Raúl Fonseca who shared experimental know-how and advice on evaporation experiments, to Bruce Fegley and Katharina Lodders for their keen interest in the experiments, equilibrium evaporation and in-depth calculation of partial pressures using their own codes, and to Frank Richter for highlighting the importance of diffusive effects in the gas during experimental runs. Julien Siebert, Arno Rohrbach, Tahar Hammouda, Bernard Bourdon and Nate Jacobson are thanked for many illuminating discussions.

References

Ackermann R. J., Thorn R. J. and Winslow G. H. (1962) *Some fundamental aspects of vaporization*, AEC Research and Development Report, Argonne National Laboratory, Illinois.

Albarède F., Albalat E. and Lee C.-T. A. (2015) An intrinsic volatility scale relevant to the Earth and Moon and the status of water in the Moon. *Meteorit. Planet. Sci.* **50**, 568–577.

Alexander C. M. O. D. (2001) Exploration of quantitative kinetic models for the evaporation of silicate melts in vacuum and in hydrogen. *Meteorit. Planet. Sci.* **36**, 255–283.

Alexander C. M. O. D. (2002) Application of MELTS to kinetic evaporation models of FeO-bearing silicate melts. *Meteorit. Planet. Sci.* **37**, 245–256.

Anders E. (1964) Origin, age, and composition of meteorites. *Space Sci. Rev.* **3**, 583–714.

Ballhaus C., Fonseca R. O. C., Münker C., Rohrbach A., Nagel T., Speelmanns I. M., Helmy H. M., Zirner A., Vogel A. K. and Heuser A. (2017) The great sulfur depletion of Earth's mantle is not a signature of mantle–core equilibration. *Contrib. to Mineral. Petrol.* **172**.

Bart G., Ikramuddin M. and Lipschutz M. E. (1980) Thermal metamorphism of primitive meteorites-IX. On the mechanism of trace element loss from Allende heated up to 1400° C. *Geochim. Cosmochim. Acta* **44**, 719–730.

Berry A. J. and O'Neill H. S. C. (2004) A XANES determination of the oxidation state of chromium in silicate glasses. *Am. Mineral.* **89**, 790–798.

Blanchard I., Badro J., Siebert J. (2015) Composition of the core from gallium metal–silicate partitioning experiments. *Earth Planet. Sci. Lett.* **427**, 191–201.

Boltzmann L. (1872) Weitere Studien über das Wärmegleichgewicht unter Gasmolekülen. *Sitz.-Ber. Akad. Vienna* **2**, 275–370.

Bonsor A., Leinhardt Z. M., Carter P. J., Elliott T., Walter M. J. and Stewart S. T. (2015) A collisional origin to Earth's non-chondritic composition. *Icarus*, **247**, 291–300.

Borisov A. A. (2009) Influence of SiO_2 and Al_2O_3 on the activity coefficients of alkalis in melts: An experimental study. *Petrology* **17**, 579–590.

Bottinga Y. and Weill, D. F. (1970) Densities of liquid silicate systems calculated from partial molar volumes of oxide components. *Am. J. Sci.*, **269**, 169–182.

Boyce J. W., Kanee S. A., McCubbin F. M., Barnes J. J., Bricker H. and Treiman A. H. (2018) Early loss, fractionation, and redistribution of chlorine in the Moon as revealed by the low-Ti lunar mare basalt suite. *Earth Planet. Sci. Lett.* **500**, 205–214.

Braukmüller N., Wombacher F., Hezel D. C., Escoube R. and Münker C. (2018) The chemical composition of carbonaceous chondrites: Implications for volatile element depletion, complementarity and alteration. *Geochim. Cosmochim. Acta* **239**, 17–48.

Burns R. P. (1966) Systematics of the evaporation coefficient Al_2O_3, Ga_2O_3, In_2O_3. *J. Chem. Phys.* **44**, 3307–3319.

Canup R. M., Visscher C., Salmon J. and Fegley Jr B. (2015) Lunar Volatile Depletion Due To Incomplete Accretion Within An Impact-Generated Disk. *Nat. Geosci.* **8**, 1–6.

Carroll M. R. and Webster J. D. (1995) Solubilities of sulfur, noble gases, nitrogen, chlorine, and fluorine in magmas. In *Reviews in Mineralogy vol. 30: Volatiles in Magmas* (eds. M. R. Carroll and J. R. Holloway). Mineralogical Society of America. pp. 231–279.

Carter P. J., Leinhardt Z. M., Elliott T., Walter M. J. and Stewart S. T. (2015) Compositional evolution during rocky protoplanet accretion. *Astrophys. J.*, **813**, 72.

Chamberlain J. W. and Hunten D. M. (1989) *Theory of Planetary Atmospheres*, 2nd Ed. Academic Press, San Diego.

Chapman D. R. and Scheiber L. C. (1969) Chemical Investigation of Australasian Tektites. *J. Geophys. Res.* **74**, 6737–6776.

Chapman S. and Cowling T. G. (1970) *The Mathematical Theory of Non-Uniform Gases*. 3rd ed., Cambridge University Press, Cambridge.

Charles R. J. (1967) Activities in Li_2O-, Na_2O-, and K_2O-SiO_2 Solutions. *J. Am. Ceram. Soc.* **50**, 631–641.

Chase M. W. (1998) NIST-JANAF Thermochemical Tables, 4th Ed. *J. Phys. Chem. Ref. Data Monograph 9, Parts I & II*.

Churakov S. V, Tkachenko S. I., Korzhinskii M. A., Botcharnikov R. E. and Schmulovich K. I. (2000) Evolution of composition of high temperature fumarolic gasses from Kudryavy volcano,

Iturup, Kuril Islands: the thermodynamic modeling. *Geochemistry Int.* **38**, 436–451.
Costa G. C. C., Jacobson N. S. and Fegley B. (2017) Vaporization and thermodynamics of forsterite-rich olivine and some implications for silicate atmospheres of hot rocky exoplanets. *Icarus* **289**, 42–55.
De Maria G., Balducci G., Guido M. and Piacente V. (1971) Mass spectrometric investigation of the vaporization process of Apollo 12 lunar samples. *Proc. Second Lunar Sci. Conf.* **2**, 1367–1380.
Donaldson C. H. (1979) Composition changes in a basalt melt contained in a wire loop of $Pt_{80}Rh_{20}$: effects of temperature, time, and oxygen fugacity. *Mineral. Mag.* **43**, 115–119.
Drowart J., Chatillon C., Hastie J. and Bonnell D. (2005) High-temperature mass spectrometry: Instrumental techniques, ionization cross-sections, pressure measurements, and thermodynamic data (IUPAC Technical Report). *Pure Appl. Chem.* **77**, 683–737.
Drowart J. and Goldfinger P. (1967) Investigation of Inorganic Systems at High Temperature by Mass Spectrometry. *Angew. Chemie Int. Ed.* **6**, 581–648.
Ebel D. S. (2004) Condensation of Rocky Material in Astrophysical Environments. In *Meteorites and the Early Solar System II* (eds. D. S. Lauretta and H. Y. Mcsween). University of Arizona Press, Tucson. pp. 253–277.
Ebel D. S. and Grossman L. (2000) Condensation in dust-enriched systems. *Geochemica Cosmochem. Acta* **64**, 339–366.
Edmonds M., Mather T. A. and Liu E. J. (2018) A distinct metal fingerprint in arc volcanic emissions. *Nature Geo.* **11**, 790–794.
Ertel W., Dingwell D. B. and O'Neill H. S. C. (1997) Compositional dependence of the activity of nickel in silicate melts. *Geochim. Cosmochim. Acta* **61**, 4707–4721.
Exner O. (1973) The Enthalpy-Entropy Relationship. In *Progress in Physical Organic Chemistry, Volume 10* (eds. A. Streitwieser and R. W. Taft). John Wiley & Sons, Inc., Hoboken, NJ, USA. pp. 411–482.
Fedkin A. V. and Grossman L. (2013) Vapor saturation of sodium: Key to unlocking the origin of chondrules. *Geochim. Cosmochim. Acta* **112**, 226–250.
Fedkin A. V., Grossman L. and Ghiorso M. S. (2006) Vapor pressures and evaporation coefficients for melts of ferromagnesian chondrule-like compositions. *Geochim. Cosmochim. Acta* **70**, 206–223.
Fegley B., Jacobson N. S., Williams K. B., Plane J. M. C., Schaefer L. and Lodders K. (2016) Solubility of Rock in Steam Atmospheres of Planets. *Astrophys. J.* **824**, 103.
Fegley B. and Palme H. (1985) Evidence for oxidizing conditions in the solar nebula from Mo and W depletions in refractory inclusions in carbonaceous chondrites. *Earth Planet. Sci. Lett.* **72**, 311–326.
Fraser D. G. and Rammensee W. (1987) Determination of the mixing properties of granitic and other alumino silicate melts by Knudsen Cell Mass Spectrometry. In *Magmatic Processes: Physicochemical Principles* (ed. B. O. Mysen), The Geochemical Society Special Publication **1**, Washington D.C. pp. 401–410.
Genda H. and Abe Y. (2003) Modification of a proto-lunar disk by hydrodynamic escape of silicate vapor. *Earth Planets Sp.* **53**, 53–57.
Georges P., Libourel G. and Deloule E. (2000) Experimental constraints on alkali condensation in chondrule formation. *Meteorit. Planet. Sci.* **35**, 1183–1188.
Gibson E. K. and Hubbard N. J. (1972) Thermal volatilization studies on lunar samples. *Proc. Third Lunar Sci. Conf.* **2**, 2003–2014.
Glushko V. P., Medvedev V. A., Gurvich L. V. and Yungman V. S. (1999) *Thermal Constants of Substances*. 1st ed., John Wiley & Sons, New York.
Gooding J. L. and Muenow D. W. (1976) Activated release of alkalis during the vesiculation of molten basalts under high vacuum: implications for lunar volcanism. *Geochim. Cosmochim. Acta* **40**, 675–686.
Grant K. and Wood B. J. (2008) Alkali activities in silicate melts. *Geochim. Cosmochim. Acta*, A323.
Grossman L. (1972) Condensation in the primitive solar nebula. *Geochim. Cosmochim. Acta* **36**, 597–619.
Grossman L. and Larimer J. W. (1974) Early chemical history of the solar system. *Rev. Geophys.* **12**, 71–101.

945 Hastie J. W., Plante E. R., Bonnell and D. W. (1982) Alkali Vapor Transport in Coal Conversion and
946 Combustion Systems. In: *Metal Bonding and Interactions in High Temperature Systems* (eds. J.
947 L. Gole and W. C. Stwalley W. C.), ACS Symposium Series **179**, Washington D.C., pp. 543–
948 600.
949 Hertz H. (1882) Ueber den Druck des gesättigten Quecksilberdämpfes. *Ann. der Phys. und Chemie*
950 **17**, 177–197.
951 Hin R. C., Coath C. D., Carter P. J., Nimmo F., Lai Y.-J., Pogge von Strandmann P. A. E., Willbold
952 M., Leinhardt Z. M., Walter M. J. and Elliott T. (2017) Magnesium isotope evidence that
953 accretional vapour loss shapes planetary compositions. *Nature* **549**, 511–515.
954 Hirth J. P. and Pound G. M. (1963) *Condensation and evaporation—nucleation and growth kinetics*,
955 Pergamon Press, Oxford.
956 Holzheid A., Borisov A. and Palme H. (1994) The effect of oxygen fugacity and temperature on
957 solubilities of nickel, cobalt, and molybdenum in silicate melts. *Geochim. Cosmochim. Acta* **58**,
958 1975–1981.
959 Holzheid A. and Lodders K. (2001) Solubility of copper in silicate melts as function of oxygen and
960 sulfur fugacities, temperature, and silicate composition. *Geochim. Cosmochim. Acta* **65**, 1933–
961 1951.
962 Holzheid A., Palme H. and Chakraborty S. (1997) The activities of NiO, CoO and FeO in silicate
963 melts. *Chem. Geol.* **139**, 21–38.
964 Humayun M. and Cassen P. (2000) Processes Determining the Volatile Abundances of the Meteorites
965 and Terrestrial Planets. In *The Origin of the Earth and Moon* (eds. R. M. Canup and K. Righter).
966 University of Arizona Press, Tucson. pp. 3–23.
967 Humayun M. and Clayton R. N. (1995) Potassium isotope cosmochemistry: Genetic implications of
968 volatile element depletion. *Geochim. Cosmochim. Acta* **59**, 2131–2148.
969 Humayun M. and Koeberl C. (2004) Potassium isotopic composition of Australasian tektites.
970 *Meteorit. Planet. Sci.* **39**, 1509–1516.
971 Hunten D. M., Pepin R. O. and Walker J. C. G. (1987) Mass fractionation in hydrodynamic escape.
972 *Icarus* **69**, 532–549.
973 Janssens M.-J., Hertogen J., Wolf R., Ebihara M. and Anders E. (1987) Ureilites: Trace element clues
974 to their origin. *Geochim. Cosmochim. Acta* **51**, 2275–2283.
975 Jochum K.P., Stoll B., Weis U., Jacob D. E., Mertz-Kraus R. and Andreae M. O. (2014). Non-Matrix-
976 Matched Calibration for the Multi-Element Analysis of Geological and Environmental Samples
977 Using 200 nm Femtosecond LA-ICP-MS: A Comparison with Nanosecond Lasers. *Geochem.*
978 *Geoanal. Res.* **38**(3), 265–292.
979 Johnson A. and Canil D. (2011) The degassing behavior of Au, Tl, As, Pb, Re, Cd and Bi from
980 silicate liquids: Experiments and applications. *Geochim. Cosmochim. Acta* **75**, 1773–1784.
981 Kato C. and Moynier F. (2017) Gallium isotopic evidence for extensive volatile loss from the Moon
982 during its formation. *Sci. Adv.* **3**, e1700571.
983 Keays R. R., Ganapathy R. and Anders E. (1971) Chemical fractionations in meteorites-IV
984 Abundances of fourteen trace elements in L-chondrites; implications for cosmothermometry.
985 *Geochim. Cosmochim. Acta* **35**, 337–363.
986 Kemeny G. and Rosenberg B. (1973) Compensation law in thermodynamics and thermal death.
987 *Nature* **243**, 400–401.
988 Kimura H., Asano M. and Kubo K. (1980) Thermochemical study of the vaporization of Li_2O(c) by
989 mass spectrometric Knudsen effusion method. *J. Nucl. Mater.* **92**, 221–228.
990 Klemme S. and O'Neill H. S. C. (2000) The effect of Cr on the solubility of Al in orthopyroxene:
991 experiments and thermodynamic modelling. *Contrib. to Mineral. Petrol.* **140**, 84–98.
992 Knacke O. and Stranski I. N. (1956) The mechanism of evaporation. *Prog. Met. Phys.* **6**, 181–235.
993 Knudsen M. (1909) Die Gesetze der Molekularströmung und der inneren Reibungsströmung der Gase
994 durch Röhren. *Ann. Phys.* **333**, 75–130.
995 Kobertz D., Müller M. and Molak A. (2014) Vaporization and caloric studies on lead titanate.
996 *Calphad Comput. Coupling Phase Diagrams Thermochem.* **46**, 62–79.
997 Kobertz D. (2019a) Vaporization and caloric studies on yellow lead oxide. *Calphad* **65**, 155–164.
998 Kobertz D. (2019b) Vaporization studies on sodium oxide. *Calphad* **64**, 327–333.
999 Koeberl C. (1986) Geochemistry of tektites and impact glasses. *Annu. Rev. Earth Planet. Sci.* **14**,

323–350.
Kreutzberger M. E., Drake M. J. and Jones J. H. (1986) Origin of the Earth's Moon: Constraints from alkali volatile trace elements. *Geochim. Cosmochim. Acta* **50**, 91–98.
L'vov B. (2007) *Thermal Decomposition of Solids and Melts*. 1st ed. Springer Netherlands.
Lamoreaux R. H. and Hildenbrand D. L. (1984) High Temperature Vaporization of Oxides. I. Alkali Metal Binary Oxides. *J. Phys. Chem. Ref. Data* **13**, 151–173.
Lamoreaux R. H., Hildenbrand D. L. and Brewer L. (1987) High-Temperature Vaporization Behavior of Oxides II. Oxides of Be, Mg, Ca, Sr, Ba, B, Al, Ga, In, Tl, Si, Ge, Sn, Pb, Zn, Cd, and Hg. *J. Phys. Chem. Ref. Data* **16**, 419–443.
Langmuir I. (1916) The evaporation, condensation and reflection of molecules and the mechanism of adsorption. *Phys. Rev.* **8**, 149–176.
Larimer J. W. (1967) Chemical fractionations in meteorites-I. Condensation of the elements. *Geochim. Cosmochim. Acta* **31**, 1215–1238.
Larimer J. W. (1973) Chemical fractionations in meteorites-VII. Cosmothermometry and cosmobarometry. *Geochim. Cosmochim. Acta* **37**, 1603–1623.
Laul J. C., Ganapathy R., Anders E. and Morgan J. W. (1973) Chemical fractionations in meteorites-VI. Accretion temperatures of H-, LL- and E-chondrites, from abundance of volatile trace elements. *Geochim. Cosmochim. Acta* **37**, 329–357.
Li Z., Hu Z., Liu Y., Gao S., Li M., Zong K., Chen H. and Hu S. (2015) Accurate determination of elements in silicate glass by nanosecond and femtosecond laser ablation ICP-MS at high spatial resolution. *Chem. Geol.* **400**, 11–23.
Littlewood R. and Rideal E. (1956) On the Evaporation Coefficient. *Trans. Faraday Soc.* **52**, 1598–1608.
Liu Y., Zhang L. and Yu D. (2009) Diffusion mobilities in fcc Cu-Au and fcc Cu-Pt alloys. *J. Phase Equilibria Diffus.* **30**, 136–145.
Lodders K. (2003) Solar System Abundances and Condensation Temperatures of the Elements. *Astrophys. J.* **591**, 1220–1247.
Magna T., Wiechert U. and Halliday A. N. (2006) New constraints on the lithium isotope compositions of the Moon and terrestrial planets. *Earth Planet. Sci. Lett.* **243**, 336–353.
Mann U., Frost D. J. and Rubie D. C. (2009) Evidence for high-pressure core-mantle differentiation from the metal–silicate partitioning of lithophile and weakly-siderophile elements. *Geochim. Cosmochim. Acta* **73**, 7360–7386.
Mare E., O'Neill H. S. C. and Berry A. (2016) Changes in the Coordination and Valence State of Ge in Silicate Melts at Conditions Relevant to Core Formation. In *Mineralogical Magazine* Yokohama, Japan. p. 1971.
Margrave J. L. (1967) *The Characterization of High Temperature Vapors*, John Wiley & Sons, New York.
Markova O. M., Yakovlev O. I., Semenov G. A. and Belov A. N. (1986) Evaporation of Natural Melts in a Knudsen Chamber. *Geokhimiya* **11**, 1559–1568.
Mather T. A., Witt M. L. I., Pyle D. M., Quayle B. M., Aiuppa A., Bagnato E., Martin R. S., Sims K. W. W., Edmonds M., Sutton A. J. and Ilyinskaya E. (2012) Halogens and trace metal emissions from the ongoing 2008 summit eruption of Kīlauea volcano, Hawai'i. *Geochim. Cosmochim. Acta* **83**, 292–323.
Mathieu R., Khedim H., Libourel G., Podor R., Tissandier L., Deloule E., Faure F., Rapin C. and Vilasi M. (2008) Control of alkali-metal oxide activity in molten silicates. *J. Non. Cryst. Solids* **354**, 5079–5083.
Mathieu R., Libourel G., Deloule E., Tissandier L., Rapin C. and Podor R. (2011) Na_2O solubility in CaO-MgO-SiO_2 melts. *Geochim. Cosmochim. Acta* **75**, 608–628.
Maxwell J. C. (1860) Illustrations of the dynamical theory of gases.—Part I. On the motions and collisions of perfectly elastic spheres. *London, Edinburgh, Dublin Philos. Mag. J. Sci.* **19**, 19–32.
Melosh H. J. (1990) Giant Impacts and the Thermal State of the Early Earth. In *Origin of the Earth* (eds. H. E. Newsom and J. H. Jones). Oxford University Press, New York. pp. 69–83.
Morbidelli A., Lunine J. I., O'Brien D. P., Raymond S. N. and Walsh K. J. (2012) Building Terrestrial Planets. *Annu. Rev. Earth Planet. Sci.* **40**, 251–275.

Moynier F., Beck P., Jourdan F., Yin Q. Z., Reimold U. and Koeberl C. (2009) Isotopic fractionation of zinc in tektites. *Earth Planet. Sci. Lett.* **277**, 482–489.
Nakajima M. and Stevenson D. J. (2014) Investigation of the initial state of the Moon-forming disk: Bridging SPH simulations and hydrostatic models. *Icarus* **233**, 259–267.
Naughton J. J., Derby J. V. and Lewis V. A. (1971) Vaporization from heated lunar samples and the investigation of lunar erosion by volatilized alkalis. *Proc. Second Lunar Sci. Conf.* **1**, 449–457.
Ni P., Zhang Y., Chen S. and Gagnon J. (2019) A melt inclusion study on volatile abundances in the lunar mantle. *Geochim. Cosmochim. Acta* **249**, 17–41.
Norman M. D., Garcia M. O. and Bennett V. C. (2004) Rhenium and chalcophile elements in basaltic glasses from Ko'olau and Moloka'i volcanoes: Magmatic outgassing and composition of the Hawaiian plume. *Geochim. Cosmochim. Acta* **68**, 3761–3777.
Norris C. A. and Wood B. J. (2017) Earth's volatile contents established by melting and vaporization. *Nature* **549**, 507–510.
Notsu K., Onuma N. and Nishida N. (1978) High temperature heating of the Allende meteorite. *Geochim. Cosmochim. Acta* **42**, 903–907.
O'Neill H. S. C. (2005) A method for controlling alkali-metal oxide activities in one-atmosphere experiments and its application to measuring the relative activity coefficients of $NaO_{0.5}$ in silicate melts. *Am. Mineral.* **90**, 497–501.
O'Neill H. S. C. (1991) The origin of the Moon and the early history of the Earth - A chemical model. Part 1: The Moon. *Geochim. Cosmochim. Acta* **55**, 1135–1157.
O'Neill H. S. C. and Eggins S. M. (2002) The effect of melt composition on trace element partitioning: an experimental investigation of the activity coefficients of FeO, NiO, CoO, MoO_2 and MoO_3 in silicate melts. *Chem. Geol.* **186**, 151–181.
O'Neill H. S. C. and Palme H. (2008) Collisional erosion and the non-chondritic composition of the terrestrial planets. *Philos. Trans. A. Math. Phys. Eng. Sci.* **366**, 4205–38.
O'Neill H. S. C. and Palme H. (1998) Composition of the Silicate Earth: Implications for Accretion and Core Formation. In *The Earth's Mantle: Composition, Structure and Evolution* (ed. I. Jackson). Cambridge University Press, Cambridge. pp. 3 – 126.
O'Neill H. S. C. and Pownceby M. I. (1993) Thermodynamic data from redox reactions at high temperatures. I. An experimental and theoretical assessment of the electrochemical method using stabilized zirconia electrolytes, with revised values for the Fe–"FeO", Co–CoO, Ni–NiO and Cu–Cu_2O. *Contrib. to Mineral. Petrol.* **114**, 296–314.
Ohta H. and Suito H. (1995) Activities of MnO in CaO-SiO_2-Al_2O_3-MnO (<10 Pct)-Fe^tO (<3 Pct) Slags Saturated with Liquid Iron. *Metall. Mater. Trans. B* **26**, 295–303.
Oulton J., Humayun M., Fedkin A. and Grossman L. (2016) Chemical evidence for differentiation , evaporation and recondensation from silicate clasts in Gujba. *Geochim. Cosmochim. Acta* **177**, 254–274.
Pahlevan K., Stevenson D. J. and Eiler J. M. (2011) Chemical fractionation in the silicate vapor atmosphere of the Earth. *Earth Planet. Sci. Lett.* **301**, 433–443.
Palme H., Larimer J. W. and Lipschutz M. E. (1988) Moderately Volatile Elements. In *Meteorites and the Early Solar System* (eds. J. F. Kerridge and M. S. Matthews). University of Arizona Press, Tucson. pp. 436–461.
Paniello R. C., Day J. M. D. and Moynier F. (2012) Zinc isotopic evidence for the origin of the Moon. *Nature* **490**, 376–379.
Persad A. H. and Ward C. A. (2016) Expressions for the Evaporation and Condensation Coefficients in the Hertz-Knudsen Relation. *Chem. Rev.* **116**, 7727–7767.
Pretorius E. B. and Muan (1992) Activity–Composition Relations of Chromium Oxide in Silicate Melts at 1500 °C. *J. Am. Ceram. Soc.* **75**, 1364–1377.
Pringle E. A., Moynier F., Beck P., Paniello R. and Hezel D. C. (2017) The origin of volatile element depletion in early solar system material: Clues from Zn isotopes in chondrules. *Earth Planet. Sci. Lett.* **468**, 62–71.
Rammensee W. and Fraser D. G. (1982) Determination of activities in silicate melts by Knudsen cell mass spectrometry-I. The system $NaAlSi_3O_8$-$KAlSi_3O_8$. *Geochim. Cosmochim. Acta* **46**, 2269–2278.
Renggli C. J., King P. L., Henley R. W. and Norman M. D. (2017) Volcanic gas composition, metal

dispersion and deposition during explosive volcanic eruptions on the Moon. *Geochim. Cosmochim. Acta* **206**, 296–311.
Reyes R. A. and Gaskell D. R. (1983) The thermodynamic activity of ZnO in silicate melts. *Metall. Trans. B* **14**, 725–731.
Richter F. M., Davis A. M., Ebel D. S. and Hashimoto A. (2002) Elemental and isotopic fractionation of type B calcium-, aluminum-rich inclusions: Experiments, theoretical considerations, and constraints on their thermal evolution. *Geochim. Cosmochim. Acta* **66**, 521–540.
Richter F. M., Janney P. E., Mendybaev R. A., Davis A. M. and Wadhwa M. (2007) Elemental and isotopic fractionation of Type B CAI-like liquids by evaporation. *Geochim. Cosmochim. Acta* **71**, 5544–5564.
Ringwood A. E. (1966) Chemical evolution of the terrestrial planets. *Geochim. Cosmochim. Acta* **30**, 41–104.
Robie R. A. and Hemingway B. S. (1995) *Thermodynamic Properties of Minerals and Related Substances at 298.15 K and 1 Bar (10^5 Pascals) Pressure and at Higher Temperatures*. USGS Bulletin 2131.
Rubin A. E., Fegley B. and Brett R. (1988) Oxidation State in Chondrites. In *Meteorites and the Early Solar System* (eds. J. F. Kerridge and M. S. Matthews). University of Arizona Press, Tucson. pp. 488–511.
Ruzicka A., Snyder G. A. and Taylor L. A. (2001) Comparative geochemistry of basalts from the Moon, Earth, HED asteroid, and Mars: Implications for the origin of the Moon. *Geochim. Cosmochim. Acta* **65**, 979–997.
Safarian J. and Engh T. A. (2013) Vacuum Evaporation of Pure Metals. *Metall. Mater. Trans. A* **44**, 747–753.
Sahijpal S., Soni P. and Gupta G. (2007) Numerical simulations of the differentiation of accreting planetesimals with ^{26}Al and ^{60}Fe as the heat sources. *Meteorit. Planet. Sci.* **42**, 1529–1548.
Schaefer L. and Fegley B. (2010) Volatile element chemistry during metamorphism of ordinary chondritic material and some of its implications for the composition of asteroids. *Icarus* **205**, 483–496.
Schaefer L., Lodders K. and Fegley B. (2012) Vaporization of the earth: Application to exoplanet atmospheres. *Astrophys. J.* **755**, 41.
Schreiber H. D. (1987) An Electrochemical Series of Redox Couples in Silicate Melts: A Review and Applications to Geochemistry. *J. Geophys. Res.* **92**, 9225–9232.
Shimaoka T., Miyano N., Baba T., Yamamoto K. and Nakamura N. (1994) Volatilization of Alkali Metals from the Heated Murchison (CM2) Meteorite. *Proc. NIPR Symp. Antarct. Meteorites* **7**, 164–177.
Shimaoka T. and Nakamura (1991) The effect of total pressure on vaporization of alkalis from partially molten chondritic material. In *Origin and Evolution of Interplanetary Dust* (eds. A. C. Levasseur-Regourd and H. Hasegawa). Kluwer Academic Publishers, Japan. pp. 79–82.
Shornikov S. I. (2015) Vaporization coefficients of oxides contained in the melts of Ca-Al-inclusions in chondrites. *Geochemistry Int.* **53**, 1080–1089.
Siebert J., Corgne A. and Ryerson F. J. (2011) Systematics of metal–silicate partitioning for many siderophile elements applied to Earth's core formation. *Geochim. Cosmochim. Acta* **75**, 1451–1489.
Siebert J. and Shahar A. (2015) An Experimental Geochemistry Perspective on Earth's Core Formation. In *The Early Earth: Accretion and Differentiation* (eds. J. Badro and M. J. Walter). American Geophysical Union, Washington, D. C. pp. 103–121.
Siebert J., Sossi P. A., Blanchard I., Mahan B., Badro J. and Moynier F. (2018) Chondritic Mn/Na ratio and limited post-nebular volatile loss of the Earth. *Earth Planet. Sci. Lett.* **485**, 130–139.
Sossi P. A. and Fegley B. (2018) Thermodynamics of Element Volatility and its Application to Planetary Processes. In *Reviews in Mineralogy and Geochemistry 84: High temperature gas-solid reactions in Earth and planetary processes* (eds. P. L. King, T. M. Seward, and B. Fegley). Mineralogical Society of America, Chantilly. pp. 393–459.
Sossi P. A., Nebel O., O'Neill H. S. C. and Moynier F. (2018) Zinc isotope composition of the Earth and its behaviour during planetary accretion. *Chem. Geol.* **477**, 73–84.
Symonds R. B. and Reed M. H. (1993) Calculation of Multicomponent chemical equilibria in gas-

solid-liquid systems: Calculation methods, thermochemical data, and applications to studies of high-temperature volcanic gases with examples from Mount St. Helens. *Am. J. Sci.* **293**, 758–864.

Toker N. Y., Darken L. S. and Muan A. (1991) Equilibrium Phase Relations and Thermodynamics of the Cr-O System in the Temperature Range of 1500 °C to 1825 °C. *Metall. Trans. B* **22B**, 225–232.

Tsuchiyama A., Nagahara H. and Kushiro I. (1981) Volatilization of sodium from silicate melt spheres and its application to the formation of chondrules. *Geochim. Cosmochim. Acta* **45**, 1357–1367.

Tuff J. and O'Neill H. S. C. (2010) The effect of sulfur on the partitioning of Ni and other first-row transition elements between olivine and silicate melt. *Geochim. Cosmochim. Acta* **74**, 6180–6205.

Urey H. C. (1952) Chemical fractionation in the meteorites and the abundance of the elements. *Geochim. Cosmochim. Acta* **2**, 269–282.

Urey H. C. (1954) On the dissipation of gas and volatilized elements from protoplanets. *Astrophys. J. Suppl. Ser.* **1**, 147–173.

Visscher C. and Fegley B. (2013) Chemistry of Impact-Generated Silicate Melt-Vapor Debris Disks. *Astrophys. J.* **767**, L12.

Vlastélic I., Menard G., Gannoun A., Piro J. L., Staudacher T. and Famin V. (2013) Magma degassing during the April 2007 collapse of Piton de la Fournaise: The record of semi-volatile trace elements (Li, B, Cu, In, Sn, Cd, Re, Tl, Bi). *J. Volcanol. Geotherm. Res.* **254**, 97–107.

Wang K. and Jacobsen S. B. (2016) Potassium Isotopic Evidence for the Origin of the Moon. *Nature* **538**, 487–490.

Wang Z., Laurenz V., Petitgirard S. and Becker H. (2016) Earth's moderately volatile element composition may not be chondritic: Evidence from In, Cd and Zn. *Earth Planet. Sci. Lett.* **435**, 136–146.

Wänke H. and Dreibus G. (1988) Chemical Composition and Accretion History of Terrestrial Planets. *Philos. Trans. R. Soc. A Math. Phys. Eng. Sci.* **325**, 545–557.

Watson E. B., Cherniak D. J., Hanchar J. M., Harrison T. M. and Wark D. A. (1997) The incorporation of Pb into zircon. *Chem. Geol.* **141**, 19–31.

Witt-Eickschen G., Palme H., O'Neill H. S. C. and Allen C. M. (2009) The geochemistry of the volatile trace elements As, Cd, Ga, In and Sn in the Earth's mantle: New evidence from in situ analyses of mantle xenoliths. *Geochim. Cosmochim. Acta* **73**, 1755–1778.

Wolf R., Richter G. R., Woodrow A. B. and Anders E. (1980) Chemical fractionations in meteorites—XI. C2 chondrites. *Geochim. Cosmochim. Acta* **44**, 711–717.

Wolf R. and Anders E. (1980) Moon and Earth: compositional differences inferred from siderophiles, volatiles, and alkalis in basalts. *Geochim. Cosmochim. Acta* **44**, 2111–2124.

Wombacher F., Rehkämper M. and Mezger K. (2004) Determination of the mass-dependence of cadmium isotope fractionation during evaporation. *Geochim. Cosmochim. Acta* **68**, 2349–2357.

Wombacher F., Rehkämper M., Mezger K., Bischoff A. and Münker C. (2008) Cadmium stable isotope cosmochemistry. *Geochim. Cosmochim. Acta* **72**, 646–667.

Wood B. J. and Halliday A. N. (2010) The lead isotopic age of the Earth can be explained by core formation alone. *Nature* **465**, 767–70.

Wood B. J., Kiseeva E. S. and Mirolo F. J. (2014) Accretion and core formation: the effects of sulfur on metal-silicate partition coefficients. *Geochim. Cosmochim. Acta* **145**, 248–267.

Wood B. J., Smythe D. J. and Harrison T. (2019) The condensation temperatures of the elements: a reappraisal. *Am. Min.* **104**(6), 844–856.

Wood B. J. and Wade J. (2013) Activities and volatilities of trace components in silicate melts: a novel use of metal–silicate partitioning data. *Contrib. to Mineral. Petrol.* **166**, 911–921.

Wood B. J., Walter M. J. and Wade J. (2006) Accretion of the Earth and segregation of its core. *Nature* **441**, 825–33.

Wulf A. V, Palme H. and Jochum K. P. (1995) Fractionation of volatile elements in the early solar system: evidence from heating experiments on primitive meteorites. *Planet. Space Sci.* **43**, 451–468.

Yamauchi M. and Wahlund J.-E. (2007) Role of the ionosphere for the atmospheric evolution of

planets. *Astrobiology* **7**, 783–800.
Young E. D., Shahar A., Nimmo F., Schlichting H. E., Schauble E. A., Tang H. and Labidi J. (2019). Near-equilibrium isotope fractionation during planetesimal evaporation. *Icarus*, **323**, 1–15.
Yu Y., Hewins R. H., Alexander C. M. O. 'D. and Wang J. (2003) Experimental study of evaporation and isotopic mass fractionation of potassium in silicate melts. *Geochim. Cosmochim. Acta* **67**, 773–786.

Figure captions

Fig. 1. Back-scattered electron images of four experimental glasses at the same magnification (1000 μm scale bar shown), a) 3M-29/02/16, 1400 °C, logfO_2 = -0.68, 60 minutes; b) 1M-1/3/16, 1400 °C, logfO_2 = -10.01, 60 minutes; c) 2M-16/07/16h, 1550 °C, logfO_2 = -6.01, 15 minutes; d) P-11/06/18b, 1550 °C, logfO_2 = -5.48, 15 minutes.

Fig. 2. Concentrations of volatile elements (K, Cr, Cu, Zn, Ga, Ge, Rb, Mo, Ag, Cd, Pb; N = 38) in an experimental glass (pair 1) plotted relative to their concentrations in another experimental glass run under the same conditions (pair 2) for four experimental pairs. The different shades correspond to the following experimental pairs (pair 1, pair 2): black (P-09/06/18b, P-09/06/18a), 1400 °C, logfO_2 = -9.23, 15 minutes; dark grey (P-08/02/17b, 3M-29/2/16), 1400 °C, logfO_2 = -0.68, 60 minutes; light grey (P-09/06/18c, 1M-PS1), 1400 °C, logfO_2 = -5.50, 60 minutes; white (1M-2/3/16, C18/12/15), 1400 °C, logfO_2 = -3.07, 60 minutes.

Fig. 3. Measurement of elemental zoning profiles in sample 3M-29/02/16 (1400 °C, 60 mins, air). Panel a) shows a reflected light image of the glass and laser spot profiles. Panel b) displays the fraction of a volatile element *i* remaining in the glass (Ga, green; Zn, red; Cu, blue; Ge, purple; Rb, blue; Mo, orange) as a function of distance from rim to rim, corresponding to the uppermost profile in panel a), with 25 μm spots at 100 μm spacing.

Fig. 4. Vaporisation of a) Na, b) K, c) Rb, and d) Cu – elements with one oxidation state in the liquid and one species in the gas, corresponding to vaporisation reactions with n = 1 stoichiometry (eq. 4). The fraction of the element remaining in the glass after a run duration of 60 minutes (Na and K) or 15 minutes (Rb and Cu), relative to its initial concentration in the glass $\left(\frac{X_i^t}{X_i^0}\right)$ are plotted as a function of logfO_2. Lines at the top denote the location of the FMQ buffer as a function of temperature. Curves are non-linear least-squares fits (see eq. 9) to the experimental data using eq. (8), shown along with the log$K$* values to which they correspond. Colours of lines, curves and symbols denote the temperature of the experiment; blue = 1300 °C, green = 1400 °C, yellow = 1500 °C, red = 1550 °C.

Fig. 5. Vaporisation of a) Zn and b) Ge – elements with one oxidation state in the liquid and one gas species, corresponding to vaporisation reactions with n = 2 stoichiometry (eq. 4). The fraction of the element remaining in the glass after a run duration of 15 minutes, relative to its initial concentration in the glass $\left(\frac{X_i^t}{X_i^0}\right)$ is plotted as a function of logfO_2. Lines at the top denote the location of the FMQ buffer. Colours and nomenclature are as per Fig. 4.

Fig. 6. Vaporisation of a) Li, b) Ga and c) Pb – elements with one oxidation state in the liquid and multiple species in the gas. The fraction of the element remaining in the glass after an experimental run, relative to its initial concentration in the glass $\left(\frac{X_i^t}{X_i^0}\right)$ is plotted as a function of a) time for Li. Shown are experiments performed at a single temperature, 1400 °C, at two logfO_2s, -0.68 (white circles) and -8.00 (black circles). Both series are fit by non-linear least squares using eq. 8 corresponding to the reactions $LiO_{0.5}(l) + ¼O_2 = LiO(g)$ for a log$K$* of -3.39 (white circles) and $LiO_{0.5}(l) = Li(g) + ¼O_2$ with log$K$* of -5.36 (black circles). Parts b) and c) plot $\left(\frac{X_i^t}{X_i^0}\right)$ against logfO_2 for Ga and Pb, respectively. Lines at the top denote the location of the FMQ buffer. Symbols and nomenclature as per Fig. 4. All experiments shown were run for 15

minutes. The two log$K$*s for Ga correspond to the reactions $GaO_{1.5}$(l) = GaO(g) + ¼O_2 (normal script) and $GaO_{1.5}$(l) = Ga(g) + ¾O_2 (italic); and for Pb, PbO(l) = PbO(g) (normal script) and PbO(l) = Pb(g) + ½O_2 (italic).

Fig. 7. Vaporisation of the Group VI elements – a) Mo and b) Cr – that have multiple species in the liquid and at least one species in the gas, whose net vaporisation reactions have $n < 0$ stoichiometry (see eq. 4). The fraction of the element remaining in the glass after a run duration of 15 minutes, relative to its initial concentration in the glass $\left(\frac{X_i^t}{X_i^0}\right)$ is plotted as a function of log$f$$O_2$. Lines at the top denote the location of the FMQ buffer. Colours and nomenclature are as per Fig. 4. For Mo, the log$K$* values shown correspond to the reaction: MoO_3(l) = MoO_3(g), and for Cr the log$K$* values shown correspond to the reaction: CrO(l) + ½O_2 = CrO_2(g).

Fig. 8. Activity coefficients (γ) of melt oxide species (i) at infinite dilution (∞) in a ferrobasaltic FCMAS liquid calculated by eq. 6, as a function of temperature. Melt oxide species are: $CuO_{0.5}$ = teal, $LiO_{0.5}$ = yellow, $AgO_{0.5}$ = grey, ZnO = blue, PbO = light orange, CdO = red, GeO_2 = purple, $NaO_{0.5}$ = sky blue, $KO_{0.5}$ = dark orange, $RbO_{0.5}$ = black. The two light orange 'PbO' series denote γ_{PbO}^{∞} calculated by two reactions, PbO(l) = PbO(g) (lower series) and PbO(l) = Pb(g) + ½O_2 (upper series). The two data points shown for $LiO_{0.5}$ denote $\gamma_{LiO_{0.5}}^{\infty}$ calculated at log$f$$O_2$ -8.00 by the reaction $LiO_{0.5}$(l) = Li(g) + ¼O_2 and at log$f$$O_2$ = -0.68 by the reaction $LiO_{0.5}$(l) + ¼ O_2 = LiO(g).

Fig. 9. The Gibbs Free Energy, ΔG*, in kJ/mol against temperature (K) for element vaporisation reactions from a ferrobasaltic liquid in the FCMAS system at 1 bar of a) Rb, $RbO_{0.5}$(l) = Rb(g) + ¼O_2 b) Cu, $CuO_{0.5}$(l) = Cu(g) + ¼O_2 c) Zn, ZnO(l) = Zn(g) + ½O_2 d) Ge, GeO_2(l) = GeO(g) + ½O_2. Greyscale denotes $f$$O_2$ series run at constant temperature with different times, White = 15 minutes, Black = 60 minutes, Grey = 120 minute. Best fits to all data points *via* the 2nd-law method yield the ΔG* as a function of temperature (shown in panel).

Fig. 10. Enthalpy (ΔH)-Entropy (ΔS) correlations for vaporisation reactions that are a) experimentally-derived (see section 4.7. and Table 5) and b) in the pure system (see Table 5). Labels refer to the stable gas species. Colours as per Fig. 8 with the addition of Ga and GaO (fuchsia), CrO_2 (green) for the reaction CrO(l) + ½O_2 = CrO_2(g) and MoO_3 (magenta) for the reaction MoO_2(l) + ½O_2 = MoO_3(g).

Fig. 11. Experimental data from the literature. a) Fraction of Na remaining in chondrule-like glass as a function of time at different temperatures (Tsuchiyama et al., 1981). Circles refer to 'composition 1'; blue = 1450 °C, green = 1500 °C, yellow = 1550 °C, red = 1600 °C; the square symbols refer to 'composition 2' at 1586 °C. Curves are fits with eq. 8 assuming an n = 1 evaporation stoichiometry, and numbers correspond to log$K$* values. b) Data of Kreutzberger et al. (1986) showing the fraction of Na (blue), K (orange) and Rb (black) remaining in a $Di_{75}An_{25}$ glass composition at 1400 °C in air as a function of time. Curves are fits with eq. 8 assuming an n = 1 evaporation stoichiometry, and numbers correspond to log$K$* values. c) Data of Norris and Wood (2017) showing the fraction of Cu (teal), Zn (blue), Ga (crimson), Ge (purple) and Pb (orange) remaining in MORB glass after 60 minutes at 1300 °C, as a function of log $f$$O_2$. The fits to the data are made relative to Zn, with eq. (19).

Fig. 12. Nebular half condensation temperatures (T_c^{50}) of a) Lodders (2003) and b) Wood et al. (2019) compared to 1% evaporation temperatures for metal oxides from a ferrobasaltic silicate melt at 1 bar and log $f$$O_2$ = -10, calculated from the experiments, except for Mn, Mg, Fe, Co, Ni and Cr, which are taken from thermodynamic data in the pure system (Table 5). Chalcophile = orange, Siderophile = grey, Lithophile = green. Line of best fit (black) to lithophile elements only.

Fig. 13. 1% evaporation temperatures for metal oxides from a ferrobasalt in the FCMAS system at 1 bar as a function of log $f$$O_2$, calculated from thermodynamic data from the experiments, except for Mn, Mg, Fe, Co, Ni and Cr (below IW-1), which are taken from the pure system (Table 5). Dotted coloured lines (Li, Na, K, Mo, Cr) indicate that evaporation temperatures are calculated assuming their activity coefficients are constant with temperature (For Li, Na, K calculated at 1673 K, for Mo

and Cr fixed by literature values at 1673 K) and hence uncertain outside of this temperature. In general, caution should be exercised in use of evaporation temperatures calculated outside of the experimental range (grey field). Dashed grey lines show the fO_2 defined by mineral oxygen buffers (IW = Iron-Wüstite, FMQ = Fayalite-Magnetite-Quartz, MH = Magnetite-Hematite).

Fig. 14. Elemental depletion factors normalised to Mg in a residual ferrobasalt melt after Langmuir evaporation at 1 bar calculated with eq. 19. Elements are plotted in order of their volatilities from the ferrobasalt composition. a) At constant relative fO_2 (FMQ buffer) and variable temperature (listed next to lines in K) and b) At constant temperature and variable relative fO_2 (ΔFMQ listed next to lines). Also plotted are the estimated elemental abundances of lithophile and weakly siderophile elements in the Earth's primitive mantle (Palme and O'Neill, 2014; green circles) and the Moon's primitive mantle (O'Neill, 1991, Ni et al. 2019; grey circles).

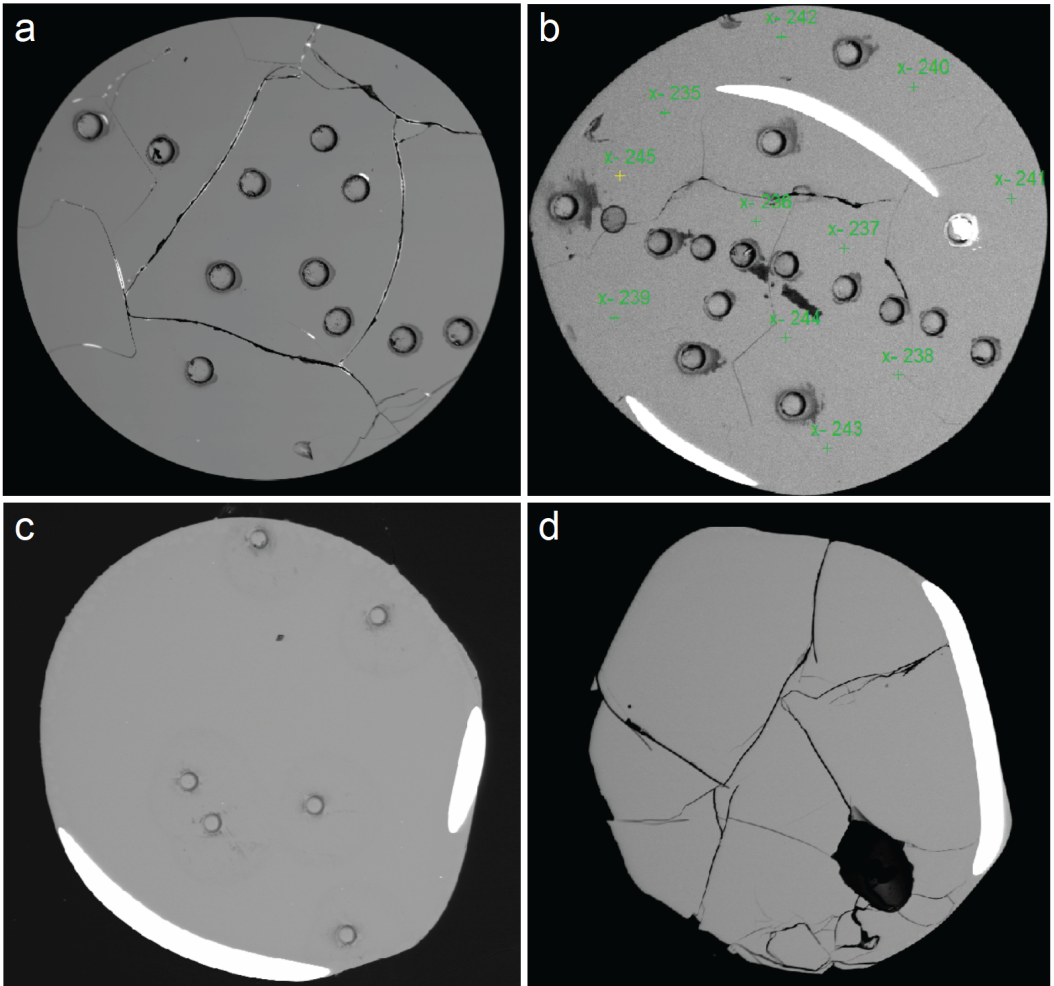
a
b
x- 242
x- 240
x- 235
x- 245
x- 241
x- 236
x- 237
x- 239
x- 244
x- 238
x- 243
c
d
1000 µm

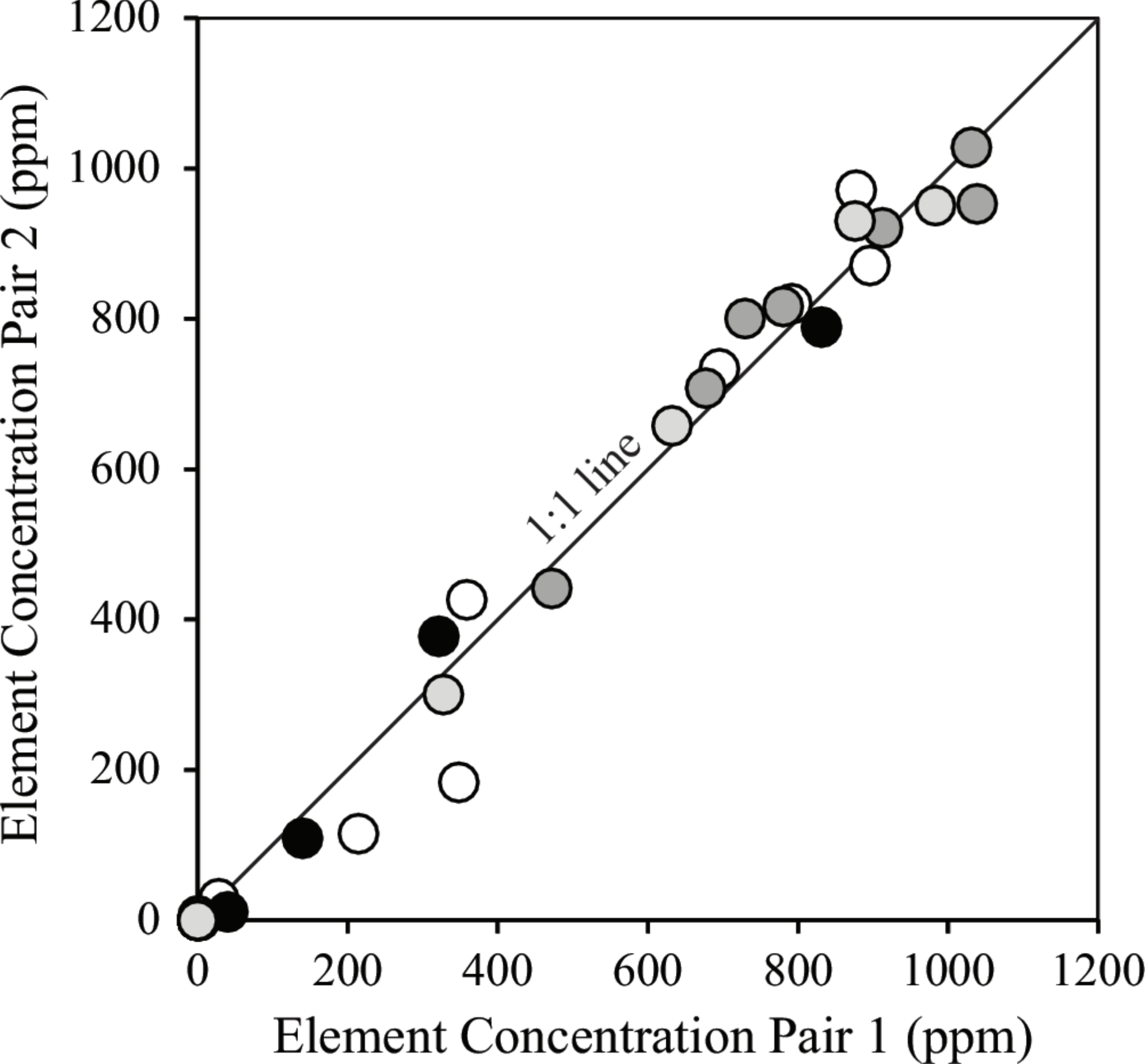
1200
1000
800
600
400
200
0
Element Concentration Pair 2 (ppm)
1:1 line
0
200
400
600
800
1000
1200
Element Concentration Pair 1 (ppm)

Sample 3M-29/02/16 (1400 °C, 60 mins, air)

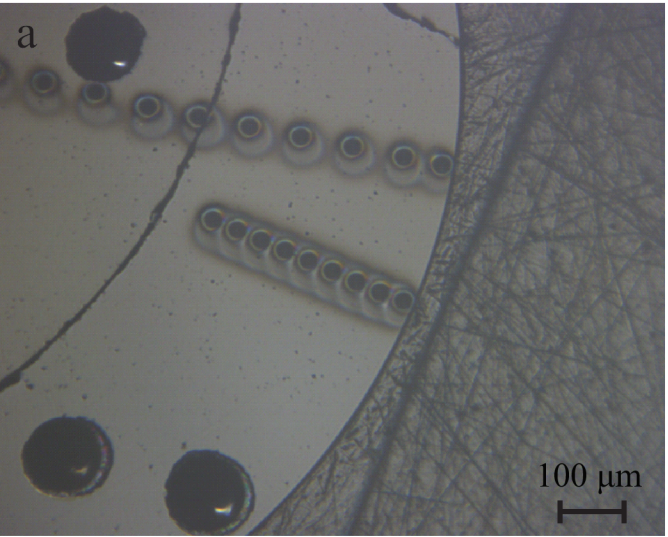

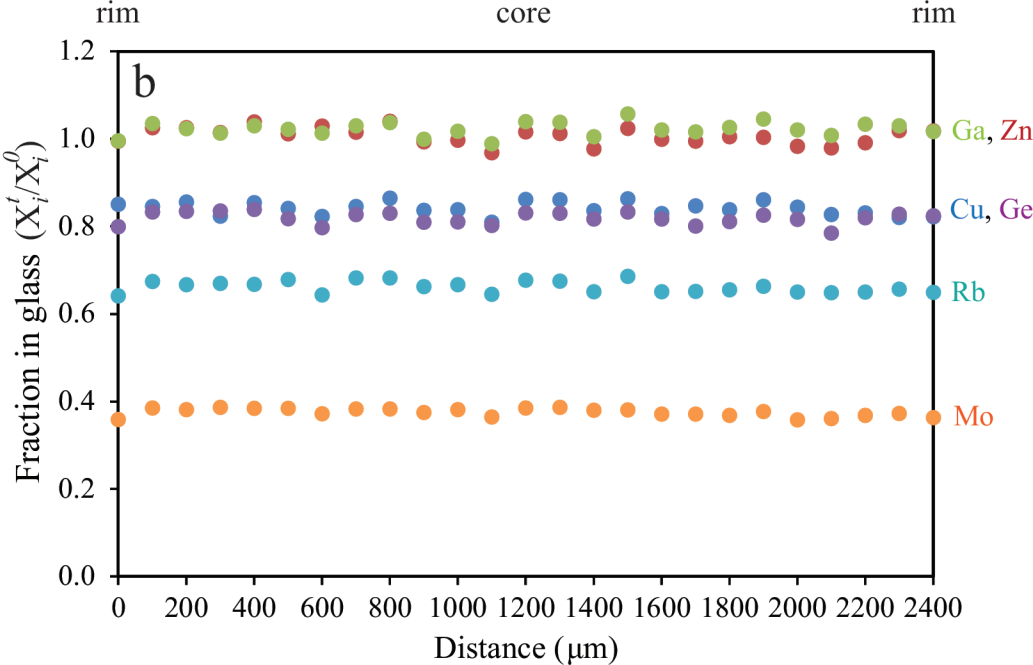

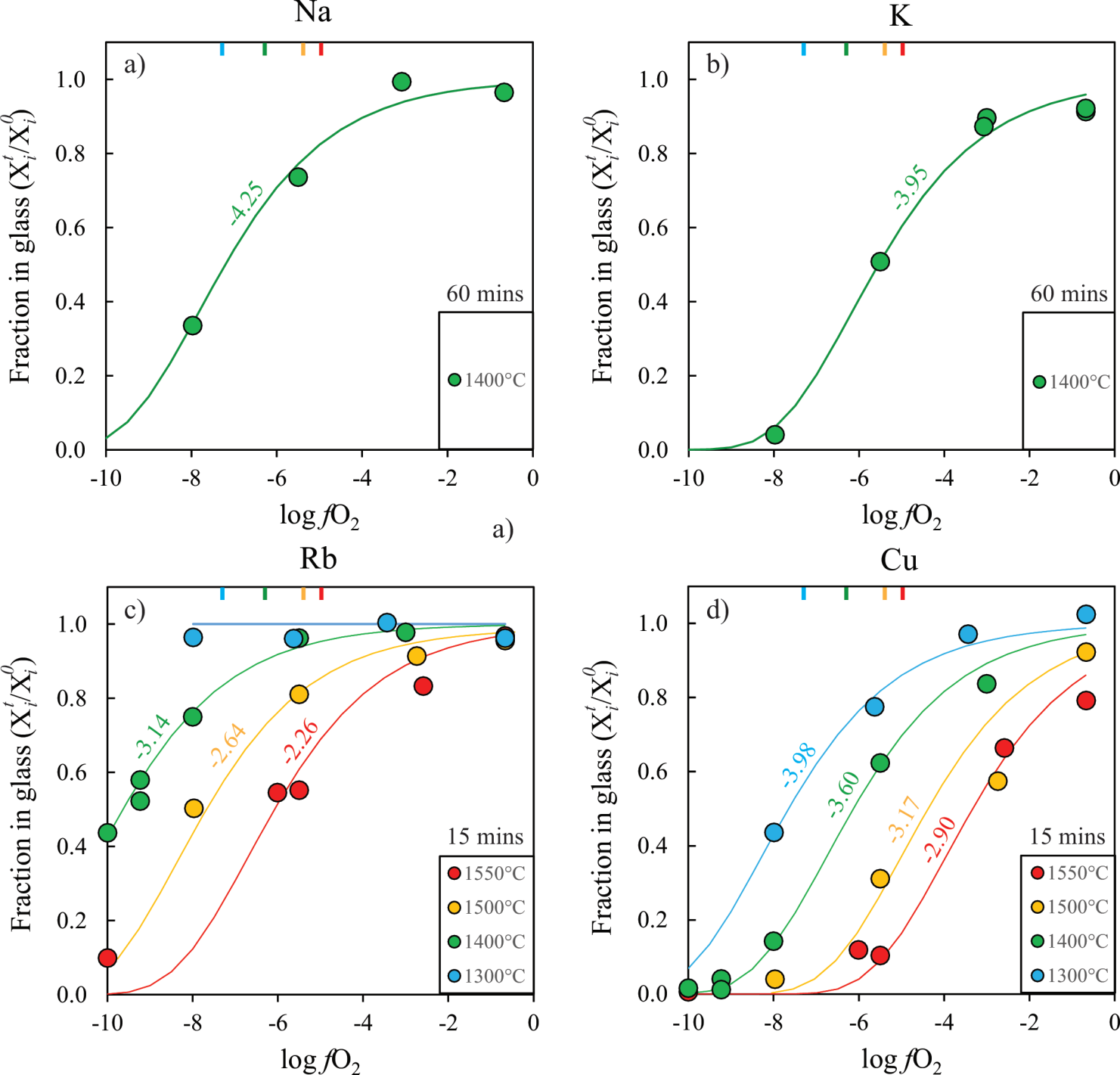
Na
a)
-4.25
60 mins
1400°C
Fraction in glass (X_i^t/X_i^0)
log fO_2
K
b)
-3.95
60 mins
1400°C
Fraction in glass (X_i^t/X_i^0)
log fO_2
a)
Rb
c)
-3.14
-2.64
-2.26
15 mins
1550°C
1500°C
1400°C
1300°C
Fraction in glass (X_i^t/X_i^0)
log fO_2
Cu
d)
-3.98
-3.60
-3.17
-2.90
15 mins
1550°C
1500°C
1400°C
1300°C
Fraction in glass (X_i^t/X_i^0)
log fO_2

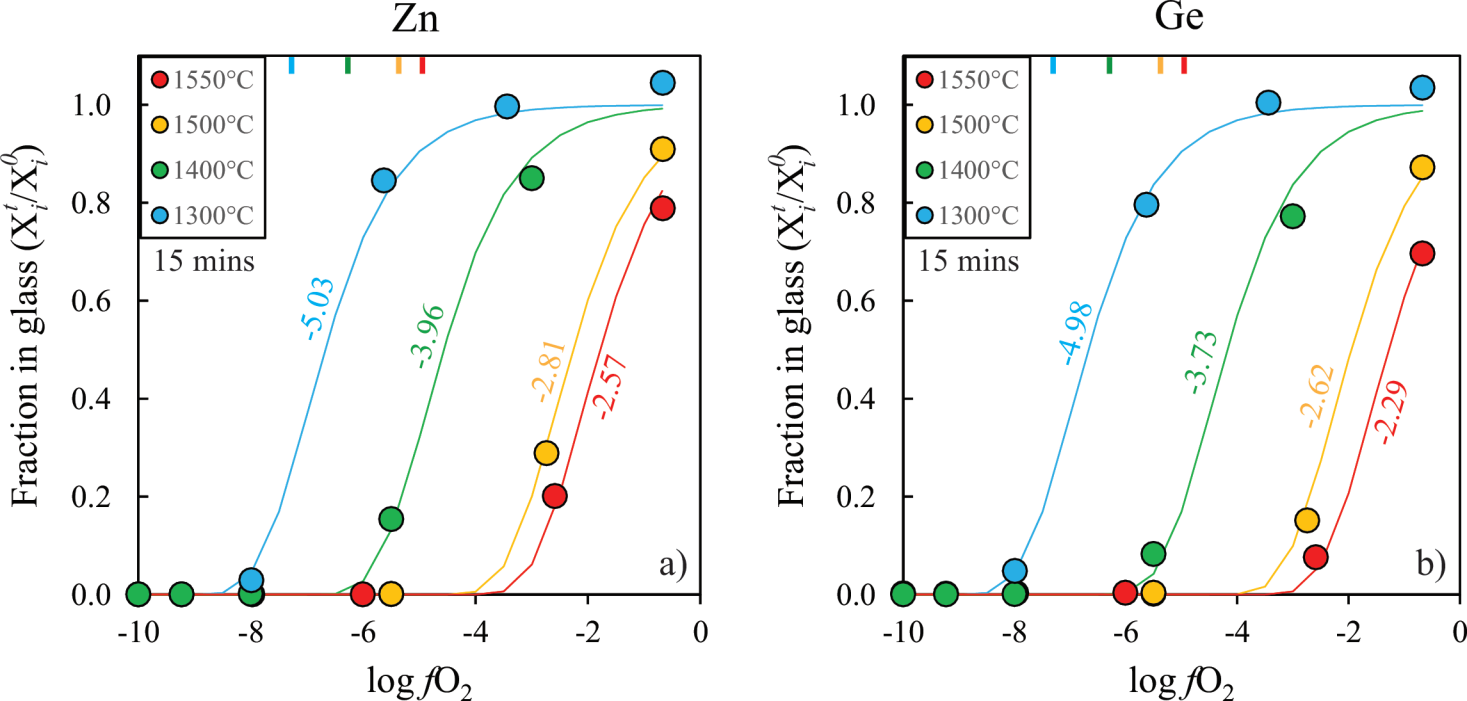
Zn
Ge
1550°C
1500°C
1400°C
1300°C
15 mins
-5.03
-3.96
-2.81
-2.57
-4.98
-3.73
-2.62
-2.29
a)
b)
Fraction in glass (X_i^t/X_i^0)
log fO_2
0.0
0.2
0.4
0.6
0.8
1.0
-10
-8
-6
-4
-2
0

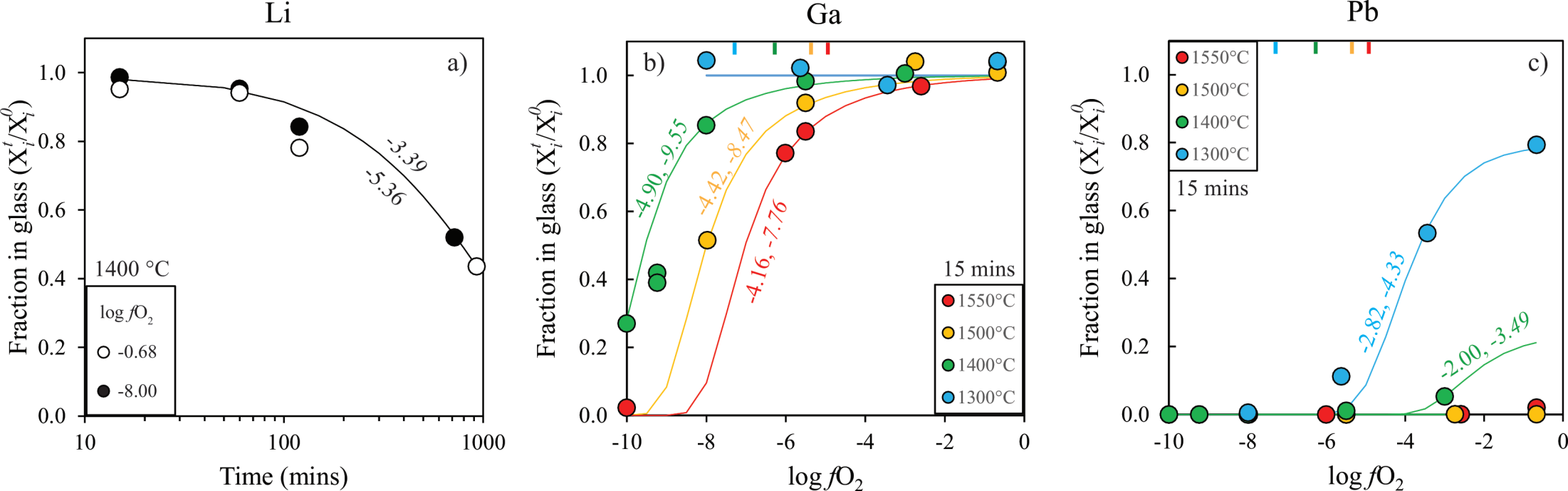
Li
a)
1400 °C
log fO_2
-0.68
-8.00
-3.39
-5.36
Fraction in glass (X_i^t/X_i^0)
Time (mins)
Ga
b)
-4.90, -9.55
-4.42, -8.47
-4.16, -7.76
15 mins
1550°C
1500°C
1400°C
1300°C
log fO_2
Pb
c)
1550°C
1500°C
1400°C
1300°C
15 mins
-2.82, -4.33
-2.00, -3.49
log fO_2

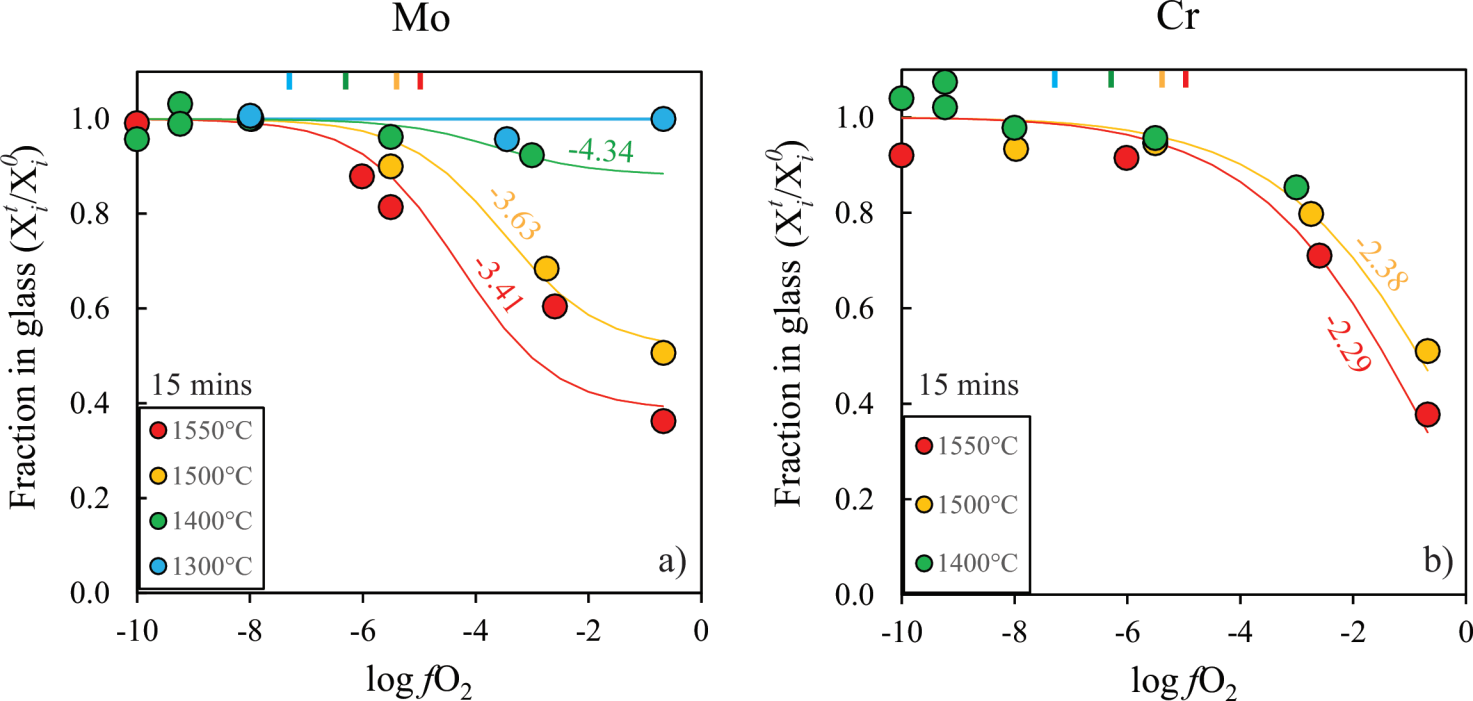
Mo
Cr
Fraction in glass (X_i^t/X_i^0)
log fO_2
15 mins
1550°C
1500°C
1400°C
1300°C
-4.34
-3.63
-3.41
-2.38
-2.29
a)
b)

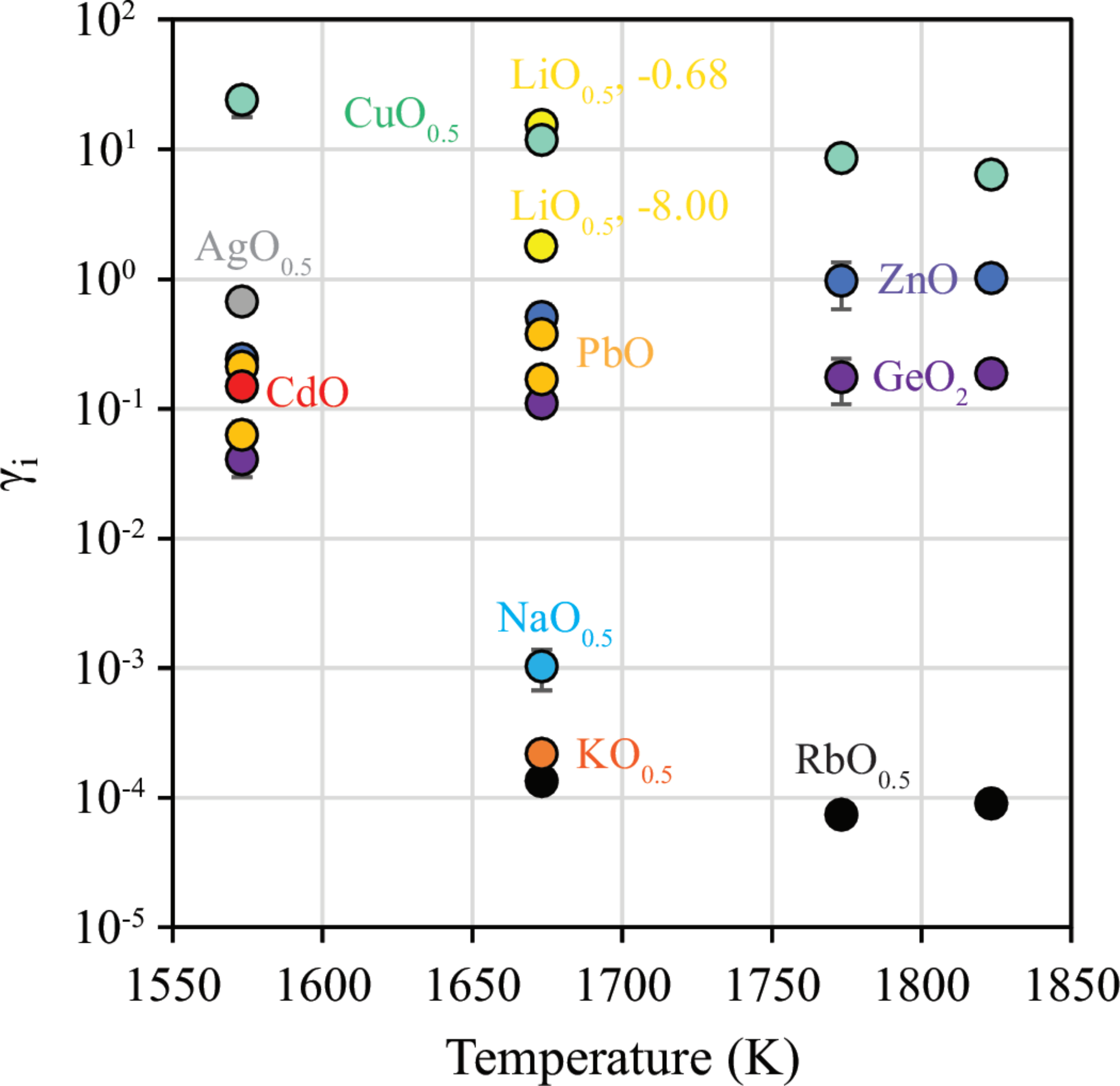
10^{2}
10^{1}
10^{0}
10^{-1}
10^{-2}
10^{-3}
10^{-4}
10^{-5}
γ_i
$CuO_{0.5}$
$LiO_{0.5}$, -0.68
$LiO_{0.5}$, -8.00
$AgO_{0.5}$
CdO
PbO
ZnO
GeO_2
$NaO_{0.5}$
$KO_{0.5}$
$RbO_{0.5}$
1550
1600
1650
1700
1750
1800
1850
Temperature (K)

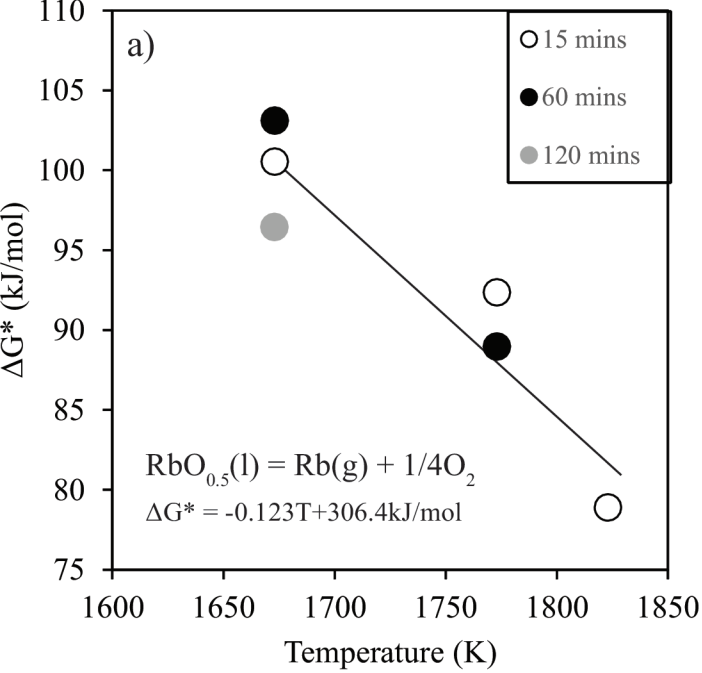
a)
15 mins
60 mins
120 mins
$RbO_{0.5}(l) = Rb(g) + 1/4O_2$
ΔG* = -0.123T+306.4kJ/mol
ΔG* (kJ/mol)
Temperature (K)
110
105
100
95
90
85
80
75
1600
1650
1700
1750
1800
1850

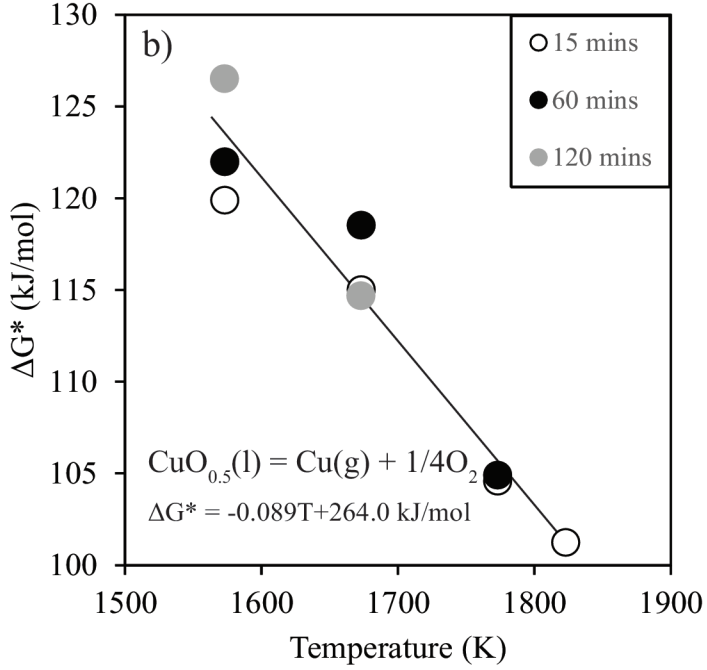
b)
15 mins
60 mins
120 mins
$CuO_{0.5}(l) = Cu(g) + 1/4O_2$
ΔG* = -0.089T+264.0 kJ/mol
ΔG* (kJ/mol)
Temperature (K)
130
125
120
115
110
105
100
1500
1600
1700
1800
1900

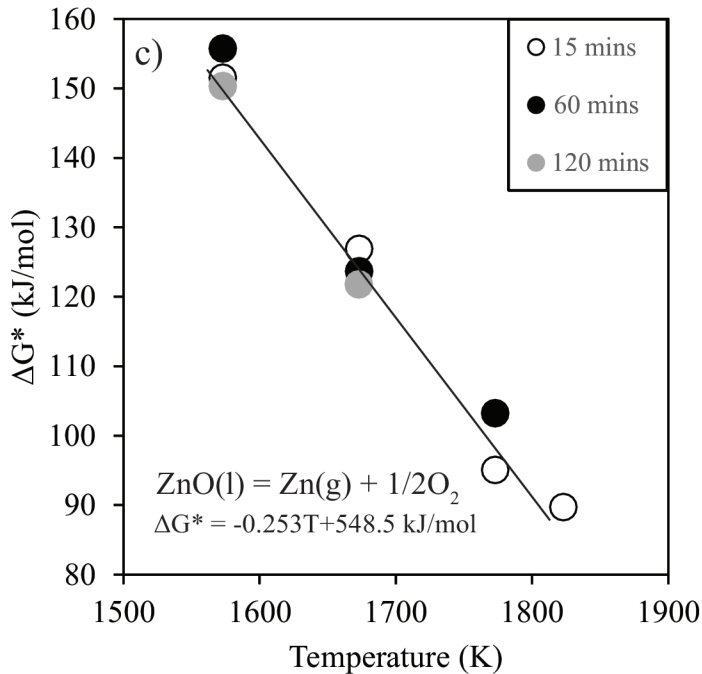
c)
15 mins
60 mins
120 mins
$ZnO(l) = Zn(g) + 1/2O_2$
ΔG* = -0.253T+548.5 kJ/mol
ΔG* (kJ/mol)
Temperature (K)
160
150
140
130
120
110
100
90
80
1500
1600
1700
1800
1900

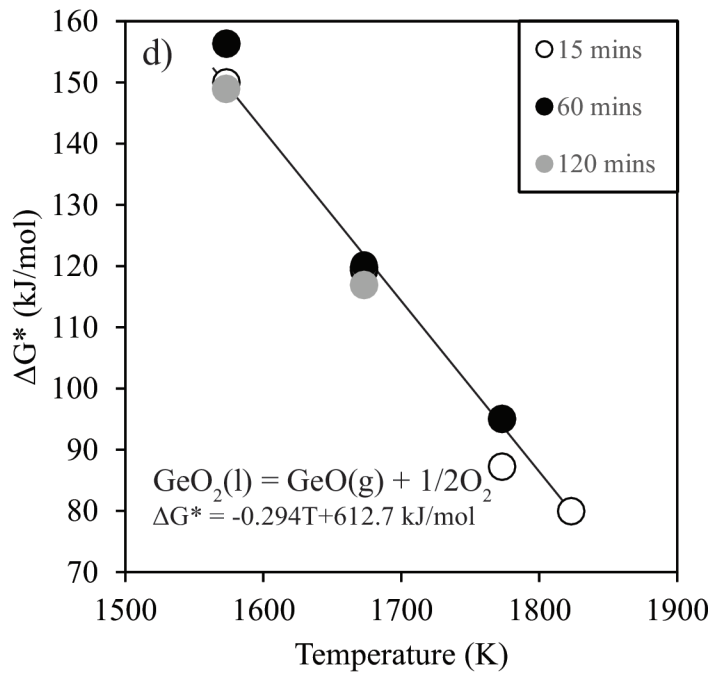
d)
15 mins
60 mins
120 mins
$GeO_2(l) = GeO(g) + 1/2O_2$
ΔG* = -0.294T+612.7 kJ/mol
ΔG* (kJ/mol)
Temperature (K)
160
150
140
130
120
110
100
90
80
70
1500
1600
1700
1800
1900

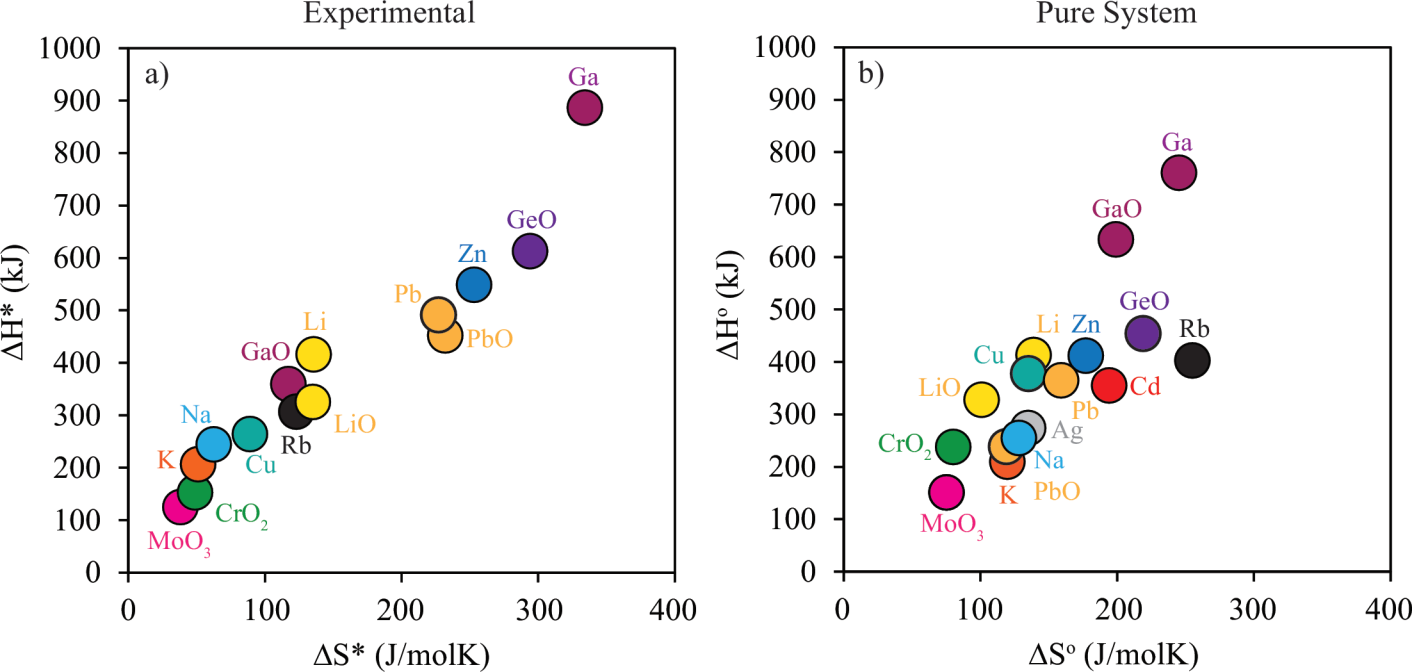
Experimental
a)
ΔH* (kJ)
ΔS* (J/molK)
Ga
GeO
Zn
Pb
PbO
Li
GaO
LiO
Na
K
Cu
Rb
CrO2
MoO3
Pure System
b)
ΔH° (kJ)
ΔS° (J/molK)
Ga
GaO
GeO
Rb
Li
Zn
Cu
LiO
Cd
Pb
Ag
CrO2
Na
K
PbO
MoO3

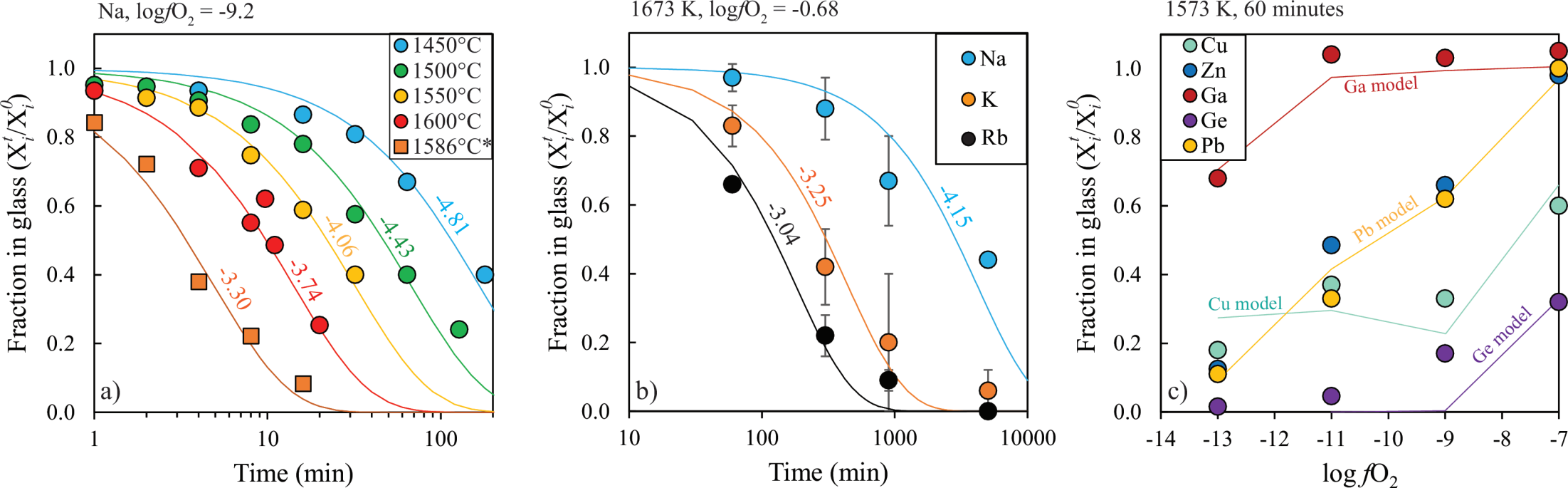
Na, logfO_2 = -9.2
1450°C
1500°C
1550°C
1600°C
1586°C*
-4.81
-4.43
-4.06
-3.74
-3.30
a)
Fraction in glass (X_i^t/X_i^0)
Time (min)
1673 K, logfO_2 = -0.68
Na
K
Rb
-4.15
-3.25
-3.04
b)
Fraction in glass (X_i^t/X_i^0)
Time (min)
1573 K, 60 minutes
Cu
Zn
Ga
Ge
Pb
Ga model
Pb model
Cu model
Ge model
c)
Fraction in glass (X_i^t/X_i^0)
log fO_2

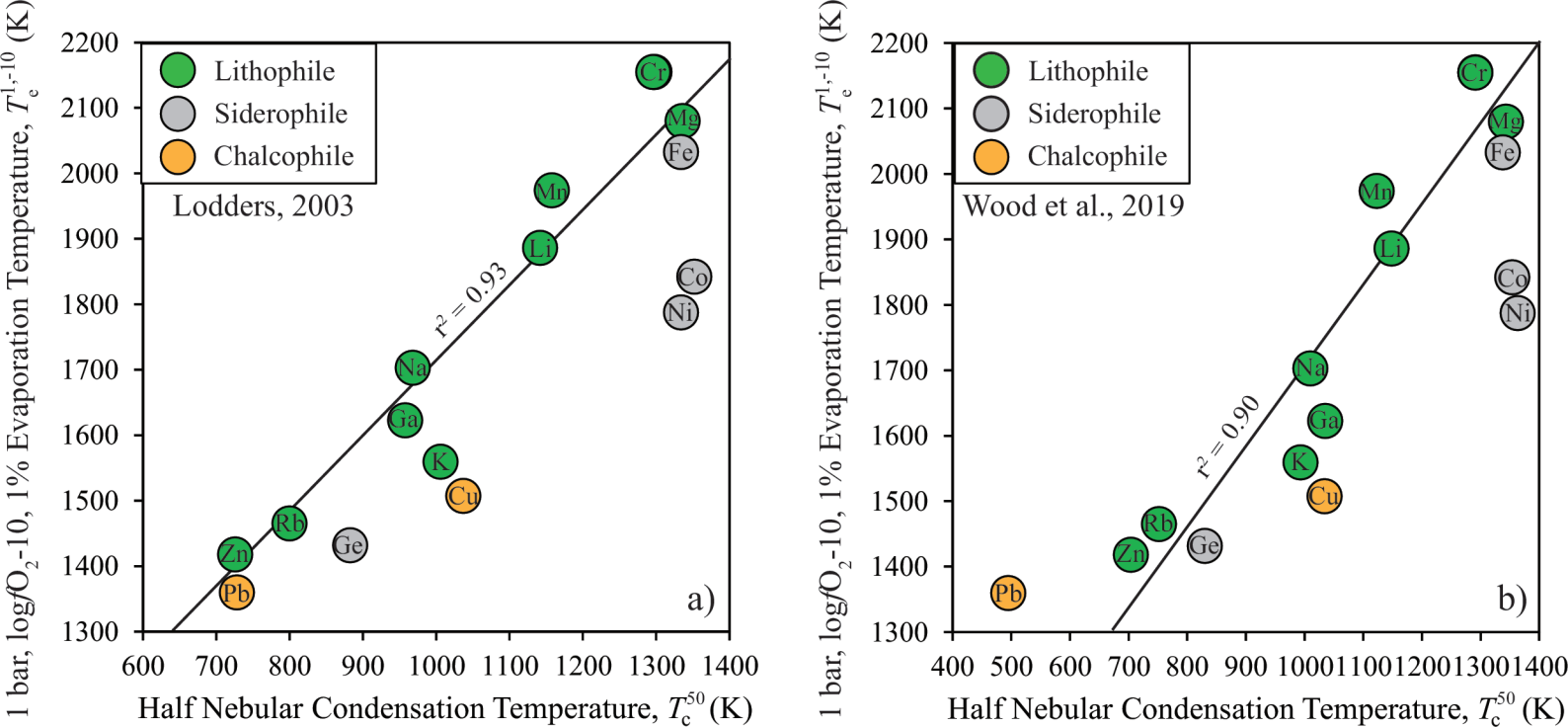
Lithophile
Siderophile
Chalcophile
Lodders, 2003
$r^2 = 0.93$
Cr
Mg
Fe
Mn
Li
Co
Ni
Na
Ga
K
Cu
Rb
Ge
Zn
Pb
a)
1 bar, logfO_2-10, 1% Evaporation Temperature, $T_e^{1,-10}$ (K)
Half Nebular Condensation Temperature, T_c^{50} (K)
Wood et al., 2019
$r^2 = 0.90$
b)

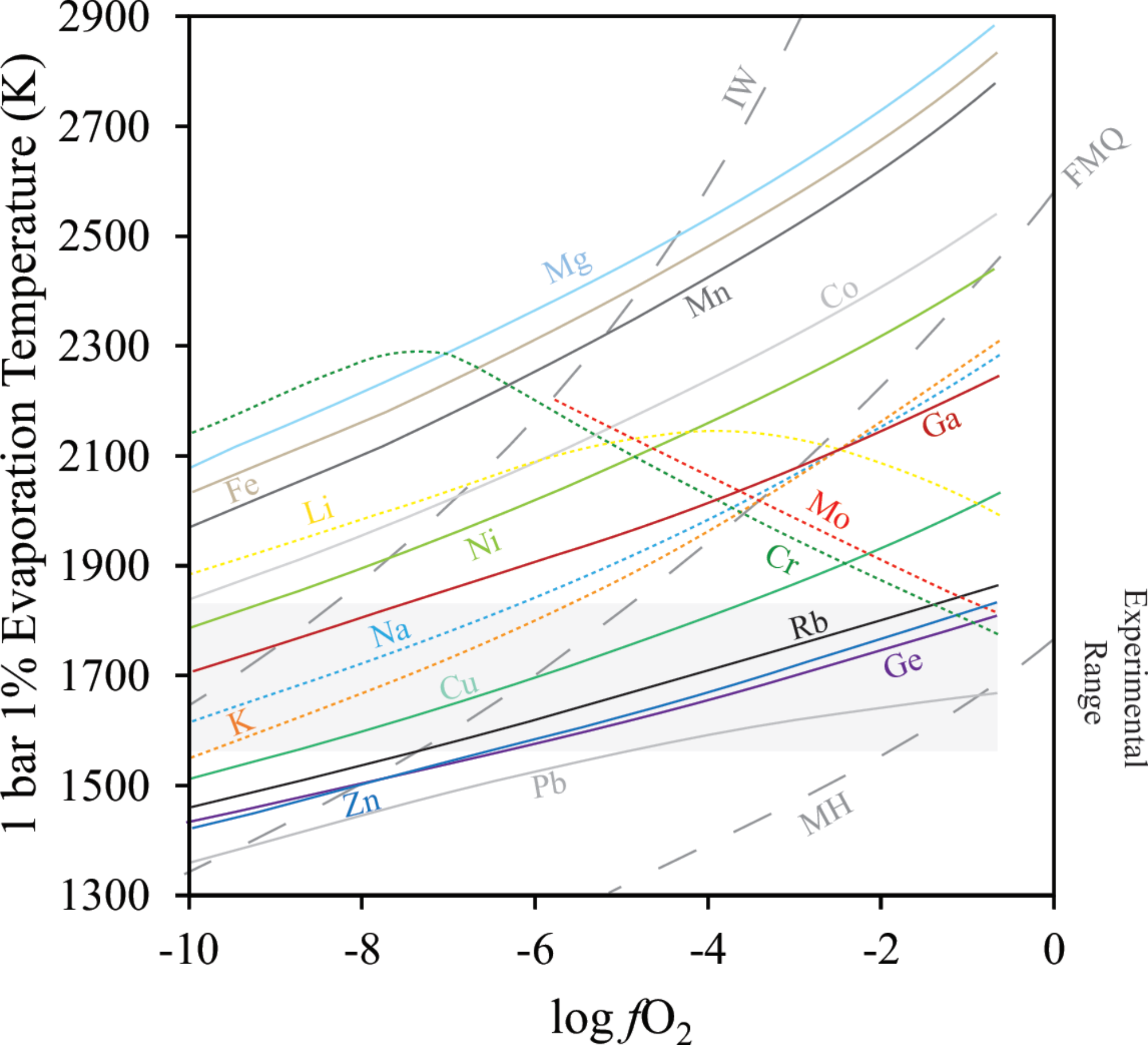
1 bar 1% Evaporation Temperature (K)
2900
2700
2500
2300
2100
1900
1700
1500
1300
-10
-8
-6
-4
-2
0
log fO_2
IW
FMQ
MH
Mg
Mn
Co
Fe
Li
Ni
Ga
Mo
Cr
Na
Rb
Ge
Cu
K
Zn
Pb
Experimental Range

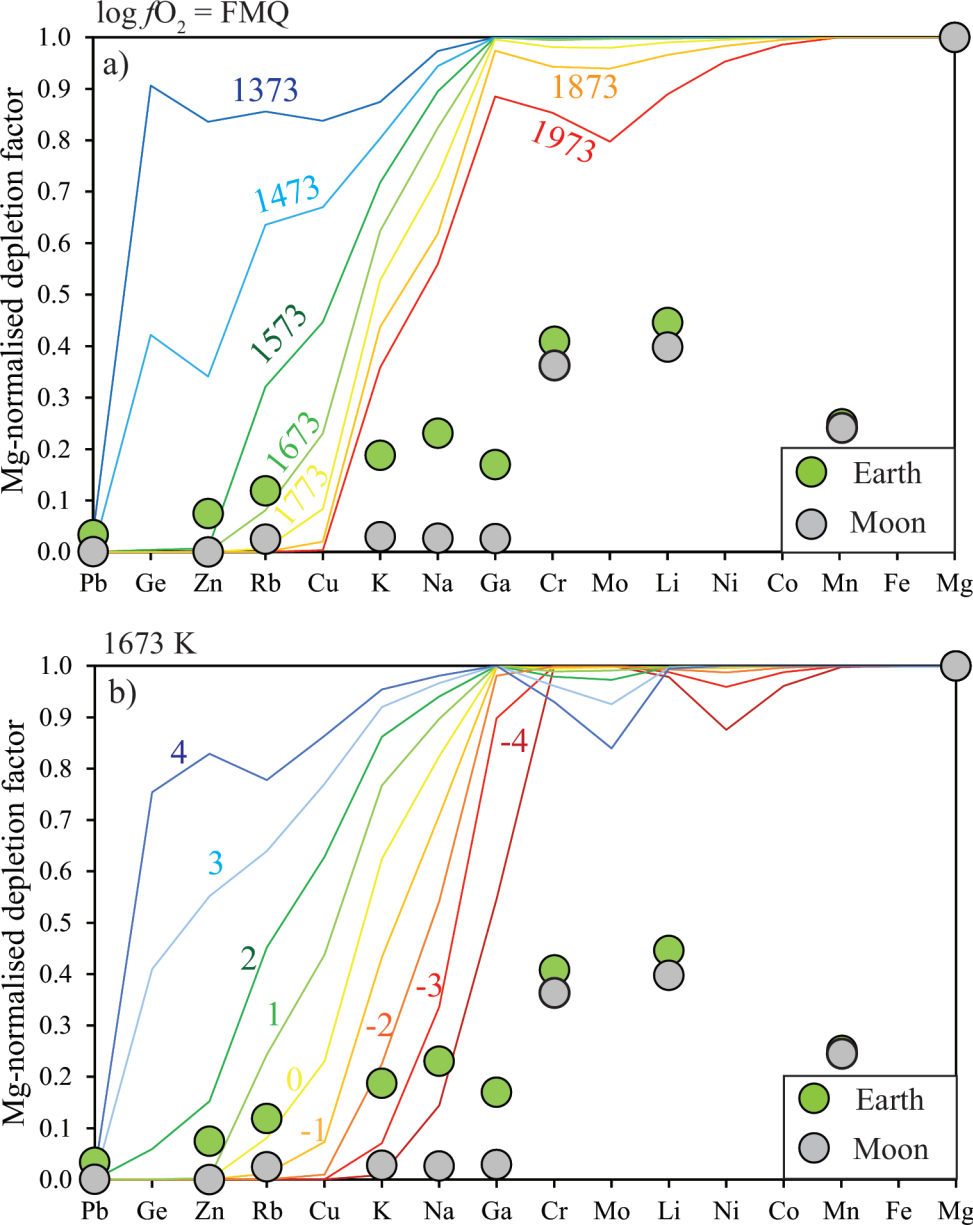
log fO_2 = FMQ
a)
1373
1473
1573
1673
1773
1873
1973
Mg-normalised depletion factor
Earth
Moon
Pb Ge Zn Rb Cu K Na Ga Cr Mo Li Ni Co Mn Fe Mg
1673 K
b)
4
3
2
1
0
-1
-2
-3
-4
Mg-normalised depletion factor
Earth
Moon
Pb Ge Zn Rb Cu K Na Ga Cr Mo Li Ni Co Mn Fe Mg

Table 1. Major (in wt. %) and trace element (in ppm) composition of the starting mixture. The 'calculated' column refers to that expected from added weights. The 'measured' column refers to EPMA analyses of glasses unaffected by Fe-loss or crystallisation post-experiment (major elements) and solution ICP-MS analyses of the de-carbonated powder pre-experiment (trace elements).

	Calculated	Measured	St. Dev.
wt. %		*N* = 8	
SiO_2	40.76	40.60	0.21
Al_2O_3	10.52	10.67	0.22
MgO	15.78	15.40	0.23
FeO	16.25	16.26	0.12
CaO	16.69	16.82	0.12
ppm		*N = 2*	
Li	1008.7	1020.0	17.8
Na	993.4	3252.3	281.3
K	1039.4	944.0	128.0
Sc	970.8	850.8	28.9
Ti	1008.0	1045.0	46.6
V	1019.7	1024.6	32.4
Cr	-	36.8	0.5
Mn	992.4	690.2	3.8
Cu	1009.5	1034.5	49.8
Zn	1015.5	1043.8	51.1
Ga	1019.3	1036.7	23.3
Ge	994.5	1007.7	44.6
Rb	1052.8	1036.1	62.4
Zr	991.9	1118.1	34.8
Mo	1029.0	1044.1	56.6
Ag	994.3	998.2	33.0
Cd	1037.0	991.1	33.2
La	1038.9	969.8	21.2
Gd	1063.3	1060.6	25.2
Yb	1036.2	1111.0	26.4
Pb	1002.7	1078.7	15.5

Table 2. Run conditions and LA-ICP-MS trace element data for all experiments. 'Y' denotes expeirments analysed for 25 µm zoning profiles ('Profile') and trace element contents in the wire loop ('Metal'). Experiments marked '*' denote repeat experiments.

Run#	T (°C)	t (min)	CO (sccm)	CO_2 (sccm)	logfO_2	Loop	Profile	Metal	Li	Na	K	Sc	Ti	V	Cr	Mn	Ni	Cu	Zn	Ga	Ge	Rb	Zr	Mo	Ag	Cd	La	Gd	Yb	Pb
2M-15-07-16c	1300	15	-	-	-0.68	Pt	Y		1429.4	6501.2	1245.0	1085.4	1312.4	1098.9	5.5	759.6	-	1024.7	1044.8	1093.8	1034.5	961.7	1088.1	999.9	358.4	448.0	1113.8	1276.0	1273.7	896.2
2M-15-07-16d	1300	15	-	200	-3.44	Pt			1446.9	10376.3	1570.7	1040.7	1196.3	1141.8	10.7	747.0	51.4	971.2	996.1	1020.1	1003.8	1003.2	1184.7	957.2	194.9	84.3	973.9	1125.9	1124.8	478.7
2M-15-07-16g	1300	15	1.8	200	-5.63	Pt			1445.2	13585.8	1868.9	1100.5	1285.4	1270.7	20.1	775.6	-	774.5	845.5	1072.9	795.2	960.3	1193.6	1108.0	5.3	0.2	1055.9	1192.3	1207.0	150.3
2M-15-07-16h	1300	15	24	175	-7.99	Pt			1477.8	11402.1	1798.9	1138.9	1425.6	1412.2	32.7	805.9	40.3	435.6	29.1	1095.9	48.1	963.3	1262.9	1006.2	0.4	0.0	1124.1	1293.8	1296.7	5.1
2M-15-07-16f	1300	15	156	100	-10.10	Pt	Y	Y																						
P11-06-18a*	1300	60	-	200	-3.44	Pt			1121.1	3222.8	1162.0	1023.2	1120.8	1211.7	7.8	709.6	7.0	888.3	981.2	1005.2	876.4	792.8	1228.8	967.6	0.2	0.1	1061.3	1040.4	1073.8	275.0
1M-15-07-16a*	1300	60	-	200	-3.44	Pt			1272.2	6412.8	1358.7	1064.7	1235.9	1113.7	8.1	734.5	8.5	885.1	954.5	1069.0	866.4	782.5	1190.9	972.3	4.1	0.2	1009.0	1164.9	1175.6	244.7
1M-15-07-16b	1300	60	1.9	200	-5.67	Pt			1406.2	15818.1	2075.5	1203.7	1385.7	1403.4	22.2	800.5	112.7	401.1	264.8	1046.1	248.6	589.7	1374.1	975.0	0.3	0.2	1184.5	1358.1	1366.1	1.5
1M-PS6	1300	60	25	180	-8.00	Pt			1201.3	16757.9	2053.3	1184.2	1368.3	1343.1	34.4	782.9	58.1	95.6	10.6	1083.9	21.3	198.7	1252.8	1092.8	0.5	0.1	1087.5	1171.2	1149.3	0.3
3M-18-07-16b	1300	120	-	-	-0.68	Pt			1384.2	7547.0	1011.0	1053.5	1224.3	1015.7	2.8	593.4	24.6	1019.6	1087.6	993.4	1004.0	577.0	1193.4	263.7	0.4	0.0	1019.4	1175.1	1197.6	7.2
2M-18-07-16a	1300	120	-	200	-3.44	Pt			1314.2	8911.1	1495.8	1092.9	1255.8	1294.5	4.7	756.5	46.2	728.5	712.2	1068.0	640.8	983.9	1219.5	765.5	0.2	0.2	1068.6	1211.1	1218.7	15.4
2M-18-07-16c	1300	120	12	188	-7.33	Pt		Y	1405.9	9559.0	1500.9	1149.6	1417.5	1283.4	32.7	721.6	42.6	192.2	2.0	1186.1	4.3	899.1	1341.5	980.3	0.1	0.2	1132.0	1284.3	1284.6	0.0
1M-PS3	1400	15	-	180	-3.07	Pt			1046.6	13784.1	1687.2	1209.1	1276.6	1181.1	30.7	828.4	11.8	837.0	908.1	1055.6	782.0	977.3	1193.7	923.3	3.6	0.1	1028.8	1098.1	1101.8	52.7
1M-PS2	1400	15	5	180	-5.49	Pt			1054.4	10421.8	1504.8	1229.9	1258.3	1188.1	34.4	760.4	5.3	623.3	353.6	1032.1	272.2	961.7	1198.2	962.1	0.7	0.1	1024.4	1101.1	1091.8	10.7
1M-PS4	1400	15	66	133	-8.00	Pt		Y	1084.6	14426.0	1562.7	1240.4	1350.8	1218.0	35.2	833.9	10.5	142.1	1.4	895.7	0.8	749.0	1242.8	1000.4	0.2	0.1	1067.2	1170.6	1167.3	0.1
P09/06/18b*	1400	15	130	65	-9.23	Pt			1199.2	2013.9	732.4	1006.1	1156.0	1179.1	38.7	802.1	13.0	40.5	0.4	439.9	1.2	521.5	1092.2	1031.1	0.1	0.1	1003.8	930.5	947.3	0.0
P09/06/18a*	1400	15	130	65	-9.23	Re			1161.9	1901.2	684.2	1087.0	1180.8	1129.2	36.7	722.0	0.8	11.2	0.3	409.4	0.1	578.5	1126.5	989.7	0.1	0.0	1026.6	978.1	1006.7	0.0
1M-PS5	1400	15	167	33	-10.01	Pt		Y	1110.8	8419.1	1168.0	1177.3	1290.5	1223.5	37.4	851.2	6.9	15.6	0.3	283.2	0.4	436.3	1209.0	957.2	0.2	0.1	1020.5	1096.3	1090.7	0.0
P08-02-17b*	1400	60	-	-	-0.68	Pt			1034.8	3076.2	912.7	1112.2	1188.2	1190.2	9.1	692.7	9.1	840.3	1039.1	1031.2	729.2	677.1	1076.3	467.2	0.1	0.1	1033.8	1001.2	992.6	0.0
3M-29/2/16*	1400	60	-	-	-0.68	Pt	Y		1028.3	5703.4	921.1	1100.3	1084.4	1025.8	11.3	721.4	5.5	816.6	953.7	1028.4	800.6	708.0	1119.2	441.9	0.1	0.1	915.9	992.2	984.1	0.3
1M-2/3/16*	1400	60	-	200	-3.07	Pt			1129.1	10167.2	895.7	1279.7	1273.1	1148.6	28.1	863.9	13.5	695.1	348.0	878.0	214.0	358.6	1232.1	792.1	0.4	2.4	1074.7	1154.5	1178.0	3.4
C18/12/15*	1400	60	0	27	-3.07	Ir			1038.8	3167.7	911.7	1230.0	1346.1	1132.3	29.0	852.5	8.5	833.8	183.4	971.2	115.8	426.7	1090.0	820.8	0.1	0.2	1044.3	1121.8	1110.6	0.4
1M-PS1*	1400	60	5	180	-5.50	Pt		Y	1069.5	9048.0	1363.8	1008.1	1135.3	1194.8	35.6	784.8	5.5	300.5	6.5	930.5	1.6	57.7	1085.8	951.0	0.1	0.1	1037.6	1129.6	1113.6	0.1
P09/06/18c*	1400	60	5.5	195	-5.51	Re			1033.0	2345.0	547.1	1049.5	1135.7	1155.8	36.1	749.3	9.4	327.7	0.4	876.6	0.2	32.2	1011.0	983.2	0.1	0.1	1049.7	951.0	967.6	0.0
C17/12/15a	1400	60	13	27	-7.97	Re			1048.1	1068.8	40.2	1294.5	1418.9	1140.8	35.6	820.4	13.7	13.9	0.3	677.3	0.5	0.3	1499.7	980.2	0.1	0.1	1083.9	1199.7	1193.8	0.0
1M-1/3/16	1400	60	167	33	-10.01	Re		Y	1149.9	3924.1	5.2	1363.5	1396.8	1449.9	38.5	845.8	35.7	6.5	0.8	122.6	4.9	0.1	1132.6	947.5	0.1	0.1	1203.8	1276.6	1276.8	0.0
3M-1/3/16	1400	120	-	-	-0.68	Pt			858.8	20028.4	1102.7	1102.7	1323.2	1258.5	3.6	779.3	76.6	772.6	774.5	1041.6	577.5	368.7	1187.9	9.4	0.1	0.0	1117.6	1219.0	1247.2	0.2

C17/12/15b	1400	120	13	27	-7.97	Re			976.2	950.6	7.7	1223.9	1317.2	1129.1	36.4	754.6	23.6	10.5	0.3	564.1	0.3	0.3	1245.3	857.3	0.2	0.1	1022.5	1110.5	1111.9	0.0
1M-1/3/16b	1400	120	167	33	-10.01	Re		Y	1044.3	1576.5	196.5	1320.6	1385.9	1280.5	36.0	819.9	56.2	4.4	0.2	19.1	2.2	8.3	1896.7	670.2	0.1	0.1	1159.5	1270.7	1275.3	0.0
3M-29/2/16b	1400	930	-	-	-0.68	Pt			479.2	5993.0	541.0	1233.4	1170.0	1149.1	1.3	782.4	9.6	438.9	486.6	1086.2	96.4	113.6	1062.8	10.8	0.1	0.1	1033.7	1108.6	1132.6	0.1
C17/12/15c	1400	720	13	27	-7.97	Re	Y	Y	571.9	32.6	1.1	1308.9	1349.0	1190.2	40.9	843.3	22.7	1.6	0.2	120.1	0.3	0.1	1013.3	718.4	0.1	0.1	1105.7	1196.4	1198.2	0.3
2M-16-07-16e	1500	15	-	-	-0.68	Pt			952.5	7896.9	1199.2	1137.2	1319.0	1148.8	18.4	848.9	105.4	922.3	909.2	1058.2	872.3	955.1	1253.0	506.4	1.4	0.2	1034.3	1194.3	1220.7	0.6
2M-16-07-16a	1500	15	-	200	-2.74	Pt			1217.1	10642.4	1384.8	1130.0	1219.5	1213.4	28.7	742.5	101.2	574.0	288.5	1092.7	151.3	912.9	1185.7	683.8	0.2	0.2	1025.7	1168.3	1191.4	0.5
2M-16-07-16b	1500	15	16	184	-5.50	Pt			1319.4	4959.0	1205.5	1106.7	1238.0	1188.5	34.1	739.9	6.8	311.1	0.5	964.7	3.7	809.7	1155.6	899.5	0.1	0.1	988.5	1134.6	1158.2	0.1
2M-16-07-16c	1500	15	120	80	-7.97	Re	Y		1287.4	4577.0	957.7	1081.0	1247.0	1154.1	33.6	738.1	7.8	39.5	0.2	540.4	2.8	501.9	1155.5	999.5	0.2	0.1	967.9	1117.7	1135.9	0.1
3M-2/3/16	1500	60	-	-	-0.68	Pt			597.3	9378.6	1012.6	1227.5	1210.9	1200.3	3.8	764.0	13.2	570.6	566.3	1079.7	149.7	339.1	1136.7	23.6	0.1	0.6	1032.8	1092.1	1108.4	0.1
2M-17-07-16a	1500	60	-	200	-2.74	Pt	Y		1307.9	5028.1	984.8	1069.1	1239.6	1095.5	21.6	717.7	21.8	372.7	66.1	1096.5	3.9	157.0	1155.0	347.0	0.2	0.2	980.9	1116.5	1136.9	0.1
2M-17-07-16b	1500	60	16	184	-5.50	Pt		Y	1376.6	4711.9	727.7	1082.7	1214.1	1145.4	32.4	760.1	18.8	54.0	0.3	775.1	2.6	27.9	1163.7	609.4	0.1	0.2	991.7	1142.3	1160.1	0.0
2M-17-07-16c	1500	60	120	80	-7.97	Pt		Y	1411.2	1842.0	281.8	1103.9	1312.0	1199.8	34.9	784.9	4.2	10.8	0.2	67.4	1.9	4.8	1158.8	944.1	0.1	0.1	1016.1	1138.9	1153.4	0.1
2M-16-07-16f	1550	15	-	-	-0.68	Pt			580.9	11969.3	1808.5	1137.0	1298.5	1232.4	13.6	801.1	172.5	791.8	768.2	1091.2	696.2	967.6	1189.9	362.0	1.5	0.2	1051.4	1197.7	1212.1	19.9
2M-16-07-16g	1550	15	-	200	-2.59	Pt			621.8	7199.0	1314.1	1149.4	1368.7	1175.1	25.6	825.4	50.3	663.5	251.1	1016.4	76.1	832.3	1240.3	604.2	0.3	0.2	1052.9	1198.4	1217.0	0.5
P11-06-18b	1550	15	25	175	-5.48	Pt			1147.9	2485.5	865.2	1066.8	1123.5	1120.4	34.1	747.4	15.0	103.7	0.5	876.5	1.5	551.3	1057.7	813.9	0.2	0.1	1004.2	964.8	998.6	0.2
2M-16-07-16h	1550	15	42	158	-6.01	Pt	Y	Y	1341.0	4106.7	957.5	1106.0	1239.6	1161.5	32.9	766.4	10.5	138.5	0.4	809.8	3.2	544.6	1201.6	879.0	0.2	0.2	1002.7	1144.9	1162.8	0.0
2M-16-07-16d	1550	15	188	12	-9.56	Re			1361.8	2721.8	480.9	1079.6	1220.5	1108.4	33.1	819.6	5.1	5.7	0.2	22.8	2.3	118.8	1188.0	990.9	0.1	0.1	975.9	1117.6	1128.9	0.0
Blank Runs																														
P28-05-18	1400	15	-	-	-0.68	Pt			0.1	92.1	77.7	0.3	2.0	0.4	1.2	1.3	6.3	1.6	3.0	0.1	0.1	0.1	0.2	0.4	0.1	0.2	0.3	3.1	0.0	1.4
P23-05-18a	1400	60	50	100	-8.00	Re			0.2	45.7	12.1	0.4	1.3	0.3	0.1	1.1	34.5	1.0	0.2	0.4	0.1	0.1	0.2	7.3	0.0	0.0	0.2	4.1	0.0	0.0
P24-05-18a	1500	60	93	60	-8.00	Re			0.3	25.6	1.5	0.3	1.6	0.4	1.1	2.2	119.5	1.4	0.2	2.5	0.1	0.1	0.2	5.9	0.0	0.0	0.3	3.4	0.0	0.0
P24-05-18b	1500	120	93	60	-8.00	Re			0.3	15.6	0.6	0.3	1.7	0.4	1.7	2.2	101.8	0.8	0.2	1.9	0.1	0.0	0.2	10.8	0.0	0.0	0.3	3.9	0.0	0.0

Table 3. The logK^* values and SD uncertainty and stoichiometries of reaction (n) found by non-linear least-squares fit to the experimental data.

Element	Reaction	n	t_0 (min)	logK^*			
				1573.15 K	1673.15 K	1773.15 K	1823.15 K
Li	$LiO_{0.5}(l) = Li(g) + ¼O_2$	1	0		-5.36±0.05		
N					2		
Li	$LiO_{0.5}(l) + ¼O_2 = LiO(g)$	-1	0		-3.39±0.07		
N					2		
Na	$NaO_{0.5}(l) = Na(g) + ¼O_2$	1	0		-4.25±0.10		
N					2		
K	$KO_{0.5}(l) = K(g) + ¼O_2$	1	0		-3.95±0.06		
N					2		
Rb	$RbO_{0.5}(l) = Rb(g) + ¼O_2$	1	14.4	-4.15	-3.12±0.10	-2.63±0.02	-2.26
N				1	3	2	1
Cu	$CuO_{0.5}(l) = Cu(g) + ¼O_2$	1	0	-4.09±0.12	-3.70±0.10	-3.13±0.06	-2.90
N				3	3	2	1
Ag	$AgO_{0.5}(l) = Ag(g) + ¼O_2$	1	0	-2.23			
N				1			
Zn	$ZnO(l) = Zn(g) + ½O_2$	2	9.0	-5.06±0.09	-3.96±0.09	-2.92±0.17	-2.57
N				3	4	2	1
Ge	$GeO_2(l) = GeO(g) + ½O_2$	2	10.4	-5.04±0.13	-3.70±0.06	-2.71±0.13	-2.29
N				3	4	2	1
Cd	$CdO(l) = Cd(g) + ½O_2$	2	0	-2.48			
N				1			
Ga	$GaO_{1.5}(l) = Ga(g) + ¾O_2$	3	0		-9.92±0.32	-8.42±0.07	-7.76
N					3	2	1
Ga	$GaO_{1.5}(l) = GaO(g) + ¼O_2$	1	0		-5.10±0.26	-4.45±0.04	-4.16
N					3	2	1
Pb	$PbO(l) = PbO(g)$	0	0	-2.90±0.12	-2.00		
N				2	1		
Pb	$PbO(l) = Pb(g) + ½O_2$	2	0	-4.47±0.19	-3.49		
N				2	1		
Mo	$MoO_3(l) = MoO3(g)$	0	0	-4.67	-4.34±0.00	-3.64±0.01	-3.41
N				1	2	2	1
Mo	$MoO_2(l) + ½O_2 = MoO_3(g)$	-2	0	-2.87	-2.86±0.00	-2.48±0.01	-2.39
N				1	2	2	1
Cr	$CrO(l) + ½O_2 = CrO_2(g)$	-2	0		-2.70	-2.40±0.03	-2.29
N					1	2	1
Cr	$CrO_{1.5}(l) + ¼O_2 = CrO_2(g)$	-1	0		-4.96	-4.41±0.03	-4.20
N					1	2	1

Table 4. Evaporation- (α_e) and activity coefficients (γ_i) of melt oxide species. Evaporation coefficients calculated with eq. 6 using activity coefficients shown in the references, activity coefficients calculated with $\alpha_e = 1$ from eq. 6.

Species		**Temperature (K)**				
		1573.15	1673.15	1773.15	1823.15	1923.15
ZnO	γ_i (this work)	0.24±0.02	0.51±0.13	0.97±0.38	1.01	
	γ_i (literature)		0.25[a]	0.43[a]	0.58[a]	
	α_e		2.0	2.2	1.7	
$RbO_{0.5}$	γ_i (this work)		$1.3\times10^{-4}\pm1.5\times10^{-5}$	$7.4\times10^{-5}\pm5.9\times10^{-6}$	9.0×10^{-5}	
GeO_2	γ_i (this work)	0.04±0.01	0.11±0.01	0.18±0.07	0.19	
$CuO_{0.5}$	γ_i (this work)	24.0±6.3	11.8±1.7	8.5±0.1	6.4	4.2*
	γ_i (literature)	10±1[b]				3.5[c]
	α_e	2.4±0.8				1.2
$KO_{0.5}$	γ_i (this work)		$2.2\times10^{-4}\pm5.5\times10^{-5}$			
	γ_i (literature)		5×10^{-5} - 7×10^{-4}[, d]			
	α_e		0.3 - 3.4			
$NaO_{0.5}$	γ_i (this work)		$1.0\times10^{-3}\pm2.2\times10^{-4}$			
	γ_i (literature)		8.4×10^{-4} - 2.2×10^{-3}[, e]			
	α_e		0.3 – 1.7			
PbO^	γ_i (this work)	0.06±0.02	0.17			
	γ_i (literature)					0.22[c]
	α_e	0.3*	0.8*			
PbO#	γ_i (this work)	0.21±0.09	0.38			
	γ_i (literature)					0.22[c]
	α_e	1.0*	1.7*			
$LiO_{0.5,}$ (air)	γ_i (this work)		1.8±0.2			
$LiO_{0.5}$ (-8)	γ_i (this work)		15.4±3.1			
$AgO_{0.5}$	γ_i (this work)		0.67			
CdO	γ_i (this work)		0.15			

a = Reyes and Gaskell, 1983; b = Holzheid et al. 2001; c = Wood and Wade, 2013; d = Hastie et al. 1982; e = Mathieu et al. 2011

^ = calculated from the reaction PbO(l) = PbO(g)

= calculated from the reaction PbO(l) = Pb(g) + ½O_2

* extrapolated to 1923.15 K

Table 5. Equilibrium thermodynamic data (entropy and entropy) for reactions investigated herein (experimental) in addition to those in the metal-oxygen system (pure system).

				Experimental				Pure System		
Element	Reaction	*n*	# points	ΔS* (kJ/molK)	±	ΔH* (kJ)	±	ΔS^o (kJ/molK)	ΔH^o (kJ)	Source
Experimental										
Li*	$LiO_{0.5}(l) = Li(g) + 1/4O_2$	1	1	0.133		413.0		0.139	413.0	*1*
Li*	$LiO_{0.5}(l) = Li(g) + 1/4O_2$	-1	1	0.130		326.3		0.107	326.3	*1*
Na*	$NaO_{0.5}(l) = Na(g) + 1/4O_2$	1	1	0.071		255.0		0.128	255.0	*2*
K*	$KO_{0.5}(l) = K(g) + 1/4O_2$	1	1	0.050		209.5		0.120	209.5	*2*
Cr*	$CrO(l) + 1/2O_2 = CrO_2(g)$	-2	4	0.046	0.016	163.1	28.6	0.080	237.6	*1, 6*
Cr*	$CrO_{1.5}(l) + 1/4\ O_2 = CrO_2(g)$	-1	4	0.085	0.017	301.2	29.1	0.128	414.3	*1*
Cu	$CuO_{0.5}(l) = Cu(g) + 1/2O_2$	1	9	0.089	0.009	264.0	15.7	0.135	377.7	*1, 4*
Zn	$ZnO(l) = Zn(g) + 1/2\ O_2$	2	10	0.253	0.011	548.6	19.6	0.177	411.7	*3*
Ga	$GaO_{1.5}(l) = Ga(g) + 3/4O_2$	3	6	0.334	0.026	885.9	45.7	0.245	760.4	*3*
Ga	$GaO_{1.5}(l) = GaO(g) + 1/4O_2$	1	6	0.117	0.015	358.9	24.6	0.199	633.7	*3*
Ge	$GeO_2(l) = GeO(g) + 1/2O_2$	2	10	0.294	0.014	612.7	23.9	0.219	453.8	*3*
Rb	$RbO_{0.5}(l) = Rb(g) + 1/4O_2$	1	6	0.123	0.024	306.4	41.6	0.255	402.4	*2*
Mo*	$MoO_3(l) = MoO_3(g)$	0	6	0.118	0.016	332.4	16.4	0.120	316.3	*1*
Mo*	$MoO_2(l) + 1/2O_2 = MoO_2(g)$	-2	6	0.033	0.004	143.2	7.8	0.075	151.2	*1*
Pb	$PbO(l) = PbO(g)$	0	3	0.232	0.043	452.1	70.6	0.119	238.0	*3*
Pb	$PbO(l) = Pb(g) + 1/2O_2$	2	3	0.227	0.070	490.9	112.1	0.159	364.7	*3*
Pure System[#]										
Mg	$MgO(l) = Mg(g) + 1/2O_2$	2						0.186	666.4	*1*
Ni	$NiO(l) = Ni(g) + 1/2O_2$	2						0.200	597.5	*1,5*
Fe	$FeO(l) = Fe(g) + 1/2O_2$	2						0.183	644.4	*1*
Mn	$MnO(l) = Mn(g) + 1/2O_2$	2						0.173	606.3	*1,4*
Co	$CoO(l) = Co(g) + 1/2O_2$	2						0.192	600.0	*1,4*
Cr	$CrO(l) = Cr(g) + 1/2O_2$	2						0.197	712.6	*1,6*

1 Chase 1998 ; 2 Lamoreaux and Hildenbrand, 1984 ; 3 Lamoreaux et al., 1987; 4 O'Neill and Pownceby, 1993; 5 Robie and Hemingway, 1995; 6 Toker et al., 1991

* denotes elements for which log*K** was measured at only 1 temperature, ΔS* and ΔH* determined by assuming γ_i remains constant over all temperatures.

pure system elements were calculated assuming $\gamma_i = 1$ at all temperatures.

^{o} enthalpies and entropies of formation for pure system calculated from $\Delta G^o = \Delta H^o - T\Delta S^o$ from T = 1000 to 2000 K

Table 6. 1% Evaporation temperatures from silicate melt at 1 bar

logfO_2	-10		-5		-0.68	
Element	T (K)	±	T (K)	±	T (K)	±
Pb	1360	50	1563	9	1669	6
Ge	1432	9	1612	3	1809	4
Zn	1418	10	1618	5	1843	2
Rb	1465	28	1668	5	1863	16
Cu	1507	9	1746	3	2023	22
K	1548		1867		2290	
Ga	1703	1	1959	17	2239	47
Na	1623		1914		2267	
Li	1886		2092		1976	
Cr	2155		2096	52	1785	4
Mo			2138	41	1816	3
Mg	2080		2445		2883	
Ni	1787		2086		2439	
Fe	2033		2394		2830	
Mn	1974		2339		2783	
Co	1842		2159		2538	